Republic of Iraq
Ministry of Higher Education
and Scientific Research
University of Babylon
College of Science
Department of Physics

Study of the Photocatalytic Activity for the Synthesized Modified Zinc Oxide Nanocomposites

Thesis

Submitted to the Council of the College of Science
University of Babylon in Partil Fulfilment of the Requirements for the Degree of Doctor of Philosophy in Science / Physics

By

Ahmed Mesehour Ali Refaas

B.Sc. in physics University of Al Muthanna / 2007
M.Sc. in physics University of Babylon / 2016

Supervised by

Prof. Dr. Enas M.AL-Robayi
College of Science for Women
University of Babylon

Prof. Dr. Ayad F. Alkaim
College of Science for Wome
University of Babylon

2023 A.D **1445 A.H**

بِسْمِ اللَّهِ الرَّحْمَٰنِ الرَّحِيمِ

﴿يَٰٓأَيُّهَا ٱلَّذِينَ ءَامَنُوٓاْ إِذَا قِيلَ لَكُمۡ تَفَسَّحُواْ فِي ٱلۡمَجَٰلِسِ فَٱفۡسَحُواْ يَفۡسَحِ ٱللَّهُ لَكُمۡۖ وَإِذَا قِيلَ ٱنشُزُواْ فَٱنشُزُواْ يَرۡفَعِ ٱللَّهُ ٱلَّذِينَ ءَامَنُواْ مِنكُمۡ وَٱلَّذِينَ أُوتُواْ ٱلۡعِلۡمَ دَرَجَٰتٖۚ وَٱللَّهُ بِمَا تَعۡمَلُونَ خَبِيرٞ﴾

صَدَقَ اللهُ العَلِيُّ الْعَظِيمُ

﴿ المجادلة: الآية ١١﴾

Dedication

To the souls of my parents,

in their eternal world, in their all anniversary,

I dedicate my work. To my brother, my children

and my wife, who was a great credit during this

scientific journey.

Ahmed

Acknowledgements

My thanks and gratitude to Dr. Enas M. al-Robayi and Dr. Ayad F. Alkaim, for their project and continuous follow-up.

Thanks are extended to my professors in the Department of Physics, in college of science, and Department of Chemistry in college of science for women.

In addition my thanks appreciation to my colleague Muammar Hassan Aidan, who was a great credit during this scientific journey, and to his honorable family.

Ahmed

Summary

Zinc oxide (ZnO), Zinc oxide vanadium pentoxide V_2O_5/ZnO nanocomposite was prepared by “hydrothermal synthesis technique”.

Zinc oxide vanadium pentoxide nanocomposite doped with silver Ag/V_2O_5/ZnO was prepared by photodeposition process as nanocatalysts.

Using the techniques of (XRD, FE-SEM, EDX, FTIR, TEM, and BET surface analysis). Each of structure, surface composition and optical characteristics of the catalysts were examined. Nanocomposite (silver-doped) was distinguished by the highest peak compared to the other prepared nanocomposites.

The crystal size for the prepared nanocomposites was calculated. The silver-doped nanocomposite was distinguished by the lowest crystal size, which confirms the effect of silver in the photodeposition process and the success of the preparation of the nanocomposites. Ag/V_2O_5/ZnO surface area has increased compared to the ZnO and V_2O_5/ZnO composite.

Photocatalytic-degradation process of maxilon blue GRL dye was investigated by using prepared V_2O_5/ZnO and Ag/V_2O_5/ZnO nanocomposites.

The degradation of dye was performed by irradiated aqueous solutions containing different concentrations of dye and different amounts for nanocomposites using UV-Vis lamp with different intensities.

Effect of the various factors on the photocatalytic-degradation process of GRL dye was tested to reach an optimal state, where they involve effect of the nanocomposites mass, effect of GRL dye concentration and effect of light intensity.

A comparative study of the photocatalysis for the prepared nanocomposites was carried out, the efficiency of dye removal changes dramatically with time up to 60 min.

The absorbance, transmittance, reflectivity spectra, refractive index, extinction coefficient and optical absorption for catalysts materials within the wavelength 590 nm was calculated.

The energy gap was calculated for the ZnO, V_2O_5/ZnO and Ag/V_2O_5/ZnO, it value was (3.25, 3.15 and 3.04) eV, respectively.

The Ag/V_2O_5/ZnO nanocomposite exhibited enhanced photocatalytic activity under UV-visible light irradiation for the degradation of maxilon blue dye compared with binary V_2O_5/ZnO nanocomposite.

The small size, high surface area and synergistic effect in the Ag/V_2O_5/ZnO nanocomposite is responsible for high photocatalytic activity. These results also showed that the Ag nanoparticles induced visible light activity and facilitated efficient charge separation in the Ag/V_2O_5/ZnO nanocomposite, thereby improving the photocatalytic performance.

Contents

List of Abbreviations and Symbols

Symbols	Terms	Units
NPs	Nanoparticles	-
D	Crystallite size	-
A	Absorption	-
T	Transmittance	-
R	Reflectivity	-
K	Extinction coefficient	-
$n_\circ$	Refractive index	-
E	Photon energy	J
h	Plank's constant	J.s
v	Photon frequency	Hz
E_g	Band gap energy	eV
E_c	Conduction band	-
E_v	Valence band	-
eV	Electron Volt	-
XRD	X- ray diffraction	-
FTIR	Fourier Transform Infrared	-
FE-SEM	Field Emission Scanning Electron Microscopy	-
EDX	Energy Dispersive X-ray	-
TEM	Transmission Electron Microscopy	-

BET	Brunauer–Emmett–Teller theory	-
nm	Nanometer	-
mol.	mole	-
mW	Mille Watt	-
λ	Wavelength	nm
GRL	Maxilon blue dye	-
α	Absorption coefficient	cm^{-1}
UV	Ultra Violet	-
FWHM	Full Width at Half Maximum	-
ppm	Parts per million	-
C	BET constant	g/l, (Molary)
PDE(%)	Absorption efficiency	-

List of Tables

List of Figures

Chapter One

(Introduction)

Chapter One

Introduction

1.1 Introduction

In the early twentieth century to nowadays, we notice increase in the population, which is mainly connected with the increase in environmental pollution. Energy crisis and environmental pollution due to massive rise of population and extended industrialization have become the spotlight global issues since the hindmost of 20th Century [1].

Among the causes of increasing environmental pollution are factories, diesel generators, building materials, dust and means of transportation. Organic dyes and dye intermediates released in form of waste water from various industrial sites are contributing at large to organic pollution, causing constant human injury and harm to natural water bodies because of their carcinogenic and mutagenic nature [2–4].

When inadequately treated, these dyes can exist in environment for long duration of time. An instance is of Reactive Blue-19 dye with a half-life period of 47 years ($T = 25^{\circ}C$ and pH = 7) [5].

Non-pretreated effluent has significant negative impacts on human beings as well as on environment. Dye-containing wastewater can be treatment through the use of nanomaterial (catalyst).

Nanoparticles are the small particles with a big future because of their extremely small particle size, they have extremely large specific surface area. Hence they are chemically very active. They are stronger and more ductile. They have electronic states quite different from those of bulk.

Photocatalyst technology based on heterogeneous catalysis' principles stands among one of the promising strategies to pacify environmental damage by complete mineralization of organic pollutants on expense of earth-abundant solar energy [6–8].

Generally, heterogeneous photo catalysis refers to the acceleration of photo-reactions in presence of a semiconductor catalyst. Exploitation of low energy photons so as to contract maximum range of solar spectrum and reducing the recombination probability of photo excited charge carriers (e^-, h^+) to prolong the life span of transient reactive species are considered the best proposals to improve photo catalytic efficiency of a semiconductor [9].

When appropriate light energy photons illuminate the surface of semiconductor, it instigates the transfer of electrons from valence band (VB) to the conduction band (CB). This transfer leads to the generation of highly reactive Oxygen species of ephemeral nature (i.e., *OH, $*O_2^-$, $*OH_2$, H_2O_2) which set off the degradation of organic impurities on semiconductor surface without causing any secondary pollution [10–13].

Photo degradation activity of a semiconductor nanostructure is regulated by a number of factors including its composition, crystal structure, surface morphology, grain size, specific surface area, quantum efficiency and band gap position [14,15].

Zinc Oxide (ZnO) is a robust semiconductor material with a band gap of (3.37) eV which has been extensively explored for heterogeneous photo catalysis due to its non-toxic nature and easy availability [16].

Nevertheless, wide band gap of ZnO restricts its operational range to only UV region that is less than 5% of whole solar spectrum [16,17]. Yet, relatively fast recombination of photo-exactions (e^-, h^+) is another drawback associated with ZnO that lowers its photo catalytic performance [18].

One constraint associated with doping approach is that it can sometimes also reduce the redox potential of charge carrier species that results in decline of photo catalytic efficiency [19].

Further, high cost noble metal co-catalyst is less desirable to be used at commercial level as compared to cost-effective semiconductor materials. Therefore, a careful choice of coupling material is the key to get most appropriate photo catalytic design with maximum catalytic efficiency and practicability. Hence, in view of compatible band structure and low cost catalyst we have focused our attention on hybridize ZnO Nanoparticles with V_2O_5 Nanoparticles. V_2O_5 is a multi-functional n-type semiconductor material with a band gap energy (3.2) eV [20].

When V_2O_5 is coupled with ZnO, binary nanocomposites grasp better cumulative photo-efficiency than corresponding pristine nanostructures due to the formation of type-II heterojunction [21].

The photo catalytic activity of the catalyst was characterized by degradation of maxilon blue (GRL) dye under UV-visible light. The results obtained from this work are discussed in this thesis.

1.2 Catalysis

By adding a substance known as a catalyst which is not consumed during the reaction catalysis is the alteration and acceleration of the rate of a chemical reaction. By joining forces with one or more of the reactants, the catalyst contributes to the reaction and can play a role in selectively speeding one reaction in comparison to another.

Two key functions of catalysis in Nano science are as follows [22]:

(1) Some techniques for creating nanotubes, quantum dots, and various other nanostructures may involve catalysts.

(2) A few nanostructures may act as catalysts for other chemical reactions.

Catalysts play a very important role in modern science and technology as they improve reaction yields, reduce temperatures of chemical processes and promote specific enantioselectivity in asymmetric synthesis. There are two main types of catalysis, heterogeneous, where the catalyst is in the solid phase with the reaction occurring on the surface and homogeneous, where the catalyst is in the same phase as the reactants [23].

Both processes have their benefits, for example heterogeneous catalysts can be readily separated from the reaction mixture but the reaction rate is restricted due to their limited surface area [24].

Meanwhile homogeneous catalysts can react very fast and provide a good conversion rate per molecule of the catalyst, but since they are miscible in the reaction medium, it can be a painstaking process to remove them from the reaction medium [25].

The difficulty in removing homogenous catalysts from the reaction medium leads to problems in retaining the catalyst for reuse [26]. The separation and recycling of the catalyst is highly favorable since catalysts are often very expensive.

1.3 Nanoparticles

Nanoparticles (NPs) are wide class of materials that include particulate substances, which have one dimension less than 100 nm at least [27].

Depending on the overall shape these materials can be 0D, 1D, 2D or 3D [28]. The importance of these materials realized when researchers found that size can influence the physiochemical properties of a substance.

When well dispersed, the nanoparticulate catalyst forms a stable suspension in the reaction medium allowing an elevated rate of reaction. In addition, nanoparticles can permit additional catalytic functionalities due to their unique properties.

The bridge between heterogeneous and homogeneous catalysts can be achieved through the use of nanoparticles [29]. Nanoparticles of catalytic material provide the benefit of increased surface area which allows for an increased reaction rate [30].

1.4 Zinc Oxide (ZnO)

Among different semiconducting transition metal oxides, Zinc Oxide attracts attention in the scientific community for several decades for their wide band gap and tunable nanostructure [31].

Zinc Oxide is one of the most popular transparent semeconductive oxides having unique optical and electronic properties (wide energy band gap of 3.37 eV).

It is a white powder inorganic, it is insoluble in water, non-tox. Its melting point is extremely high 1975°C, ZnO exists in two common crystalline forms: wurtzite and Zinc blend. Wurtzite is more stable under ambient conditions. It has several applications like light emitting diodes, photocatalysis, sensors, fuel cells etc.

The photoluminescence emission as well as photocatalytic activity of ZnO largely depends upon the nanostructures of ZnO [32].

Both the photoluminescence emission and photocatalytic activity of ZnO varies with the variation of nanostructures, the change in nanostructures of ZnO depends upon several parameters like temperature, pressure, choice of precursor, methods of synthesis (sol-gel, hydrothermal, co-precipitation method, electrodeposition etc..), concentration of precursors etc.

Zinc acetate, zinc nitrate and zinc chloride are the three most widely used zinc sources for the preparation of ZnO nanoparticles as well as thin films. Several literatures reported the tunability of nanostructures of ZnO thin films using these three precursors [33,34].

Zinc Oxide exhibits high charge carrier mobility (from several to hundreds cm^2/Vs). However, its precise value strongly depends on its forms and dimensionalities directly related to the preparation and deposition methods [35].

The unique optical and electronic properties make zinc oxide a promising candidate mainly for selected optoelectronic devices and solar cells [36].

It plays an important role in a very wide range of applications, ranging from tyres to ceramics, from pharmaceuticals to agriculture, and from paints to chemicals. Fig. (1.1) shows worldwide consumption of zinc oxide by region [37,38].

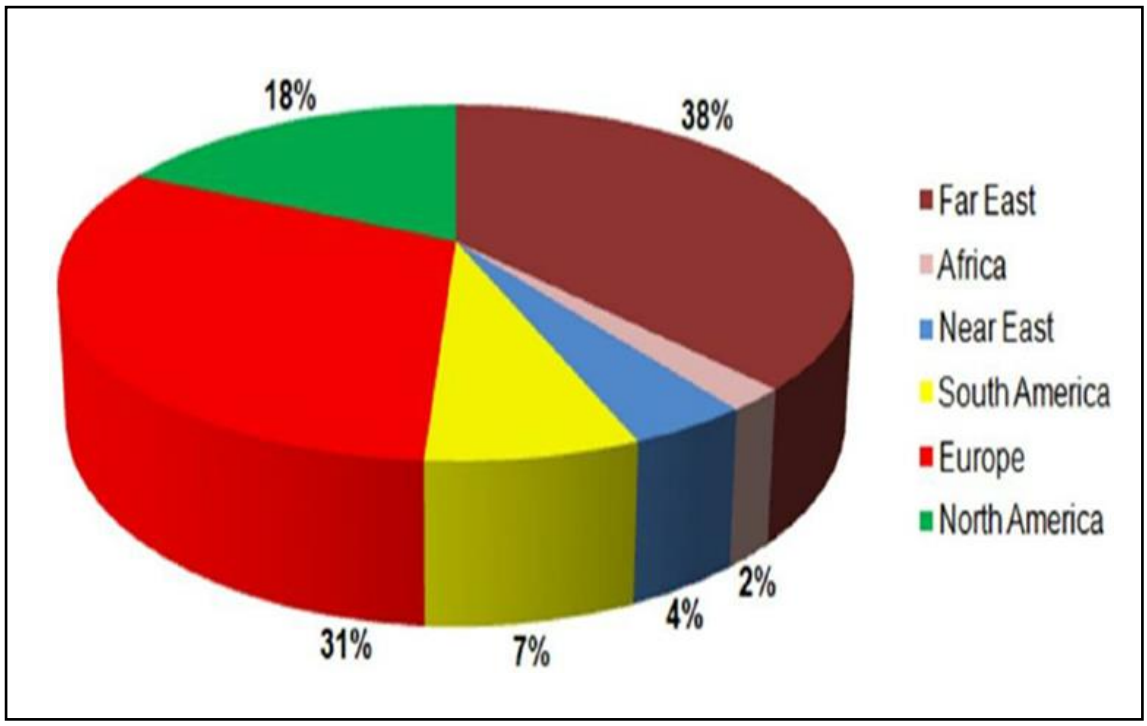

Fig. (1.1): Worldwide consumption of zinc oxide [37, 38].

1.5 Crystal Structure of ZnO

Three kinds of ZnO crystallization exist. They are cubic rock salt, hexagonal wurtzite, and cubic zinc blende. At the four corners of the tetrahedron, four cations surround each anion.

These materials also have a strong ionic character despite the typical sp^3 covalent bonding of this tetrahedral coordination. Fig. (1.2) depicts the ZnO crystal formations [39].

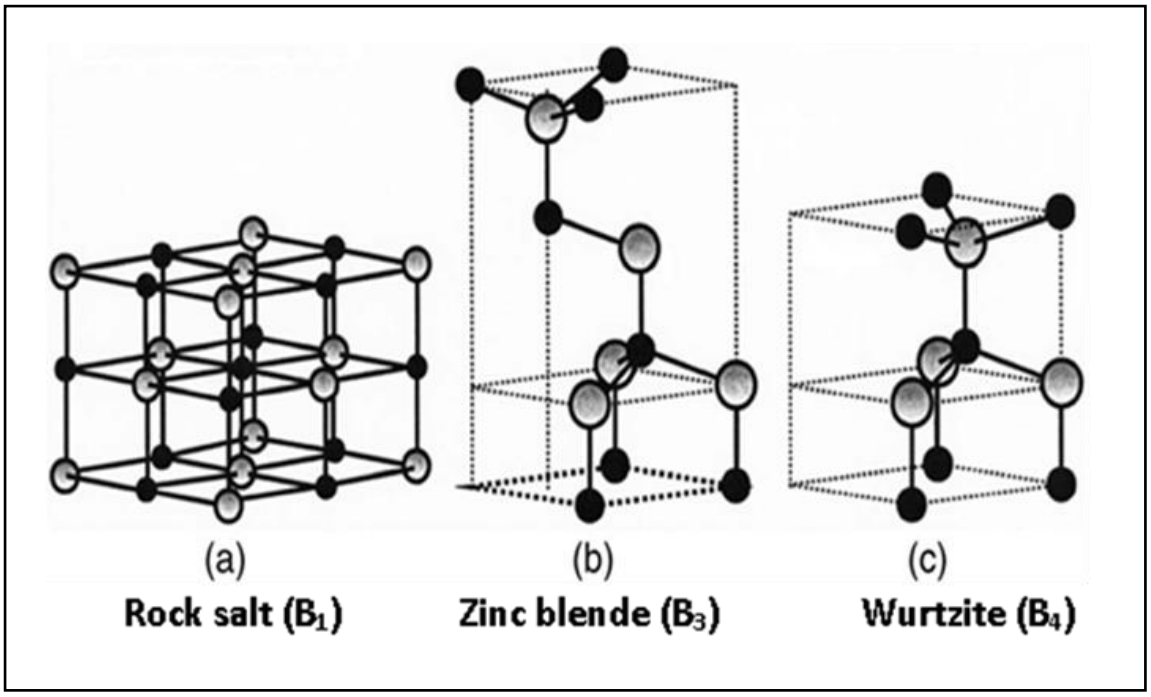

Fig. (1.2): ZnO crystals structure, the shaded gray and black spheres denote Zn and O atoms, respectively [39].

1-6 Vanadium Pentoxide

Vanadium pentoxide (V_2O_5) is a very useful semiconductor oxide material, used as an oxidising agent and amphoteric oxide material for industrial applications. It is a major compound of vanadium, used as an industrial catalyst.

It is a brown/yellow solid, although when freshly precipitated from aqueous solution, its color is deep orange. Because of its high oxidation state, it is both an amphoteric oxide and an oxidizing agent [40].

Orthorhombic phase of vanadium oxide (α-V_2O_5) is the most stable oxide and have tremendous research interest in the past years due to their excellent chemical and physical properties.

Especially the multi valence nature, layered structure, and excellent thermoelectric property are making vanadium pentoxide a fascinating material for nano-device fabrication prospective [41].

The preparation of composite materials with two transition metal oxide semiconductors possessing different energy band gap values provides an approach to attain more efficient charge separation, an increased lifetime of the charge carriers and an increased interfacial charge transfer to the adsorbed species.

1.7 Crystal Structures of V_2O_5

Vanadium pentoxide has the highest oxygen state in vanadium–oxygen systems and is the most stable member of the series of vanadium oxides.

Vanadium pentoxide has multiple distinctive polymorphs, including α-V_2O_5 (orthorhombic), β-V_2O_5 (monoclinic or tetragonal), and γ-V_2O_5 (orthorhombic).

Among them, the most common α-V_2O_5 is the thermodynamically stable phase (the unit cell structure) [42].

The orthorhombic structure of α-V_2O_5 is shown in Fig. (1.3), in which each single layer of V_2O_5 consists of edge- and corner-sharing square pyramids, and the adjacent layers are bonded together along the c-axis by weak Van der Waals bonds between the vanadium and oxygen of neighboring pyramids.

Additionally, three different oxygen's atoms, O_1, O_2, O_3, have different coordinations depending on the position in each layer. The triply coordinated O_3 links three vanadium atoms via edge-sharing V_2O_5 square pyramids [43].

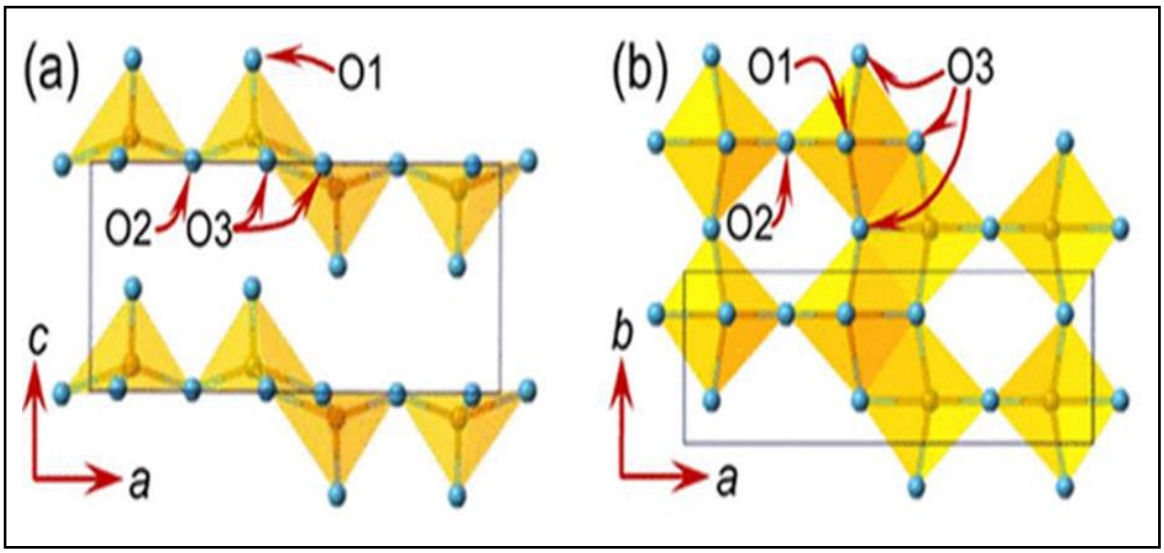

Fig. (1.3): Crystal structures of Vanadium pentoxide perspective view (a) along the b-axis, (b) along the c-axis of two layers of V_2O_5 [43].

1.8 Literature Survey

This literature survey aims to summarize some of the recent research studies that attracted much attention during last decade on the preparation and applications of ZnO NPs.

S. Chakrabarti, and B. K. Dutta, in (2004) [44] used ZnO as an effective catalyst for the photo degradation of two model dyes: Methylene Blue and Eosin Y. A 16W lamp was the source of UV-radiation in a batch reactor. The PCD efficiency has been generally, found to increase with increase in catalyst loading up to a limiting value, decrease in initial concentration, increase in airflow rate, pH, and UV light intensity. They found that this simple technology of PCD of the colored effluents has the potential to improve the quality of the wastewater from textile and other industries.

M. S. Akhtar, et al. in (2008) [45] found the morphology of ZnO materials could be controlled by changing the capping agent at constant alkali solution in hydrothermal process. ZnO nanomaterials with the structure of flowers, sheet-spheres and plates were obtained with the capping agent of ammonia, citric acid and oxalic acid, respectively. In dye-sensitized solar cell (DSSC) fabricated with sheet-sphere ZnO showed maximum conversion efficiency of 2.61% due to the uniform morphology with the high surface area and crystallinity, which lead to high dye absorption and less resistance to electron transfer. It is notable that the ZnO materials with sphere structure may be the optimal photo-anode material among various ZnO nanomaterials for DSSC.

R.Y. Hong, et al. in (2009) [46] synthesized ZnO nanoparticles by calcination of precursor prepared by the precipitation method. The influence of surface modification on the photocatalytic degradation of methyl orange has been analyzed. Experimental results show that well dispersed ZnO nanoparticles were obtained after surface modification. ZnO nanoparticles possess high photocatalytic activity, whereas the photocatalytic activity can be significantly reduced when polystyrene was grafted onto the particle surface. The photocatalytic activity of ZnO nanoparticles for some other azo dyes was also very high, which showed a good application foreground in organic contamination treatment.

R. Shidpour, et al. in (2014) [47] produced ZnO nanostructures with various morphologies in annealing temperatures ranging from (300 to 900) $^{\circ}$C.

The SEM images exhibit a variety of the as prepared hexagonal zinc oxides including wires, rods, particles and porous network of welded particles of ZnO nanoparticles. The results of the photocatalytic degradation of methylene blue as an organic dye in aqueous suspension showed that the morphology of ZnO nanostructures influences on the photocatalytic efficiency of ZnO nanostructures, greatly.

A. Moulahi and F. Sediri in (2014) [48] studied synthesized hexagonal zinc oxide nanoswords and nanopills via facile hydrothermal way. The reaction time plays an important role in the formation process and can affect the shape and size of the ZnO crystal. The values of the bandgap E_g for ZnO nanswords and nanopills are found to be 3.25 and 3.27 eV, respectively.

Haihong Yin, et al. in (2014) [49] successfully fabricated Au/V_2O_5/ZnO heteronanorods by an innovative four-step process: thermal evaporation of ZnO powders, CVD of intermediate on ZnO, solution deposition of Au NPs, and final thermal oxidization. show an enhanced photodegradation rate nearly 7 times higher than that of bare ZnO and nearly 3 times higher than that of V_2O_5/ZnO, mainly owing to the enlarged light absorption region, the effective electron–hole separation at the V_2O_5/ZnO and V_2O_5/Au interfaces.

M. Aslam, et al. in (2014) [50] synthesized V_2O_5/ZnO nanocomposites by co-precipitation technique. The characterization of the synthesized powders by FESEM, XRD and UV–visible diffuse reflectance spectroscopy (DRS) revealed that the both V_2O_5 and ZnO retain their individual identity in the composites but the increasing concentration of V_2O_5 affect the particle size of ZnO.

As estimated by photoluminescence spectroscopy, in comparison to pure ZnO, the presence of V_2O_5 significantly suppressed the charge carrier's recombination process.

O. Bechambi, et al. in (2015) [51] studied prepared different contents of silver on ZnO catalyst via hydrothermal method. The Ag doping enhances the photo catalytic and the antibacterial activities of ZnO.

R. Saravanan, et al. in (2015) [52] manufactured ternary ZnO/Ag/CdO nanocomposite was synthesized using thermal decomposition method. The ZnO/Ag/CdO nanocomposite exhibited enhanced photocatalytic activity under visible light irradiation for the degradation of methyl orange and methylene blue compared with binary ZnO/Ag and ZnO/CdO nanocomposites. The small size, high surface area and synergistic effect in the ZnO/Ag/CdO nanocomposite is responsible for high photocatalytic activity. These results also showed that the Ag nanoparticles induced visible light activity and facilitated efficient charge separation in the ZnO/Ag/CdO nanocomposite, thereby improving the photocatalytic performance.

A. Alshammari, et al. in (2015) [53] studied C-doped ZnO with large specific surface area was prepared via F127-assisted pyrolysis at 500°C and used for visible-light-responsive photo catalytic water purification. The band structure of the C-doped ZnO was investigated using valance band XPS and DFT simulation. The C-doped ZnO possessed enhanced absorption to UV and visible light, though it showed lower visible-light-responsive photo catalytic activity than ZnO because of significant recombination of photo generated charge carriers arisen from overloaded C-dopant and oxygen vacancies.

Xingang Kong, et al. in (2016) [54] used chemical in situ process was used for the synthesis of one-dimensional (1D) hetero-nanostructure $Ag/AgCl/V_2O_5$. The 1D $Ag/AgCl/V_2O_5$ hetero-nanostructures were characterized by XRD, XPS, FE-SEM and TEM. The 1D $Ag/AgCl/V_2O_5$ sample was able to well photodegrade RhB and the photodegradation rate reaches 93.8% after 180 min under visible light irradiation.

E. S. Gad, et al. in (2017) [55] synthesized binary composite consisting of Ag doped MnO_2 nanowires (NWs) and V_2O_5 nanorice (NRs) in 1:1 ratio was synthesized for photocatalytic treatment of Congo red (CR) dye and Pendimethalin (PM) herbicide. Physiochemical properties of the composite were determined by XRD, FT-IR, and SEM spectroscopy. $Ag/MnO_2/V_2O_5$ exhibited excellent chemical and photostability. These results proved $Ag/MnO_2/V_2O_5$ as potential photocatalyst for removal of various industrial and agriculture effluents.

Xiao-Dong Zhu, et al. in (2018) [56] studied delicate ternary nanostructures consisting of TiO_2 nanoplatelets co-doped with Ag and V_2O_5 nanoparticles. A remarkable synergistic effect among the three components, and the resulting delicate $Ag/V_2O_5/TiO_2$ ternary nanostructures exhibit a superior photocatalytic performance over neat TiO_2 nanoplatelets as well as Ag/TiO_2 and V_2O_5/TiO_2 binary nanostructures. delicate $Ag/V_2O_5/TiO_2$ ternary nanostructures may lay a basis for developing next-generating, high-performance composite photocatalysts.

S. Y. Sawant, et al. in (2018) [57] synthesized Ag/ZnO/C ternary photocatalysts showed a stronger interconnection among all the components, which allowed the easy transfer of photogenerated charges and provided enhanced charge carrier separation. Optical characterization showed that the enhanced absorption of visible light along with a decrease in the band gap and a red shift in the valence band maximum occurred due to the decoration of Ag-nanoparticles on ZnO/C. Ag/ZnO/C exhibited higher photocatalytic activity for the degradation of rhodamine blue and 4-nitrophenol under visible light irradiation than ZnO/C and bare ZnO without any significant loss after five successive cycles.

Juan Aliaga, et al. in (2018) [58] fabrication of the new heterojunction of two 2D hybrid layered semiconductors ZnO /V_2O_5 (hexadecylamine) and its behavior in the degradation of aqueous methylene blue under visible light irradiation. The optimal photocatalyst efficiency, reached at a ZnO /V_2O_5 (hexadecylamine) ratio of 1:0.25, results in being six times higher than that of pristine zinc oxide. Reusability test shows that after three photocatalysis cycles, no significant changes in either the dye degradation efficiency loss, nor the photocatalyst structure, occur.

S. Hamdy EL-Sheshtawy, et al. in (2019) [59] studied ternary nanocatalyst prepar by the facile immobilization of Ag NPs on the V_2O_5/g-C_3N_4 surface by photodeposition method. The morphology of the ternary nanostructure shows the uniform distribution of V_2O_5 on the g-C_3N_4 surface decorated with 20–30 nm average diameters of Ag NPs. The prepared catalyst exhibits unique catalytic, photocatalytic and post-oxidation/reduction ability for removal of organic, p-nitrophenol (NP), methylene blue (MB) and inorganic (Cr^{+6}) water pollutants.

Khac Lea, et al. in (2019) [60] fabricated vanadium pentoxide (V_2O_5) nanospheres and nanohollows by wet chemical reaction and hydrothermal methods, Reduced graphene oxide (RGO) was mixed with pure V_2O_5 nanostructures to form V_2O_5/RGO nanocomposites. This leads to the enhancement of the sunlight photocatalytic activity of the V_2O_5/RGO nanocomposites. The relation between the separation, diffusion, recombination, and degradation of the electron-hole pairs in the V_2O_5 nanostructures and V_2O_5/RGO nanocomposite is discussed.

A. S. Abed, et al. in (2020) [61] studied Synthesis of zinc oxide nanorods (ZnO NRs) using hydrothermal technique at different growth time. The structural and morphological properties were characterized by X-ray diffraction (XRD), Energy Dispersive X-Ray (EDX) and Field Emission Scanning Electron Microscope (FE-SEM). The ZnO NRs were obvious hexangular wurtzite structure and preferentially oriented along the c-axis (002) and growth vertically to the substrates. The optical properties were studied. From UV-Visible spectrophotometer and Photoluminescence (PL), the optical band gap energy of all ZnO NRs samples were calculated. Also, the effect of growth time on ZnO nanorods was studied.

S. Ameerah Jawad and Hazim Y. Al-gubury. in (2021) [62] studied photocatalytic degradation process of Safranin-T dye in this article has been investigated by using prepared nanocomposite and solar lamp. Zinc oxide/vanadium pentoxide nanocomposite was prepared using "hydrothermal processes". The degradation of dye was performed by irradiated aqueous suspended solutions containing different concentrations of dye using 0.2g/100 ml of nanocomposite.

The effect of various factors on the photocatalytic-degradation process of Safranin-T dye was tested to reach an optimal state, where they involve the effect of the nanocomposite mass and the effect of Safranin-T dye concentration the effect of light intensity and effect of temperature.

Faisal Mukhtar, et al. in (2021) [63] tri-phase direct dual S-scheme $ZnO/V_2O_5/WO_3$ heterostructured nanocomposite and pure ZnO, V_2O_5, and WO_3 nanoparticles were synthesized. The antibacterial test against Klebsiella pneumonia, Staphylococcus aureus, Proteus Vulgaris, and Pseudomonas aeruginosa bacteria showed higher activity. The photocatalytic performance of the $ZnO/V_2O_5/WO_3$ nanocomposite (99.8%) was the highest against methylene blue (MB) as compared to pure ZnO (78.8%), V_2O_5 (85.8%), and WO_3 (80.0%) under natural sunlight.

B. Dey, et al. in (2022) [64] investigated optical property through a UV–Vis spectrophotometer, indicates that the band gap has narrowed down upon the increase of Ag content. The transmittance value is found to increase drastically from 5% (for ZnO) to 55% (for 9% Ag/ZnO) compound. The frequency-dependent behavior of dielectric constant, dielectric loss, modulus spectroscopy, and ac conductivity of undoped as well as Ag/ZnO composite-like compounds has been analyzed and well explained with the help of the Maxwell-Weigner model.

Anqi Yang, et al. in (2022) [65] built three potential SCR catalyst models utilizing linear V_2O_5 and cyclic V_2O_5, respectively. Density functional theory was used to investigate the electronic structure and catalytic mechanism of the aforesaid catalysts (DFT). This V_2O_5/ZnV_2O_6 (0 0 1) model can realize the efficient separation of photogenerated carriers and has good redox ability.

Therefore, V_2O_5/ZnV_2O_6 (0 0 1) model has been proved to be an excellent photocatalyst in theory. This work is helpful to understand the effect of V_2O_5 modification on the photocatalytic activity of ZnV_2O_6 and provides a theoretical basis for the design of other vanadate high-performance catalysts.

N. Srinivasan alias Arunsankar, et al. in (2022) [66] synthesized carbon-doped ZnO (C–ZnO) with binary metal oxide semiconductor V_2O_5 has been done to hinder the limitations of both ZnO and V_2O_5 in the photocatalysis application. $C/ZnO/V_2O_5$ NPs photocatalyst exhibited improved catalytic performance over bare ZnO and V_2O_5. Based on the recycling experiments, the stability of the as-synthesized photocatalyst was confirmed toward the degradation of organic contaminants.

Nasser H. Shalaby, et al. in (2023) [67] prepared a composite photocatalyst from waste-extracted oxides, namely V_2O_5, Ag, and ZnO. The metal–lixiviant complexes were used as metal precursors, and their controlled thermal removal generates pores. The tri-constitute composite catalyst was doped with nitrogen. As did metal and metal-nonmetal co-doping. The efficiency of dye removal changes dramatically with time up to 120 min, after which it begins to decrease.

Ruijie Liu, et al. in (2023) [68] studied pure ZnO, Ag-doped ZnO, Ce-doped ZnO, and co-doped ZnO (Ag/Ce/ZnO) nano-photocatalysts synthesized by the hydrothermal method. Compared with pure ZnO, Ag-doped ZnO, Ce-doped ZnO, Ag/Ce/ZnO exhibited excellent photocatalytic performance due to their superior optical and photoelectrochemical properties.

Photodegradation experiment results revealed that the Ag/Ce/ZnO photocatalysts could degrade 97% of RhB dye within 30 min. Further, it was proved that the superoxide radicals played an active role in the photodegradation reaction. A possible mechanism of Ag/Ce/ZnO degradation was proposed.

Waseem Raza, et al. in (2023) [69] studied Ag/ZnO photocatalyst is synthesized in ethylene glycol (EG) medium using a one-pot hydrothermal method, where EG serves as both a reaction medium for the synthesis and a reduction medium for silver. The results show that spherical Ag/ZnO has the highest photocatalytic activity for H_2 evolution (30.1 μmol h^{-1}) and RhB degradation. This research could open up new avenues for the development of advanced ZnO-based visible light photocatalytic materials to address energy and environmental challenges.

E. Alzahrani, et al. in (2023) [70] developed photocatalytic activity of nanocomposite for the degradation of methylene blue (MB) dye, a primary textile industry released water-pollutant, was conducted under UV light irradiation. Meanwhile, the maximum % degradation of MB dye molecules was attained by 98.0 % after 60 min exposure of UV-light irradiation.

Increased photocatalytic activity of ZnO/Ag nanocomposites and a faster rate of MB degradation were achieved by the deposition of plasmonic Ag NPs and the surface plasmon resonance (SPR) effect possessed by Ag NPs.

S. Ganesan, et al. in (2023) [71] prepared V_2O_5/ZnO nanocomposites by a facile physico-chemical synthesis using V_2O_5 with ZnO through a high-energy ball miller technique. The 1:1 ratio of V_2O_5/ZnO nanohybrid composition material showed maximum potential (99.9% of methylene blue colour removal) in activating reactive hydroxyls from aqueous solutions for organic pollutant degradation. The experimental results proved that the developed physiochemical approach is a simple, low-cost, green methodology for synthesizing heterogenous V_2O_5/ZnO nanohybrid composite materials for environmental remediation and anti-microbial applications.

1.9 Aim of the Study

In order to investigate the reaction behavior of synthesizing ZnO nanoparticles as photocatalytic systems, this study has considered achieving the following:

1.Synthesising ZnO nanoparticles and V_2O_5/ZnO nanocomposites by eco-friendly method.

2. Preparing Ag/V_2O_5/ZnO nanocomposites by the photo-deposition method.

3. studying the characterization properties for these prepared nanoparticles such as Field Emission Scanning Electron Microscopy (FE- SEM), Surface Area Measurement (BET), X-ray Diffraction (XRD), Energy Dispersive X-ray Spectroscopy (EDX), Transmission Electron Microscopy (TEM), Fourier Transform Infrared Spectroscopy (FTIR) and Energy Band Gap.

4. Operating different parameters for photocatalytic degradation such as initial substrate concentration, incident light intensity, photocatalyst dosage, on the basis of the efficiencies of degradation.

5. Studying the photocatalytic activity of the prepared nanocomposites and comparing the photocatalytic performance of each nanocomposite.

6. studying the optical properties of synthetic nanocomposites and considering the difference in optical properties among the prepared nanocomposites.

Chapter Two

(Theoretical Part)

Chapter Two

Theoretical Part

2.1 The Hydrothermal Synthesis

Hydrothermal processing can be defined as any heterogeneous reaction in the presence of aqueous solvents or mineralizers under high pressure and temperature conditions to dissolve and recrystallize (recover) materials that are relatively insoluble under ordinary conditions.

Hydrothermal synthesis is one of the most commonly used methods for preparation of nanomaterials. It is basically a solution reaction-based approach. In hydrothermal synthesis, the formation of nanomaterials can happen in a wide temperature range from room temperature to very high temperatures. To control the morphology of the materials to be prepared, either low-pressure or high-pressure conditions can be used depending on the vapor pressure of the main composition in the reaction. Many types of nanomaterials have been successfully synthesized by the use of this approach. There are significant advantages of hydrothermal synthesis method over others [72].

Hydrothermal synthesis can generate nanomaterials which are not stable at elevated temperatures. Nanomaterials with high vapor pressures can be produced by the hydrothermal method with minimum loss of materials [73]. The compositions of nanomaterials to be synthesized can be well controlled in hydrothermal synthesis through liquid phase or multiphase chemical reactions [74].

The hydrothermal synthetic method is usually conducted in steel pressure vessels, i.e. autoclaves with the teflon liners under regulated pressure and temperature. This temperature can be increased from the boiling point of water up to saturation vapour pressure, but the pressure produced is also dependent on the amount of added solution [75].

This method involves the use of water as a catalyst and sometimes as a component of the formation of solids. This method is performed at high temperature (> 100°C) and high pressure (>1 atm).

It is one of the most common techniques used in the synthesis of homogeneous nanomaterials and is used in many different applications such as electronics, optoelectronics, catalysis, ceramics, magnetic data storage, biomedical, biophotonics, etc [76,77].

The synthesis of nanomaterials using this method depends on several variables such as temperature, process time, pressure, solvent type, and pH [78,79] .

Hydrothermal technique is not only helps in processing nano dispersed and highly homogeneous nanoparticles but also acts as one of the most attractive techniques for processing nanohybrid and nanocomposite materials.

The method is also particularly good for the growth of large good quality crystals while keeping control over their composition.

Disadvantages of the method involve the requirement of expensive autoclaves, and inability to observe the growth of crystals [80].

2.2 Dyes

Dyes are unsaturated and aromatic organic compounds that are able to absorb light radiation in the visible spectrum (400-700) nm and contain in their molecules a group called chromophores (color carriers) responsible for converting white light into colored light by reflecting on the body, or by transmission or diffusion by selective absorption of energy.

Dyes are groups of atoms that carry at least a double bond, and form with the rest of the molecule a conjugated sequence, and other groups called exochromes of an acidic or basic nature that intensify the color and fix it effectively on the treated supports.

Dyes can be classified based on their composition, functional group, or ion charge when they dissolve in water, and since the ion charge has a major role in the adsorption process, will classify them accordingly. It can be divided into ionic dyes and non-ionic dyes [81, 82].

2.3 Maxilon Blue (GRL)

The maxilon blue (GRL) is a basic cationic dye. The solution is blue in color. Chemical formula: $C_{20}H_{26}N_4O_6S_2$, λ_{max} =590 nm, and the chemical structure as shown in Fig. (2.1) [83,84].

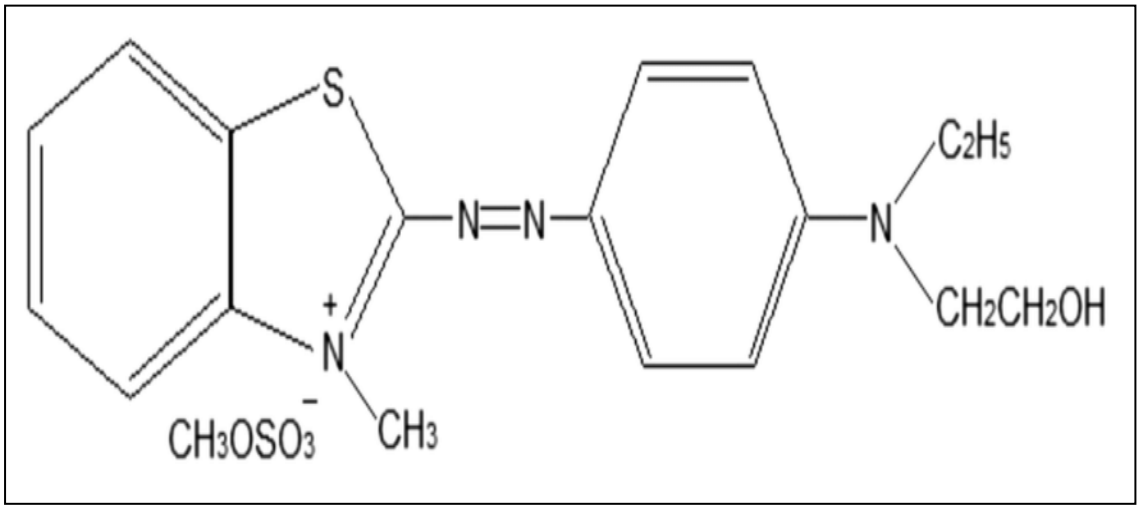

Fig. (2.1): Chemical structure of maxilon blue (GRL) [83,84].

2.4 Advanced Oxidation Processes (AOPs)

One of the best methods for destroying pollutants with less harmful products is the AOPs processes whose processer involves the generation of hydroxyl radicals ($O\dot{H}$) which oxidizes the pollutants [85].

The hydroxyl radical is the second strongest known oxidant that has an oxidation potential of (2.8) eV. This oxidant is capable of oxidizing and mineralizing almost every organic molecule, yielding CO_2 and inorganic ions as shown in Eqs. (2.1) and (2.2)

$$O\dot{H} + RH \rightarrow \dot{R} + H_2O \quad (2.1)$$

$$\dot{R} + O_2 \rightarrow R\dot{O}_2 \text{ Products and } CO_2 \quad (2.2)$$

where $O\dot{H}$ is hydroxyl radical, RH is organic molecule, $R\dot{O}_2$ is inorganic ion, H_2O is water, CO_2 is carbon dioxide.

2.5 Composite of Nanoparticles

A composite material (also called a composition material or shortened to composite, which is the common name) is a material which is produced from two or more constituent materials.

These constituent materials have notably dissimilar chemical or physical properties and are merged to create a material with properties unlike the individual elements.

Within the finished structure, the individual elements remain separate and distinct, distinguishing composites from mixtures and solid solutions. The reason for their use over traditional materials is because improve the properties of their base materials and are applicable in many situation [86].

Composite nanoparticles are advanced materials have recently gained increasing attention due to their scientific and technological importance and because of it wide variety of applications such as catalysts with huge activity and specificity, metal semiconductor junctions, optical sensors, and modifiers of polymeric films for packaging. From a scientific point of view the composition and the atomic order of the aggregates, in addition to size, are pivotal factors in determining their properties and functionalities, while the nanoscale regime confers to them structural and electronic degrees of freedom which are inaccessible to bulk materials.

2.6 Structural Properties

The crystal structure, surface morphology, and particle size can be precisely determined using the characterization methods, the results of which reveal details on the various structural characteristics.

2.6.1 X-rays Diffraction (XRD)

The production of materials with specified morphologies has drawn a lot of attention for scientists in the recent years since the characteristics of nano- and micro-structures are highly reliant on their forms and sizes. Results from X-ray, diffraction patterns are typically used to investigate the structural properties of such materials [87].

The evaluation of crystallite sizes in the nanoscale range necessitates precise analytical abilities, and the most common method for estimating crystallite size in nanomaterials and one that has been extensively employed in the current work is X-ray diffraction analysis.

The growth of the crystallite refinement and internal strain are responsible for the Bragg peaks' enlargement. Size broadening and stain broadening are determined by analyzing the full width at half maximum (FWHM) of the Brag peaks as a function of the diffraction angle.

2.6.2 Crystallite Size

The information that the obtained diffraction pattern provides us, we can find from it the rate at which the crystals grew inside the crystal lattice, so we find the rate of particle size by adopting the Scherer's formula, as we can find the amount of exposure for the characteristic peaks (β) depending on the amount of width of the middle of the peak (FWHM) (Full Width at Half Maximum) measured in radial units (rad) so the crystal size measured in nm according to the following equation [88,89]:

$$D = 0.94\lambda/\beta_{FWHM}\, cos\theta \qquad (2.3)$$

Where λ is the wave length of incident X-ray radiation (λ = 0.15406 nm), β_{FWHM} is the intrinsic (FWHM) of the peak, and θ is the Bragg's diffraction angle of the respective XRD peak. It is used to estimate the size of very small crystals from measured width of their diffraction curves.

2.6.3 Field Emission Scanning Electron Microscopy(FE-SEM)

It's the perfect analytical method for describing and displaying the elemental makeup of a material [90]. With a spatial resolution of about 1 nm and a variety of other benefits, it performs significantly better at low accelerating voltages [91].

Due to the ability to capture high-magnification images in high-vacuum conditions, it has recently gained in popularity.

This method is widely employed in the fields of metals, semiconductors, ceramics, medicine, and biology [92].

The characteristics of FE-SEM enable the development of novel methods for life science studies, based on the production of clearer, less electrostatically distorted images with spatial resolution down to 1/2 nm, (3–6) times better than conventional FE-SEM, reduced penetration of low kinetic energy electron probes closer to the immediate material surface, and the ability to detect smaller-area contamination spots.

Despite the FE-SEM sophisticated capabilities, no study has yet demonstrated how to use it to precisely localize nanoparticles inside cells using their ultrastructure.

2.6.4 Energy Dispersive X-ray Spectroscopy (EDX)

The elemental composition of a sample can be determined using the analytical method known as energy dispersive X-ray spectroscopy (EDX).

It is based on the examination of a sample by the analysis of X-rays produced by the material in reaction to being struck by charged particles and the interactions between electromagnetic radiation and matter.

When a sample is subjected to an electron beam during (EDX), the electrons in the sample collide and some of them are thrown out of their orbits as a result.

Higher energy electrons fill the vacant sites, producing X-rays as they do so. The elemental composition of the sample can be ascertained by examining the x-rays that were emitted.

This method makes it easy to do a constitutional analysis on any type of content. The ability to characterize materials is made possible by the fact that every element has a distinct atomic structure that makes it possible to distinguish one element's characteristic X-rays from another [93].

2.6.5 Transmission Electron Microscopy (TEM)

Transmission electron microscopy (TEM) is a fast-growing and fascinating area of research that has drawn tremendous attention from various fields ranging from materials science to chemistry and biology as a powerful and indispensable tool for nanomaterials characterization. TEM provides great opportunities to characterize dynamic changes in size, shape, interface structure, electronic state, and chemical composition of materials at and below the nanoscale [94].

Transmission electron microscopy (TEM), together with its associated techniques, is one of the most versatile characterization methods. In short, it can be described as analysis of the interactions between high energy electrons, usually between (60-300) keV, and a thin electron transparent sample.

This interaction may generate a number of different signals, which can be used for composing images, diffraction patterns and spectroscopic analyses. Consequently, TEM techniques can provide information on the sample’s microstructure, chemical composition and electronic properties.

As the TEM instrumentation allows the simultaneous acquisition of the signals generated during the electron beam and sample interaction, a comprehensive sample characterization is possible by the use of TEM [95].

Transmission electron microscopy (TEM) has the advantage over FE-SEM that cellular structures of the specimen can be viewed at very high magnifications. Pointed out that perhaps the least forgiving of all the steps in TEM is the sample processing that occurs prior to sectioning. In other words, a poorly prepared specimen is useless to the investigator [96].

Transmission electron microscopy (TEM) provides powerful techniques for understanding various information of materials at very high spatial resolution, including morphology, size distribution, crystal structure, strain, defects, chemical information down to atomic level and so on.

All the information that TEM can give to us are from electron-sample interaction. The transmitted electrons that have passed through the thin sample are detected to form images, which is the reason to call it "transmission" electron microscopy.

In order to allow electrons to transmit through the sample, TEM sample must be very thin (typically, sample diameters is less than 200 nm, depending on the composition of sample and the expected information from TEM characterization) [97].

In a transmission electron microscope (TEM), a beam of electrons is transmitted through the material under investigation, refocused, magnified by an electromagnetic lens system, and projected onto a phosphor screen to convert the electron image to a visible image. TEM works on the same principles as SEM, but differs from SEM in two aspects:

Firstly, TEM uses high acceleration voltage (100–300) kV to get clear, high-resolution images, usually in the range of (0.1–0.2) nm [98].

Secondly, the signal collected for image information consists of transmitted electrons (bright-field imaging), thus it can be used only for thin samples, usually less than 100 nm in thickness.

2.7 Brunauer–Emmett–Teller (BET) Theory

Brunauer–Emmett–Teller theory is a well-known rule for the physical adsorption of gas molecules on a solid surface. In 1938, Stephen Brunauer, Paul Hugh Emmett, and Edward Teller presented their theory in the Journal of the American Chemical Society [99].

Brunauer–Emmett–Teller (BET) theory aims to explain the physical adsorption of gas molecules on a solid surface and serves as the basis for an important analysis technique for the measurement of the specific surface area of materials. The observations are very often referred to as physical adsorption or physisorption.

Brunauer–Emmett–Teller theory applies to systems of multilayer adsorption that usually utilizes a probing gas (called the adsorbate) that does not react chemically with the adsorptive (the material upon which the gas attaches to and the gas phase is called the adsorptive) to quantify specific surface area. Nitrogen is the most commonly employed gaseous adsorbate for probing surface(s).

For this reason, standard BET analysis is most often conducted at the boiling temperature of N_2 (77 K). Other probing adsorbates are also utilized, albeit less often, allowing the measurement of surface area at different temperatures and measurement scales.

These include argon, carbon dioxide, and water. Specific surface area is a scale-dependent property, with no single true value of specific surface area definable, and thus quantities of specific surface area determined through BET theory may depend on the adsorbate molecule utilized and its adsorption cross section [100].

2.8 Fourier Transform Infrared Spectroscopy (FTIR)

Fourier Transform Infrared spectroscopy (FTIR) is a technique based on the vibrations of the atoms within a molecule. An infrared (IR) spectrum is obtained by passing IR radiation through a sample to determine what fraction of the incident radiation is absorbed at a particular energy. The chemical bonds in different environments will absorb various intensities and at various frequencies.

Thus IR spectroscopy involves collecting absorption information and analyzing it in the form of a spectrum, where the frequencies at which there are absorptions of IR radiation (peaks or signals) can be correlated directly to bonds within the compound [101].

Fourier Transform Infrared spectroscopy is the most useful for identifying chemicals that are organic. It can be utilized to get information of some components of an unknown mixture. It can be applied to the analysis of solids, liquids, and gasses.

Fourier Transform Infrared spectroscopy this term refers to a fairly recent development in the manner in which the data is collected and converted from an interference pattern to a spectrum. FTIR can be used to identify chemicals from spills, polymers, drugs, paints, coatings and contaminants.

Fourier Transform Infrared is also a powerful tool for identifying types of chemical bonds (functional groups). The wavelength of light absorbed is a characteristic of the chemical bond. By interpreting the infrared absorption spectrum, the chemical bonds in a molecule can be determined.

Fourier Transform Infrared spectroscopy spectra of pure compounds are generally so unique that they are like a molecular "fingerprint". For most common materials, the spectrum of an unknown can be identified by comparison to a library of known compounds.

2.9 Band Gap Energy in Semiconductor

A semiconductor is a material with an intermediate-sized, non-zero band gap that behaves as an insulator at T=0 K, but allows thermal excitation of electrons into its conduction band at temperatures that are below its melting point.

In semiconductors, electrons are confined to a number of bands of energy, and forbidden from other regions because there are no allowable electronic states for them to occupy. The term "band gap" refers to the energy difference between the top of the valence band and the bottom of the conduction band. Electrons are able to jump from one band to another.

However, the highest energy band that is filled with electrons is called the valence band. The next higher band that is empty is called the conduction band. The energy separation between these bands is called the band gap [102].

In order for a valence band electron to be promoted to the conduction band, it requires a specific minimum amount of energy for the transition.

This required energy is an intrinsic characteristic of the solid material, electrons can gain enough energy to jump to the conduction band by absorbing photon (light) [103].

The conductivity of intrinsic semiconductors is strongly dependent on the band gap. The only available charge carriers for conduction are the electrons that have enough thermal energy to be excited across the band gap and the electron holes that are left off when such an excitation occurs [104].

Band-gap engineering is the process of controlling or altering the band gap of a material by controlling construct layered materials with alternating compositions by techniques.

When temperature increases, the amplitude of atomic vibrations increase, leading to larger interatomic spacing. The interaction between the lattice phonons and the free electrons and holes will also affect the band gap to a smaller extent [105].

Band gap measurement is critical for understanding the fundamental properties of materials in the semiconductor industry. For narrow band gap materials in the visible region of the electromagnetic spectrum, optical methods are ideal for measuring the band gap through optical reflection, absorption, and ellipsometry.

For wide band gap materials, electron spectroscopy methods are more suitable. For example, reflection electron energy loss spectroscopy and transmission electron energy loss spectroscopy can be used to measure band gap and the dielectric function [106].

2.10 Optical Properties

Numerous pieces of information can be found in optical characteristics, including optical absorption, photoluminescence, reflection, transmission, and more [107].

Both intrinsic and extrinsic influences play a role in a semiconductor's optical characteristics. The excitonic effects resulting from the Coulomb interaction are also taken into account when treating the transitions between electrons in the conduction band and holes in the valence band as intrinsic optical transitions [108].

Extrinsic characteristics have to do with the electronic states that dopants, impurities, point defects, and complexes, which affect optical absorption as well as emission, generate in the band gap. The study of the optical properties is of great importance in finding the optical constants through which it can be used.

In addition to being aware of the other constants for absorption, transmittance, and reflectivity and their coefficients, as well as the extinction coefficient and refractive index, one must determine the optical energy gap value in accordance with the particular preparation conditions.

2.10.1 Absorbance of UV-Visible Light

Absorbance is the amount of light captured by a substance or an object at a specific wavelength, it is symbolized by the symbol (A) [109].

When studying the absorption spectrum, must to verify the practical benefit that enables us to use the prepared nanocomposite for its intended applications.

Absorbance depends on the energy of the photons falling on the material and on the type of material and the nature of its crystalline structure [110].

2.10.2 Transmittance of Light

The transmittance represents (T) is the ratio between the intensity of radiation transmitting through the sample to the intensity for incident radiation [111]. It can be presented as,

$$T = e^{-2.303A} \tag{2.4}$$

where, T is transmittance, A is absorption.

2.10.3 Reflectivity

The reflectivity (R) defined as the ratio between the intensity of radiation reflected from the sample in a certain direction to the intensity of incident radiation, and its value can be given as, [112].

$$R = 1 - T - A \tag{2.5}$$

where, R is reflectivity.

2.10.4 Optical Absorption

Optical absorption is one of the important and effective studies in the field of semiconductor physics, the absorption processes of semiconductors depend on the energy of incident photons and the optical energy gap.

The incidence of electromagnetic radiation with an energy greater or equal to the value of the energy gap of the material whose thickness (t) leads to the absorption of part of this incident ray.

If the intensity of the incident ray $I_\circ$ and the intensity of the transmitted ray I_T, this enables us to find the relationship by which calculate the absorption coefficient (α), according to the following equation [113, 114]:

$$I_T = I_\circ e^{-\alpha t} \quad (2.6)$$

As α is the absorption coefficient, measured in cm^{-1}, which is the ratio of the decrease in the incident radiation energy, and it changes according to the change in the wavelength of the incident rays and the nature of the material, $I_\circ$ intensity of incident radiation, I_T intensity of transmitting radiation and t is material thickness.

If the incident rays have an energy greater than or equal to the energy gap of the semiconductor, an electron in the valence band is excited and moves to the conduction band, creating a hole in the valence band. The energy of the incident ray can be calculated from the relationship [111]:

$$E = hv \quad (2.7)$$

where E is the energy of the incident photon, v is photon frequency and h is Planck's constant.

To calculate the absorption coefficient, we start by calculating the absorbance of the incident rays such that. The value of the absorption coefficient (α) can be given from the following equation:

$$\alpha = 2.303\ (A/t) \quad (2.8)$$

2.10.5 Extinction Coefficient

It is defined as the amount of energy absorbed by the valence electrons when the electromagnetic radiation falls. on the material, that is, the amount of energy that these electrons extinguished from the incident rays, or the amount of attenuation in the energy of the incident rays.

Depends on the wavelength of the incident rays and the value of the coefficient absorption (α) for each substance. The extinction coefficient can be calculated from the following relationship [112]:

$$K = \alpha\lambda/4\pi \tag{2.9}$$

where, K is extinction coefficient.

2.10.6 Optical Energy Gap

The energy gap of a semiconductor material is the amount of energy it takes for an electron to travel from the top of a band valence to the bottom of the conduction band or the local plane closest to the transition, and the width of this gap is affected the percentage of impurities added to the semi-conducting material (the membrane material) and the temperature, where increase or decrease according to the type of semi-conducting material, so it increases in some and decreases in others [115].

The value of the energy gap is calculated from the experimental Tauc equation as [116].

$$(\alpha hv)^{1/n} = C_x(hv - E_{\mathrm{bg}}) \tag{2.10}$$

where (ν = c/λ), c speed of light. n = ½, 2 for allowed direct and indirect band gap, respectively, c_x is proportionality constant, and E_g is band gap [117].

A graphic relationship is drawn between the amount of energy of the incident photons (hν) for the x-axis and the amount of $(\alpha hv)^2$ of the y-axis, the amount of the energy gap is determined by projecting a tangent line to the resulting curve in the direction of the x-axis, cuts it at the point $(\alpha hv)^{1/n}$ =0, and this point represents the value of the energy gap [116].

2.10.7 Refractive Index ($n_\circ$)

The ratio between the speed of light in a vacuum to its speed in any other physical medium is called by the coefficient of the refraction that can be found based on knowing the value of the quenching constant (K) and the value of the reflectivity R. Its value will be according to the equation: [112].

$$n_\circ = [\{(1+R)/(1-R)\}^2 - (K^2+1)]^{1/2} + \{(1+R)/(1-R)\} \qquad (2.11)$$

Chapter Three

(Experimental Details)

Chapter Three

Experimental Details

3.1 Introduction

This chapter concentrates on the description of preparation of ZnO nanoparticles, V_2O_5/ZnO nanoparticles and Ag/V_2O_5/ZnO nanoparticles, Chemicals, apparatus and the hydrothermal technique for preparation of nanoparticles and then discusses what diagnostic tools to examine these parameters.

3.2 Chemicals and Equipment

3.2.1Chemicals

Several chemical compounds were used in this study. Table (3.1) shows the chemical compounds as well as the molar mass and purity provided by the supplier

Table (3.1) The chemicals compounds used in this work

NO.	Chemicals	Chemical formula	Molar mass g/mol	Supplier	Purity (%)
1	Ammonium Metavanadates	NH_4VO_3	116.98	Sigma-Aldrich	**99.0**
2	Aqueous Ammonia	NH_3	17.03	Sigma-Aldrich	**99.0**
3	Methanol	CH_3OH	32.04	Alpha Chemika	**98.0**
4	Sodium Sulfate	Na_2SO_4	142.04	Alpha Chemika	**98.0**
5	Silver Nitrate	$AgNO_3$	169.87	Sigma-Aldrich	**99.0**
6	Zinc Acetate	$ZnC_4H_6O_4$	183.48	Sigma-Aldrich	**99.0**
7	Oxalic Acid	$C_2H_2O_4$	90.03	Alpha Chemika	**98.0**

3.2.2 Equipment Instrument

Different instruments were used in this study. Table (3.2) show this instruments with supplying companies.

Table (3.2): list of instruments used in this project.

No.	Instrument	Company supplied	Location of current measurement
1	UV-Visible spectrophotometer, Single beam	Shimadzu, Japan	University of Babylon / College of science for women
2	Field-Emission Scanning Electron Microscope (FE-SEM)	Fei, Netherlands	Baghdad/AlKhora Company
3	Transmission Electron Microscope (TEM)	Leo, Germany	University of Tehran
4	X-Ray Diffraction (XRD)	Japan	Ministry of Science and Technology/ Iraq
5	Fourier Transform Infrared (FTIR)	Shimadzu, Japan	University of Babylon / College of science for women
6	Centrifuge	JANETZI - T5, Belgium	University of Babylon / College of science for women
7	Ultrasonic Cleaner (Power Sonic 420)	Hwashin, Korea	University of Babylon/ College of science
8	Oven	Labtech, Korea	University of Babylon / College of science for women
9	Sensitive Balance	Denver instrument , Germany	University of Babylon / College of science for women
10	Energy Dispersive X-Ray (EDX)	Thermoscientific-Axia, Northlands	Baghdad/AlKhora Company
11	BET Surface Area Analyzer	Quantachrome, Autosorb iQ	University of Tehran

3.3 Preparation of ZnO NPs.

Zinc oxide compound was preparing in an acidic medium has by the method of hydrothermal synthesis in the presence of an aqueous solvent only, through thermal hydrolysis of Zinc acetate ($ZnC_4H_6O_4$), which is one of the modern methods in the world .

These experiments have been carried out in a 150 mL teflon cup enclosed in a stainless-steel autoclave (Berghof, DAB-3).

In all experiments, 75 mL of Zinc acetate aqueous solution (4g $ZnC_4H_6O_4$, 75 ml water), in presence of 75ml of an oxalic acid solution (5 g Oxalic acid, 75 ml water), are mixed. Then, this solution has been mixed very well for 1-2 hrs to get a homogeneous solution .

The resulting solution was transferred into the teflon cup, the teflon cup sealed in the autoclave, which closed and placed into an electric furnace held at 160°C for 24 hrs .

The autoclave was cooled down to ambient temperature, the solution then washed for 3-4 times with deionized water and set in drying oven at 60°c until all the water evaporated .

After that, it was grinded and placed in an oven for burning for 2 hrs at 500°C [118].

The white powder obtained is subjected to annealing at 500°C. The preparation method is illustrated in Fig. (3.1). on the other hand, Fig. (3.2) shows a laboratory picture of ZnO NPs that have been obtained after the preparation process. The confirmation of pure ZnO phase is verified by XRD and EDX analysis .

The shape and morphology of the particles are studied by FE-SEM, absorption spectroscopy and Fourier transform infrared spectroscopy has been performed.

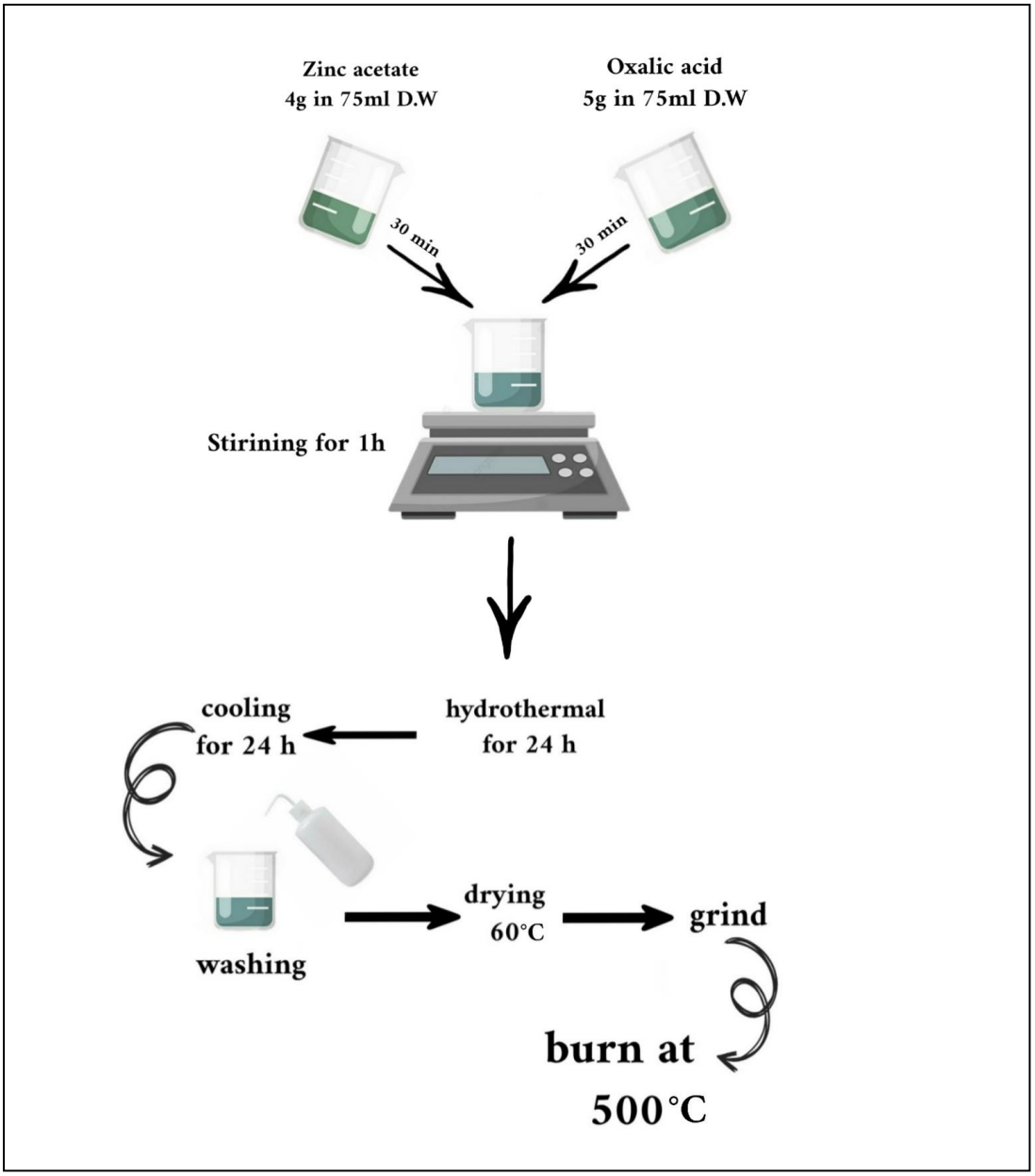

Fig. (3.1): Diagram of preparation of ZnO NPs.

Fig. (3.2): Images of the preparation of ZnO NPs.

3.4 Preparation of Vanadium Pentoxide for Zinc Oxide V_2O_5/ZnO NPs.

Vanadium pentoxide for zinc oxide V_2O_5/ZnO nanoparticles have been prepared by thermal hydrolysis of ammonium metavanadates (NH_4VO_3). These experiments were carried out in a 150 mL Teflon cup enclosed in a stainless-steel autoclave (Berghof, DAB-3).

In all experiments, 25 mL of ammonium metavanadates aqueous solution (0.5 g NH_4VO_3, 25 ml water), in the presence 75 ml of an aqueous zinc acetate solution (20.6 g zinc acetate, 75 ml D.W), they have been mixed. Then, this solution was mixed very well for further 60 minutes.

Followed by the addition 6.3 g of Oxalic acid and 65 ml of Aqueous ammonia 25% to the mixture.

Then this solution was mixed very well for further 120 minutes, the resulting solution has been transferred into the teflon cup.

Afterward, the teflon cup was sealed in the autoclave, which is closed and placed into an electric furnace held at 160°C for 24 hrs [119].

Finally, the autoclave was cooled down to ambient temperature. The solution was washed 3-4 times with deionized water and placed in drying oven at 60° C until all the water evaporated. After that, it was grinded and placed in an oven for burning for 2 hrs at 500°C .

The colour of the white powder has been changed to almost orange when subjected to annealing at temperature 500°C. Fig. (3.3) shows images of V_2O_5/ZnO nanoparticles and the preparation method is illustrated in Fig. (3.4). The confirmation of pure V_2O_5/ZnO phase was verified by XRD and EDX analysis. The shape and morphology of particles are studied by FE-SEM, absorption spectroscopy and Fourier transform infrared (FTIR) spectroscopy is performed.

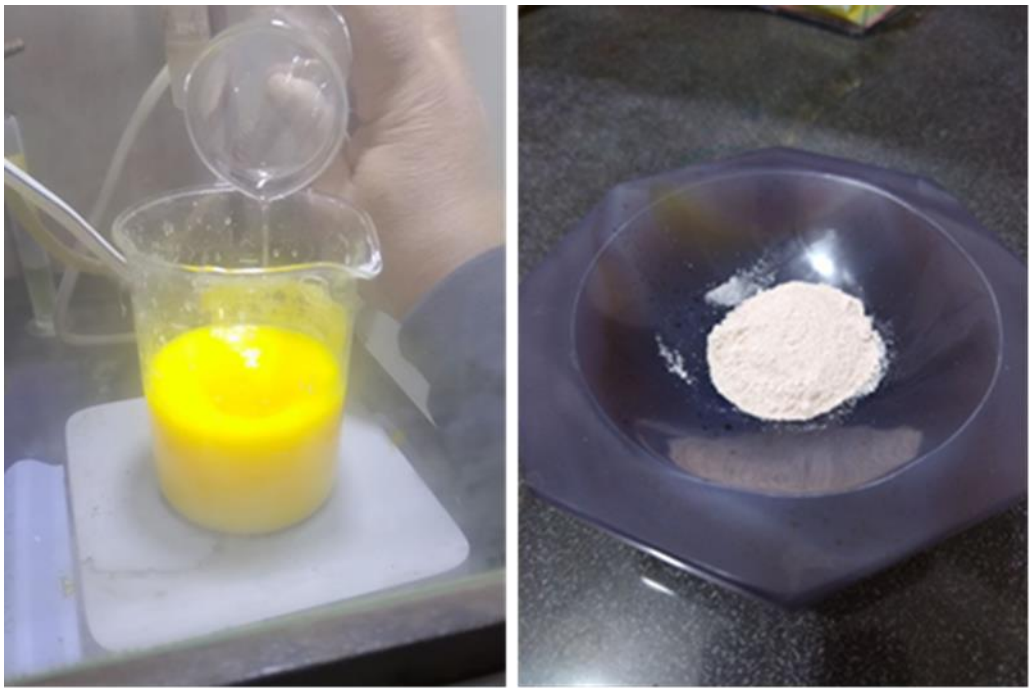

Fig. (3.3): Images of preparation of V_2O_5/ZnO NPs.

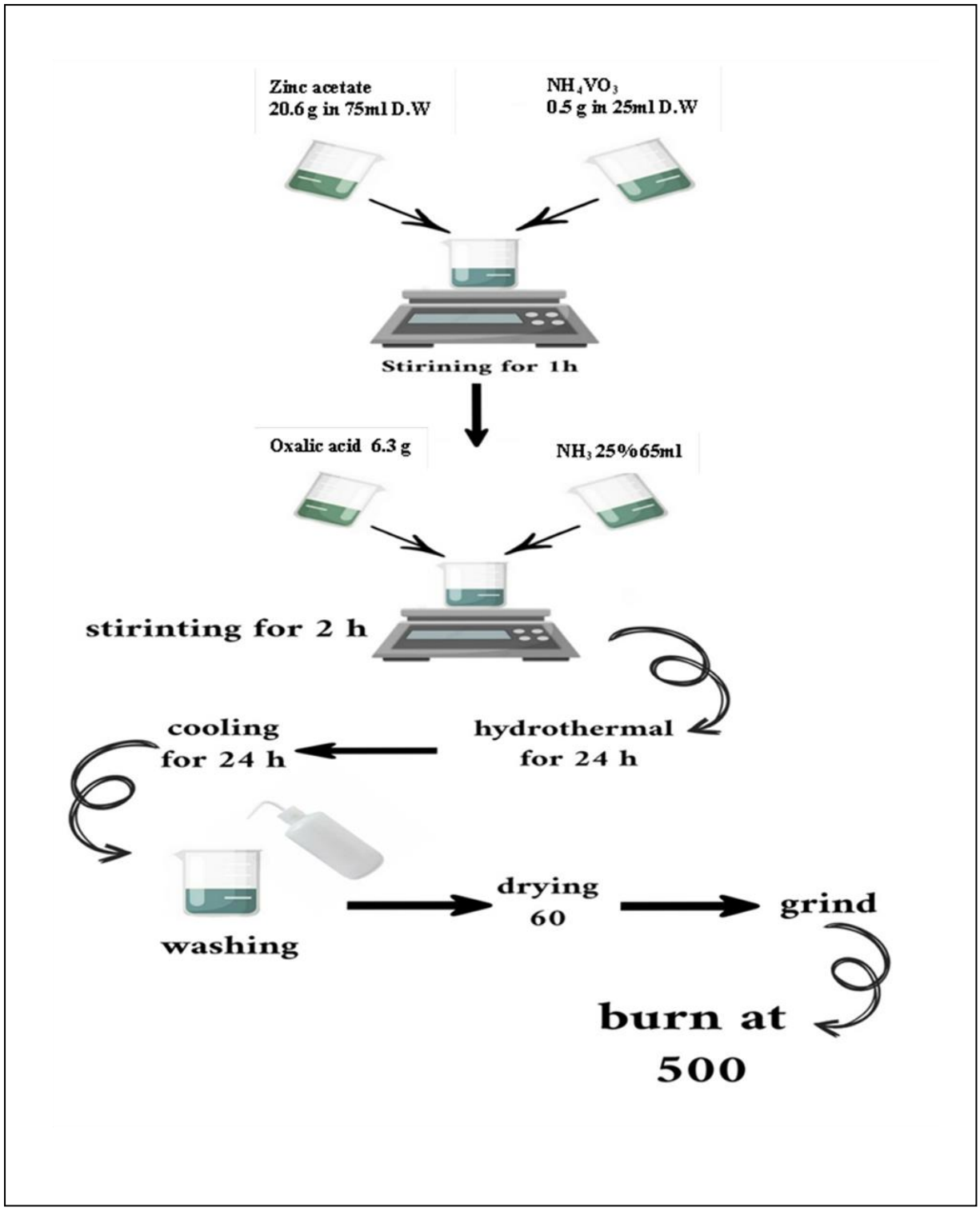

Fig. (3.4): Diagram of preparation of V_2O_5/ZnO NPs.

3.5 Preparation of Silver(Ag) Doped V_2O_5/ZnO NPs.

Silver deposited on V_2O_5/ZnO Nanoparticle was prepared by placed (0.5-1) g of V_2O_5/ZnO NPs and added (1-2) ml of methanol and the deionized water (100-200) ml in a quartz cell, pargulated by N_2 (Nitrogen gas) for (5) minutes, and added (1.5-2.5) ml of $AgNO_3$ the system was irradiated with UVA light wavelength 365 nm and light intensity of 1.71 mw/cm^2 under continuous magnetic stirring for 24 hrs [120].

The resulting powder was washed several times with deionized water and dried for 24 hrs in an oven at 60°C, to obtain the nanoparticles of Ag/V_2O_5/ZnO as shown in Fig. (3.5) as well as the preparation method illustrated in Fig. (3.6).

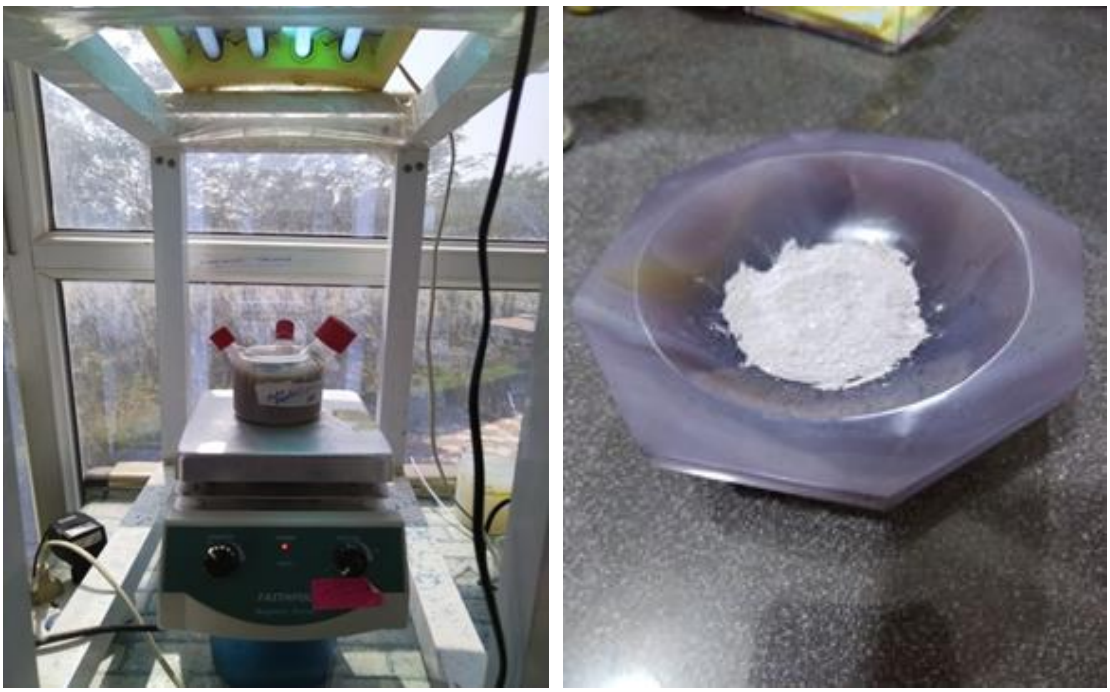

Fig. (3.5): Images of preparation of Ag/V_2O_5/ZnO NPs.

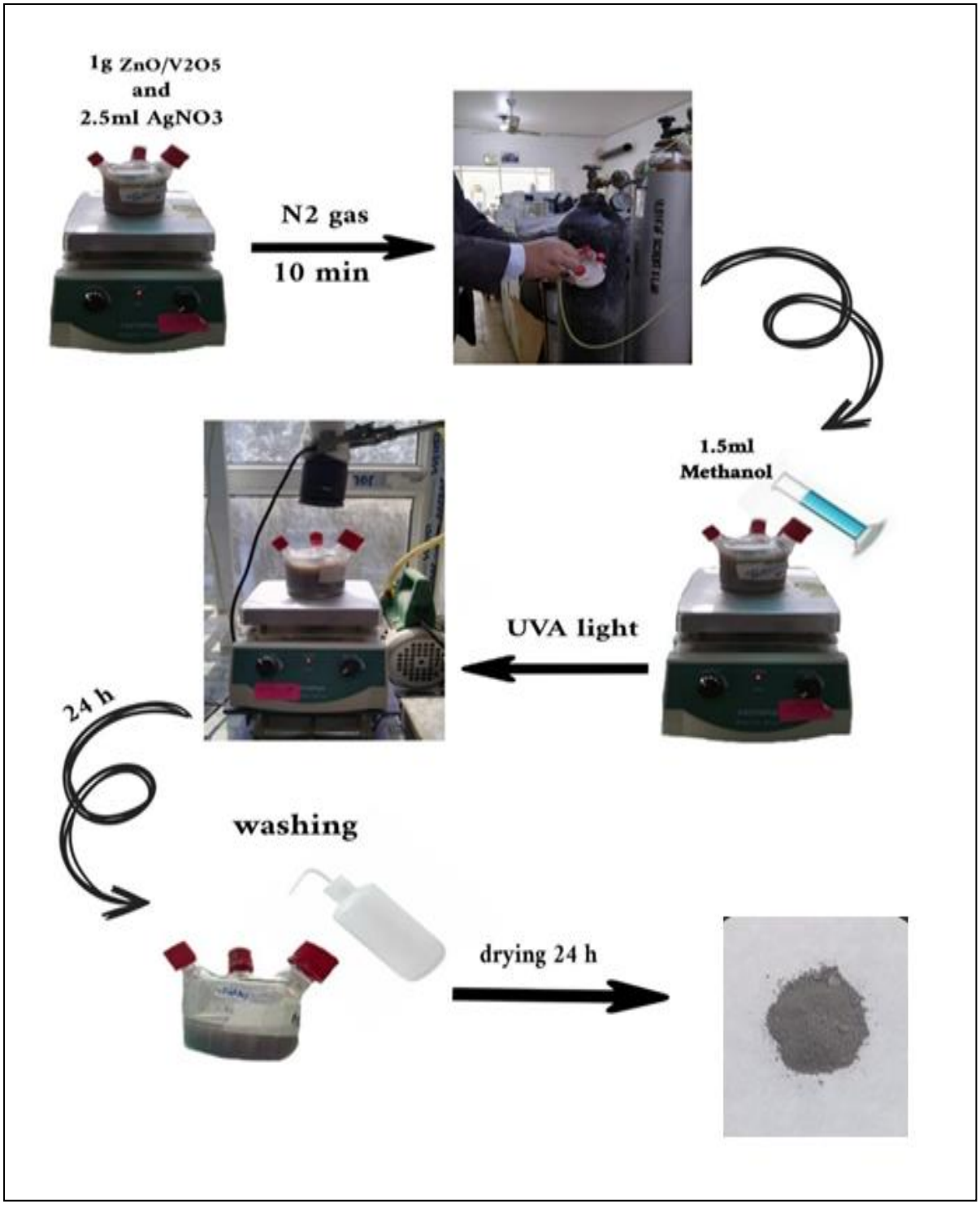

Fig. (3.6): Diagram of preparation of $Ag/V_2O_5/ZnO$ NPs.

3.6 Photocatalytic Degradation of GRL Dye by Using $Ag/V_2O_5/ZnO$ NPs.

3.6.1 Maxilon Blue (GRL) Dye

A maxilon blue dye (GRL) is a very well-known cationic dye that has a molecular formula ($C_{20}H_{26}N_4O_6S_2$), and molecular weight (482.52) g/mol, the dye is odourless blue crystals powder used for various purposes. A stock solution (1000) mg L^{-1} was prepared by dissolving 1.0 g of dye in (1000) mL distilled water.

3.6.2 Calculation of Optimum Wavelengths (λ_{max}) and Calibration Curves of Maxilon Blue (GRL) Dye

To determine a maximum wavelength of the GRL dye, the Ultraviolet-Visible absorption spectra of dyes solution 100 ppm was recorded within wavelengths of (200-800) nm [121].

where the maximum wavelength of the dye solution was determined from its highest absorption in the UV-Vis spectrum found at the wavelength λ_{max}GRL= 590 nm as shown in Fig. (3.7)**.**

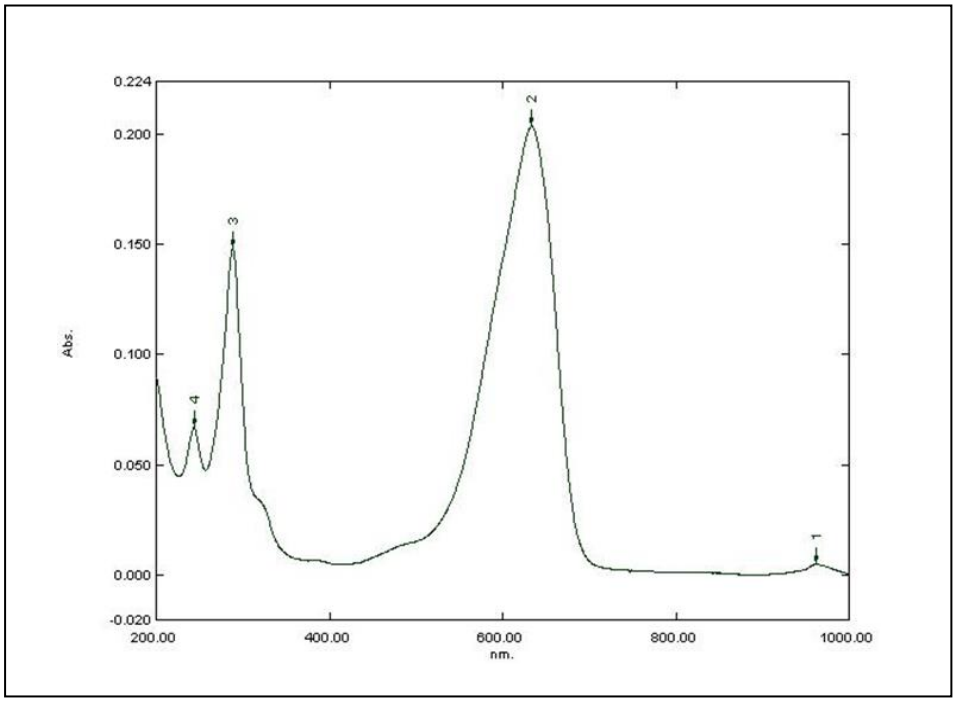

Fig. (3.7): UV-visible absorption spectrum for (GRL) dye.

3.7 Photocatalytic Degradation Experiments

Stock solutions of GRL (1g, 1000 mL) were prepared, and a series of required concentrations were carried out via dilutions by DW. The photocatalytic degradation experiments were carried out in a batch-type reactor with (V_2O_5/ZnO and Ag/V_2O_5/ZnO) nanoparticles suspended in solutions containing the dye to be degraded by using LED/UVA 365 nm Thorlab /USA [122], as shown in Fig. (3.8).

The effect of concentrations solution on the dye absorption composite was studied, the tested concentrations of dye were (5, 10, 15, 20 and 25) ppm in (200 mL DW), at amount of 0.4 g and intensity of light is 2 mW/cm^2 .

The effect of amount solution on the dye absorption composite was studied, the tested amounts of nanoparticles were (0.1, 0.2, 0.4 and 0.6) g in (200 mL solution max B dye) at a concentration of dye 5 ppm and intensity of light is 2 mW/cm^2 for 1 hr.

The effect of intensity of light on absorption composite was studied, the tested intensity of light were (0.8, 2 and 2.6) mW/cm^2 at a concentration of dye of 5 ppm and amount of 0.4 g for a period one hour.

All the experiments were done at room temperature 30°C. The reaction mixture was kept in a top irradiated reactor (capacity of 200 ml) positioned at suitable distance from the light source. The reactor contained a stirring rod supported by a magnetic stirrer to confirm homogeneity of the mixture throughout the reactor. For every single experiment, 200 ml of a requisite concentration of dye aqueous solution was added to a given amount of nanoparticles. The solution was stirred by a magnetic stirrer for 10 min in a dark chamber to reach adsorption/desorption equilibrium.

The reaction mixture was then photolysis for 60 min. Aliquots 10 ml were removed from the sample and centrifuged at 3500 rpm [123].

The change in concentration of the dye solution in the clear solution was measured spectrophotometric ally using a UV 1650 spectrometer, Shimadzu, and monitoring the variation of absorption at 590 nm. General description for the photocatalytic is shown in Fig.(3.8).

The percentage removal of photocatalytic degradation of GRL dye are calculated using the following relationship [124]:

$$PDE(\%) = 100 \times (C_0 - C_t)/C_0 \quad (3.1)$$

where, C_0 and C_t are the initial and concentration (ppm), respectively, PDE photocatalytic degradation efficiency.

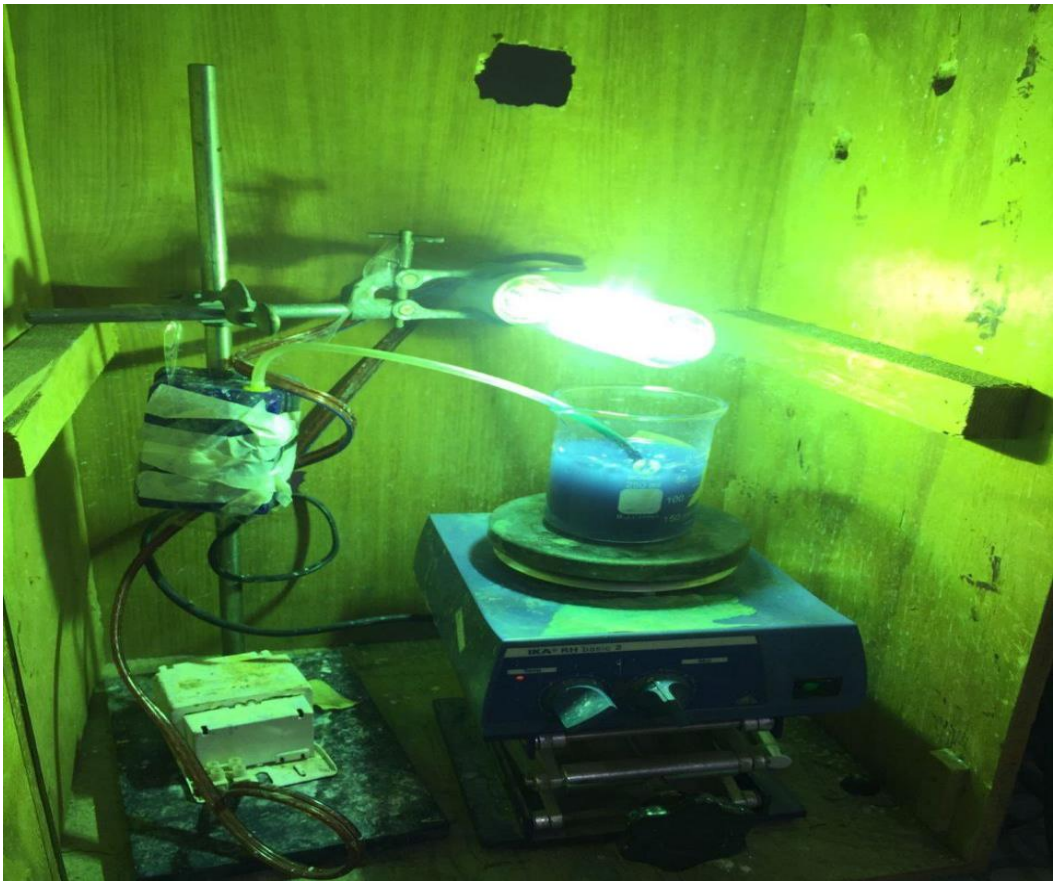

Fig. (3.8): Image for the experimental photo reaction.

3.8 Removal of Pollutants (Dyes) Using $Ag/V_2O_5/ZnO$ NPs

A laboratory sample composed of (100) mL of dye pollutants containing (Brilliant Green (BG), Congo Red (CR), Methyl Violet (MV), Crystal Violet (CV), Methylene Blue (MB), Brilliant blue (BB), Direct Yellow (DY) and Reactive Blue (RB) with a riffled concentration, is used in this study. The laboratory sample is supplemented with 200 ml of distilled water.

Add 0.4 g from $Ag/V_2O_5/ZnO$ nanoparticles to photo-reaction vessel, and expose them to a UV-visible lamp for 2 hrs at 365 nm using a UV-visible spectrophotometer (1650 spectrophotometer, Japan). The supernatant is separated by centrifuge at 3500 rpm for 10 minutes, measure the remaining concentration by using UV-visible spectrophotometer (1650 spectrophotometer, Japan) at 365 nm.

3.9 Characterizations

The prepared sample must be subjected to a range of characterization techniques in order to investigate its unique properties. The crystal structure, surface morphology, and particle size can be precisely determined using the characterization methods listed below. The results of which reveal details on the various optical and structural characteristics of the produced sample.

3.9.1 X-rays Diffraction (XRD)

The production of materials with specified morphologies has drawn a lot of attention for scientists in the recent years since the characteristics of nano- and micro-structures are highly reliant on their forms and sizes. Results from X-ray, diffraction patterns are typically used to investigate the structural properties of such materials [125].

The evaluation of crystallite sizes in the nanoscale range necessitates precise analytical abilities, and the most common method for estimating crystallite size in nanomaterials and one that has been extensively employed in the current work is X-ray diffraction analysis.

The growth of the crystallite refinement and internal strain are responsible for the Bragg peaks' enlargement. Size broadening and stain broadening are determined by analyzing the full width at half maximum (FWHM) of the Brag peaks as a function of the diffraction angle. By measuring the broadening of the X-ray diffraction (XRD) peaks, crystallite size of the deposits was determined.

The crystallite size was calculated using the Scherer Eq. (2.3) and the measurements of X-ray diffraction were made using the PANalytical-AERIS device, (Northlands, Alkhora Company, Baghdad), shown in Fig. (3.9) at the wavelength 0.15406 nm.

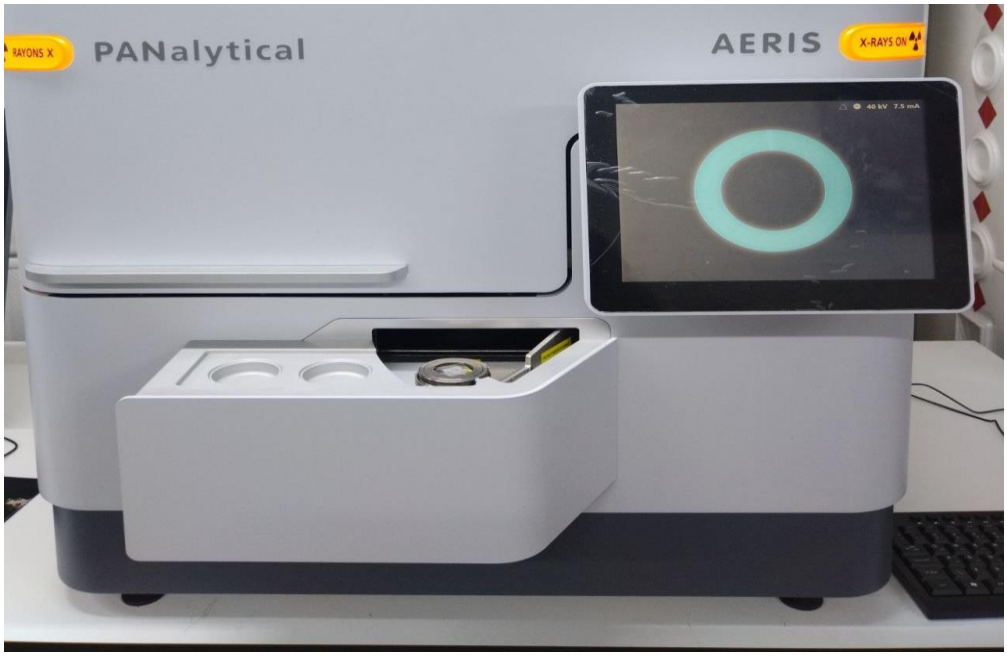

Fig. (3.9): PANalytical of XRD device.

3.9.2 Field Emission Scanning Electron Microscopy(FE-SEM)

The dynamical processes of interactions between nanoparticles and cells are better understood because to the FE-SEM ultra-high resolution.

The prepared nanomaterials were measured by Inspect f 50, (Fei, Northlands, Alkhora Company, Baghdad). This device is shown in Fig. (3.10).

Fig. (3.10): Inspect f 50 of FE-SEM microscope.

3.9.3 Energy Dispersive X-Ray (EDX) Measurement

The prepared nanomaterials were measured by Hitachi S-3000N, (Thermoscientific-Axia, Northlands, Alkhora Company, Baghdad). This device is shown in Fig. (3.11). The required phase has presented, according to the EDX.

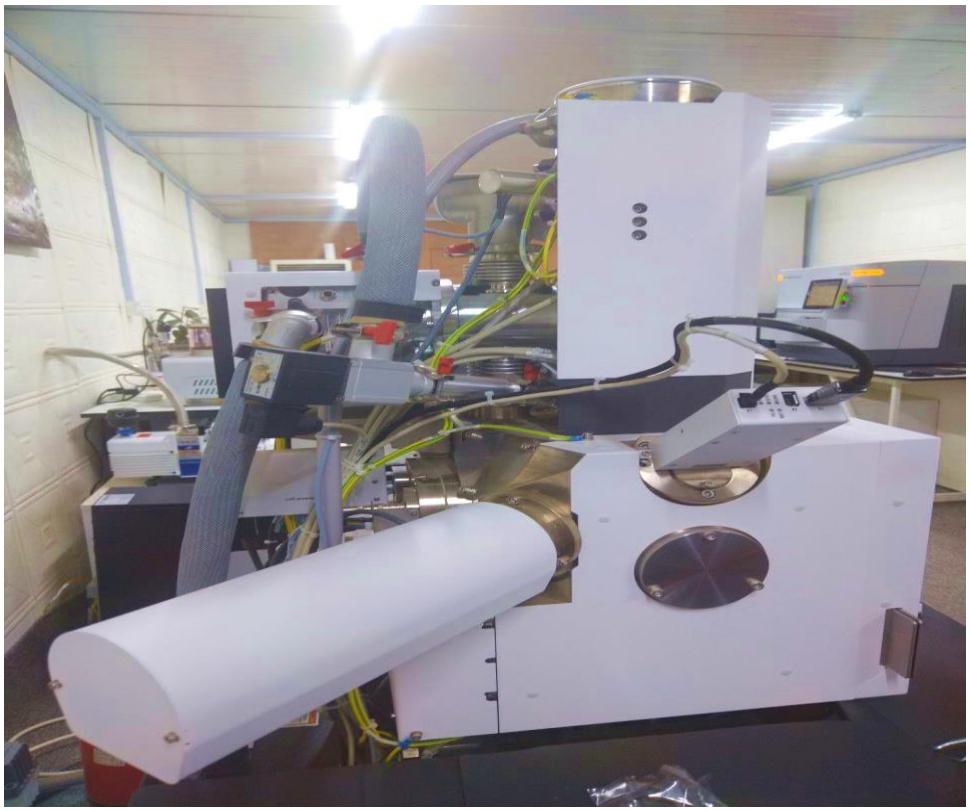

Fig. (3.11): Hitachi S-3000N of EDX device.

3.9.4 Transmission Electron Microscopy (TEM) Measurement

Transmission Electron Microscopy provides information about the structural morphology, crystalline structure, and elemental composition of materials [126].

The prepared $Ag/V_2O_5/ZnO$ NPs were measured by TEM device, (University of Tehran, Iran), and the device is shown in Fig. (3.12).

Fig. (3.12): TEM measurements device.

3.10 BET Surface Area Analyzer

The prepared nanomaterials were measured by BET device, (University of Tehran, Iran) as shown in Fig. (3.13). The BET equation is expressed by [127].

$$\frac{1}{v[(P_\circ/P)-1]} = \frac{c-1}{v_m c}\left(\frac{P}{P_\circ}\right) + \frac{1}{v_m c} \tag{3.2}$$

where P and $P_\circ$ are the equilibrium and the saturation pressure of adsorbates at the temperature of adsorption, v is the adsorbed gas quantity (for example, in volume units), and v_m is the monolayer adsorbed gas quantity, c is the BET constant, with the value is expressed by,

$$c = \exp\left(\frac{E_1 - E_L}{RT}\right) \tag{3.3}$$

where E_1 is the heat of adsorption for the first layer, and E_L is that for the second and higher layers and is equal to the heat of liquefaction.

Equation (3.2) is an adsorption isotherm and can be plotted as a straight line with $\frac{1}{v[(P_\circ/P)-1]}$ on the y-axis and $\varphi = \frac{P}{P_\circ}$ on the x-axis according to experimental results.

This plot is called a BET plot. The linear relationship of this equation is maintained only in the range of $0.05 < \varphi < 0.35$.

The value of the slope A and the y-intercept I of the line are used to calculate the monolayer adsorbed gas quantity v_m and the BET constant c.

Fig. (3.13): BET measurements device.

3.11 Fourier Transform Infrared (FTIR) Measurement

To identify less common materials, IR will need to be combined with nuclear magnetic resonance, mass spectrometry, emission spectroscopy, X-ray diffraction, and other techniques.

Shimadzuo 2400S FTIR, (University of Babylon/ College of science for women) as shown in Fig. (3.14) was used to probe the molecular vibrations of molecules for ZnO, V_2O_5/ZnO and Ag/V_2O_5/ZnO samples which are prepared using the hydrothermal method in sections (3.3), (3.4) and (3.5).

Fig. (3.14): Shimadzuo 2400S FTIR device.

3.12 Band Gap Energy Measurement

A Varian Cary 100 Scan UV−visible spectrophotometer system equipped with a lab sphere diffuse reflectance accessory was used to obtain the reflectance spectra shown in Fig. (3.15).

Lab sphere USRS-99−010, (University of Babylon / College of science for women) was employed as a reflectance standard, the band gap was obtained for ZnO, V_2O_5/ZnO and Ag/V_2O_5/ZnO NPs.

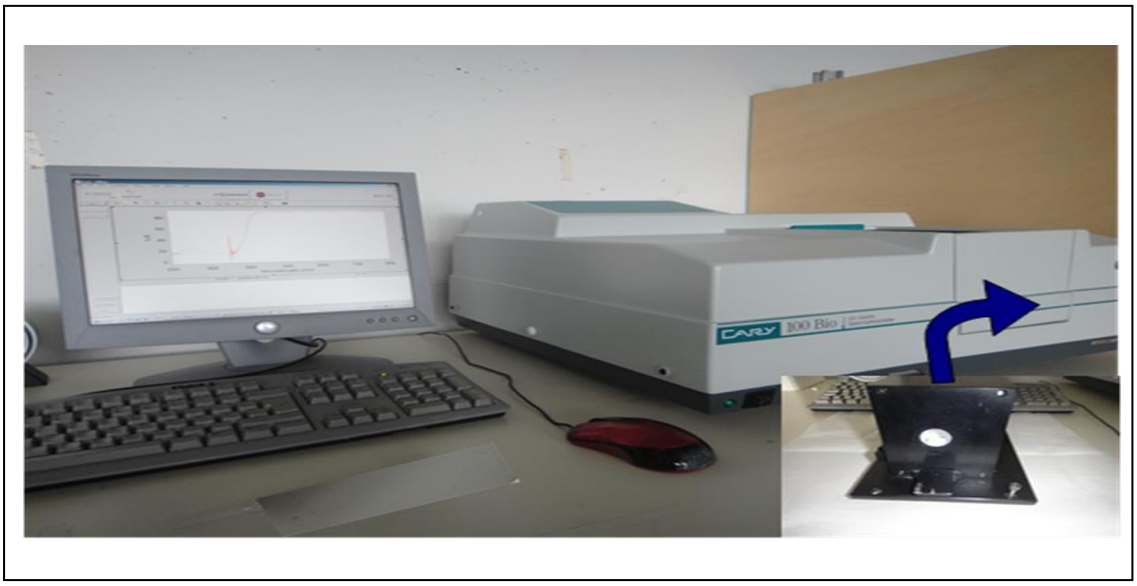

Fig. (3.15): Lab sphere USRS-99−010 for band gap energy measurements device.

Chapter Four

(Results and Discussions)

Chapter Four

Results and Discussions

4.1 Introduction

In this chapter, the characterizations of the prepared samples are determined by different parametric tests, such as (XRD, FE-SEM, EDX, TEM, BET, FTIR and UV-Vis Spectrum). In regard to the spectroscopic studies for ZnO, V_2O_5/ZnO and Ag/V_2O_5/ZnO, which synthesized by hydrothermal techniques, the results of the spectroscopic study include the effect of different amounts of the above-mentioned materials and the effect of different concentrations of GRL dye as well as the effect of light intensity on photocatalysis. It, also, includes optical properties of the photocatalyst.

4.2 XRD Analysis of Prepared Samples

The crystal structure, orientation and phase purity of pure ZnO, V_2O_5/ZnO and Ag/V_2O_5/ZnO NPs were analyses by using X-ray diffraction, as shown in Fig. (4.1).

For the pure ZnO, the characteristic peaks (series of diffraction patterns) 2θ= 31.71386°, 34.36364°, 35.02984°, 36.14111°, 47.47509°, 56.5558°, 62.81067°, 66.32414°, and 67.90023° correspond to the (100), (002), (101), (102), (110), (103), (200), (112), and (201) planes of the hexagonal structure of wurtzite ZnO, respectively, with preferred orientation along (101) plane which represents the peak position max 2θ=35.02984°.

For V_2O_5/ZnO, the XRD pattern is found to be similar to that of pure wurtzite ZnO.

The orientation along (100) plane, that represents $2\theta = 31.43444^{\circ}$, is more than for pure ZnO , with preferred orientation along (101) plane which represents the peak position max $2\theta = 35.92505^{\circ}$.

For the doped material Ag /V_2O_5/ZnO, the XRD pattern is found to be similar to that of pure wurtzite ZnO structure, the orientation along 100 plane, that represents $2\theta = 31.57347^{\circ}$, is larger than for pure ZnO, with preferred orientation along (101) plane which represents the peak position max $2\theta = 36.05891^{\circ}$.

It is known that if the vanadium pentoxide is incorporated into the ZnO crystal lattice, the position of 101 peak slightly shifts into higher angle when compared to the peak position in the pure ZnO due to the radius mismatch of the vanadium ion 0.093 nm and zinc ion 0.088 nm [128].

In addition, the position of 101 peak in the Ag/V_2O_5/ZnO , it slightly shifts to higher angle when compared to the peak position in the pure ZnO which indicates that the lattice expanded after doping and dopants form substitutional defects in the lattice because of the difference among the ionic radius. The ionic radius of silver is 0.144 nm [129].

It is observed that the XRD peaks have not saturated, which indicates that the formation of V_2O_5/ZnO in the composite, zinc oxide and vanadium pentoxide exhibited hexagonal wurtzite and orthorhombic structures, respectively.

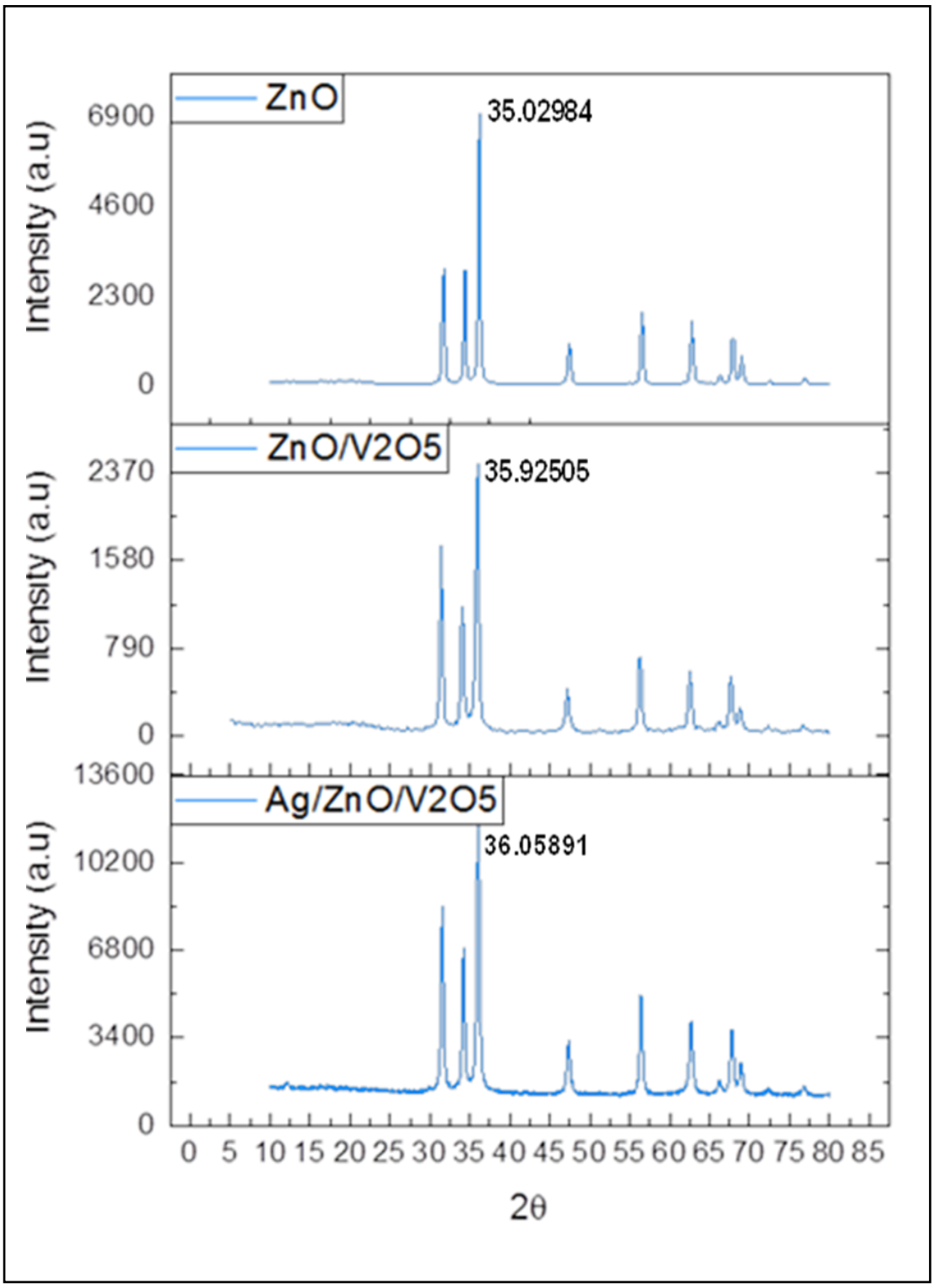

Fig. (4.1): XRD diffractogram of ZnO, V_2O_5/ZnO and Ag/V_2O_5/ZnO NPs.

4.3 Calculation of the Average Crystallite Size

From the X-Ray diffraction patterns of the prepared nanoparticles as shown in Fig. (4.1). The average granular size was calculated to three prepared nanocomposite from the full width at half maximum (FWHM) of the diffraction peaks using Debye-Scherrer Eq. (2.3).

The peak position(2θ), FWHM(β) and values of the mean particles size (crystal size) of the prepared samples were calculated and listed in Tables (4.1), (4.2) and (4.3).

We noticed that the crystallite size of the nanocomposite prepared by the hydrothermal technique V_2O_5/ZnO 13.07 nm is less than that of pure zinc oxide ZnO 19.29 nm prepared by the same technique, where as the crystallite size of the nanocomposite Ag/V_2O_5/ZnO 12.71 nm prepared by photodeposition method doped with silver nitrate was decreases more, which indicates an increase in the surface area of this prepared composite and the success of the preparation method [130].

Table (4.1): XRD data of ZnO results.

Peak Position(2θ)	FWHM(β)	Crystallite Size(nm)
31.71386	0.32661	23.38877732
34.36364	0.27402	27.68701744
35.02984	4.16464	1.818411731
36.14111	0.49203	15.34357196
47.47509	0.41268	17.61500934
56.5558	0.37452	18.67321914
62.81067	0.3875	17.49116923
66.32414	0.41064	16.18884121
67.90023	0.42355	15.55285765
69.04082	0.36475	17.93816072
72.50157	0.15803	40.52439129

Table (4.2): XRD data of V_2O_5/ZnO results .

Peak Position(2θ)	FWHM(β)	Crystallite Size(nm)
31.43444	0.38531	19.83928976
34.08412	0.43747	17.35546701
35.92505	0.43241	17.46982891
47.22227	0.48967	14.85979775
56.30188	0.43642	16.04374971
62.57341	0.53599	12.66139546
67.67932	0.50191	13.14169926
68.81858	0.62163	10.5394844
66.23812	1.01028	6.583367684
68.81858	100.32781	0.065302529
76.72226	0.40872	15.23489803

Table (4.3): XRD data of Ag/V_2O_5/ZnO results.

Peak Position(2θ)	FWHM(β)	Crystallite Size(nm)
31.57347	0.39361	19.41429625
34.2224	0.41795	18.15930652
36.05891	0.43863	17.21556378
47.36387	0.50368	14.43865407
56.43803	0.45252	15.46308853
62.70395	0.57107	11.87538998
66.27012	0.69127	9.619732942
67.80875	0.54108	12.18110302
68.93058	0.61539	10.63922142
76.85072	79.76526	0.07799484
76.85072	0.5776	10.77091191

4.4 Field Emission Scanning Electron Microscopy (FE-SEM)

The information regarding the morphology of ZnO compound is obtained by FE-SEM analysis. Fig. (4.2) a and b shows the FE-SEM image of as-synthesized ZnO and confirms the rods-like microstructures of ZnO.

Also, at some places, some small rods can be easily seen in Fig. (4.2) a and seem to be agglomerated. The magnified image in Fig. (4.2) c and d, indicates that these rods have a hollow hexagonal cross-section in its average diameter of about 47.68 nm.

It can be also seen that the morphology of the ZnO nanoparticles takes rod-like shape and obviously demonstrate aggregation of the particles. The aggregation of particles (formation of larger particles) should have been originated from the large specific surface area and high surface energy of ZnO nanoparticles.

Thus, due to the large specific surface area and high surface energy, ZnO nanoparticles aggregate severely [131]. FE-SEM analyses V_2O_5/ZnO composite prepared by hydrothermal method as illustrated in Fig. (4.2) c and d.

The micrographs reveal with particle like morphological appearance and spherical shape with homogeneous size distribution, the average diameter of nanoparticles is 35 nm.

The high-magnification FE-SEM images show that the V_2O_5/ZnO particles have a porous nature with typical pore sizes below 100 nm.

Due to the attraction between the V_2O_5 and ZnO particles, the surface morphologies are more compact and continuous with the presence of closely packed particles [132].

Hence, it may not affect the mobility of electrons travelling between the grains V_2O_5/ZnO nanoparticles that were generated. All shown via this figure is proof that the material formed was on the nanoscale.

The nanoparticles are dispersed over a wide region, and the average size of the particle corresponds to the number of nanomaterials acquired by XRD.

As shown in Fig. (4.2) e and f, FE-SEM image for Ag/V_2O_5/ZnO describes the creation of a closely stacked cluster comprising rod-like aggregated particles of diameters of nonuniform sizes.

The synthesized Ag/ V_2O_5/ZnO nanocatalyst was rod-like cylinder with a homogeneous size diameter 28.12 nm. This rod-like shape can be attributed to the type of synthesis method and precursor employed [133]. The photocatalyst with a rod-like shape has been reported to be very effective in organic dye degradation [134].

Field emission scanning electron microscopy images of nanoparticles with Ag content are shown very smooth surfaces as is observed in Fig. (4.2) e and f. As low amounts of silver are incorporated in the NPs, the surface becomes nanostructured as is clearly observed in Fig. (4.2) e.

Field emission scanning electron microscopy images of Ag/V_2O_5/ZnO demonstrates that the shape of the ZnO changes from a rod shape to a smaller agglomeration shape when silver nitrate is added during the reaction.

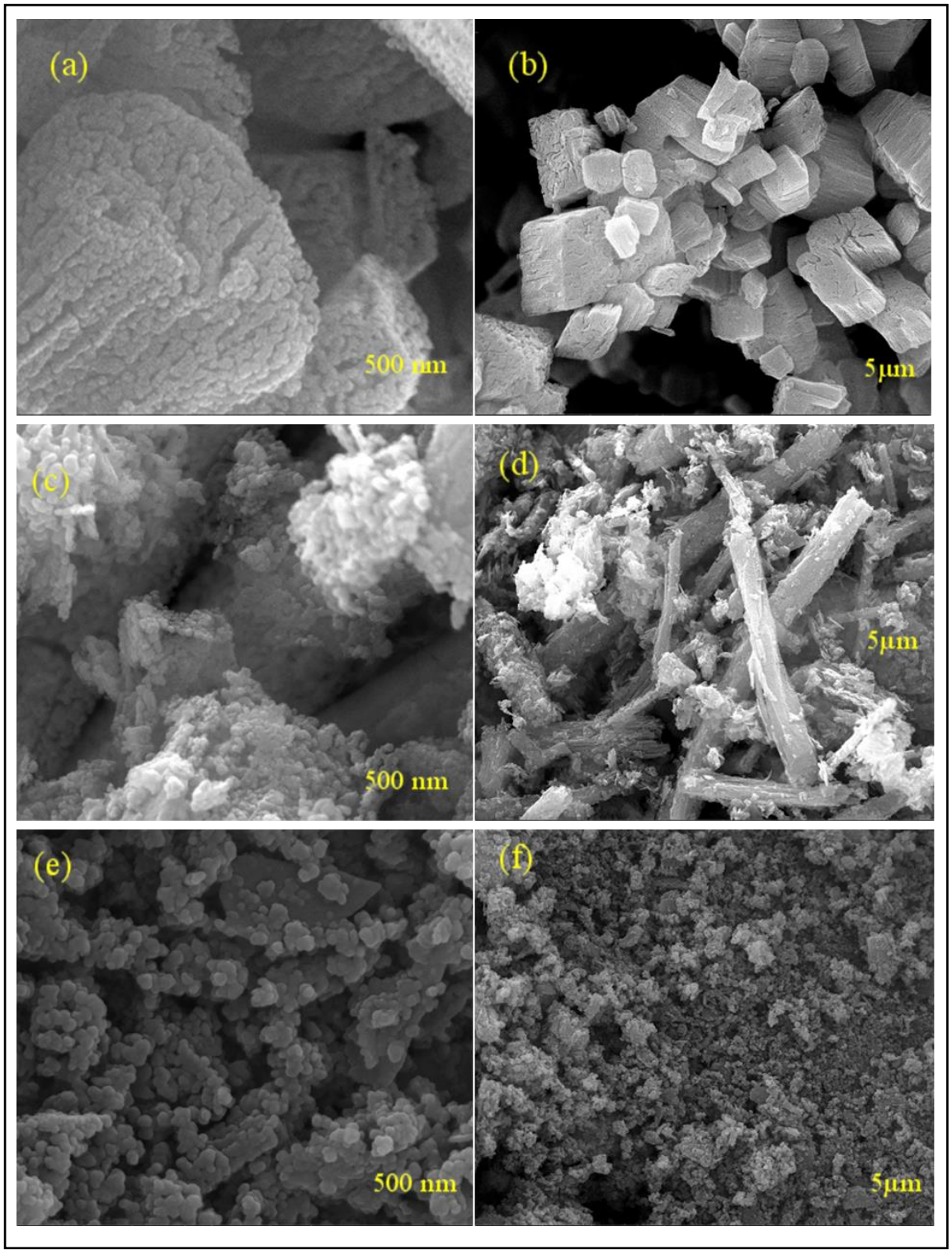

Fig. (4.2): FE-SEM images of nanoparticles (a) and (b) ZnO, (c) and (d) V_2O_5/ZnO, (e) and (f) Ag/V_2O_5/ZnO

4.5 Energy Dispersion X-Ray (EDX) Analysis

Due to the resolution limit of the FE-SEM technique and the small sizes of nanoparticles, it's not easy to find nanoparticles on the surface of ZnO tubes from FE-SEM images.

Therefore, to demonstrate the presence of nanoparticles. This result confirmed that the ZnO powder contained Zn , O and C elements and that ZnO successfully formed as shown in the Fig. (4.3), the reason for the presence of the carbon element is due to the process of burning the nanomaterial in an oven at 500°C . Table (4.4) provides the weight % of the compositional elements like C, O and Zn that are present in ZnO nanoparticles.

The elemental analysis of V_2O_5/ZnO confirms the presence of V in the product Fig. (4.4) and Table (4.5). These results clearly show that V_2O_5 is successfully doped the ZnO nanoparticles. This is in agreement with the results of XRD patterns. The EDX analysis confirms the presence of C, O, V, and Zn in the Ag/V_2O_5/ZnO composite.

The Ag/V_2O_5/ZnO composite is further characterized by EDX, shown in Fig. (4.5). The EDX results specify that Ag/V_2O_5/ZnO is made up of only four elements C, O, V, and Zn, weight/ atomic percentage is shown in Table (4.6). The weight ratios of C, O, V, and Zn are 11.2 %, 7.0 %, 0.5% and 81.3 %, respectively and the atomic ratios of C, O, V, and Zn are 35.5 %, 16.7 %, 0.4 % and 47.4 %, respectively.

Ag concentration is very low according to the other elements. This is evidence of that the amount of the Ag atoms did not enter the ZnO nanostructure. This situation compatible with XRD results.

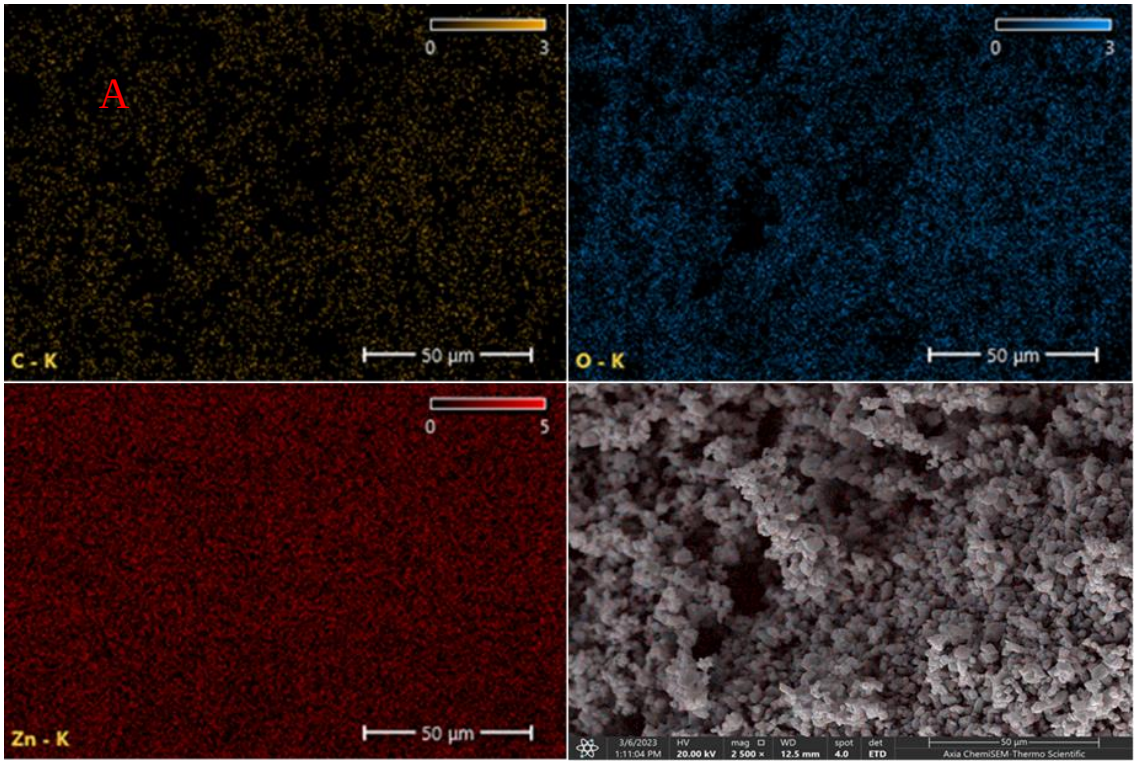

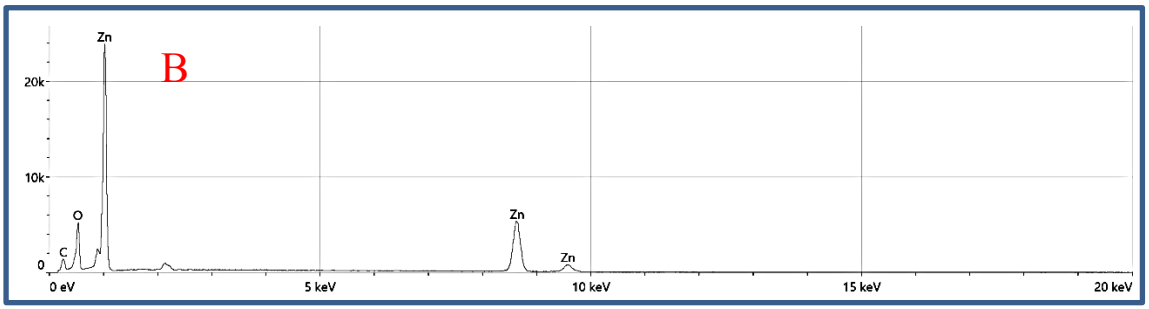

Fig. (4.3): (A) EDX analysis of ZnO nanoparticles images (B) blots

Table (4.4): EDX analysis results of ZnO nanoparticles.

Element	Atomic %	Atomic % Error	Weight %	Weight % Error
C	26.1	0.4	9.0	0.1
O	33.4	0.3	15.3	0.1
Zn	40.5	0.3	75.7	0.5

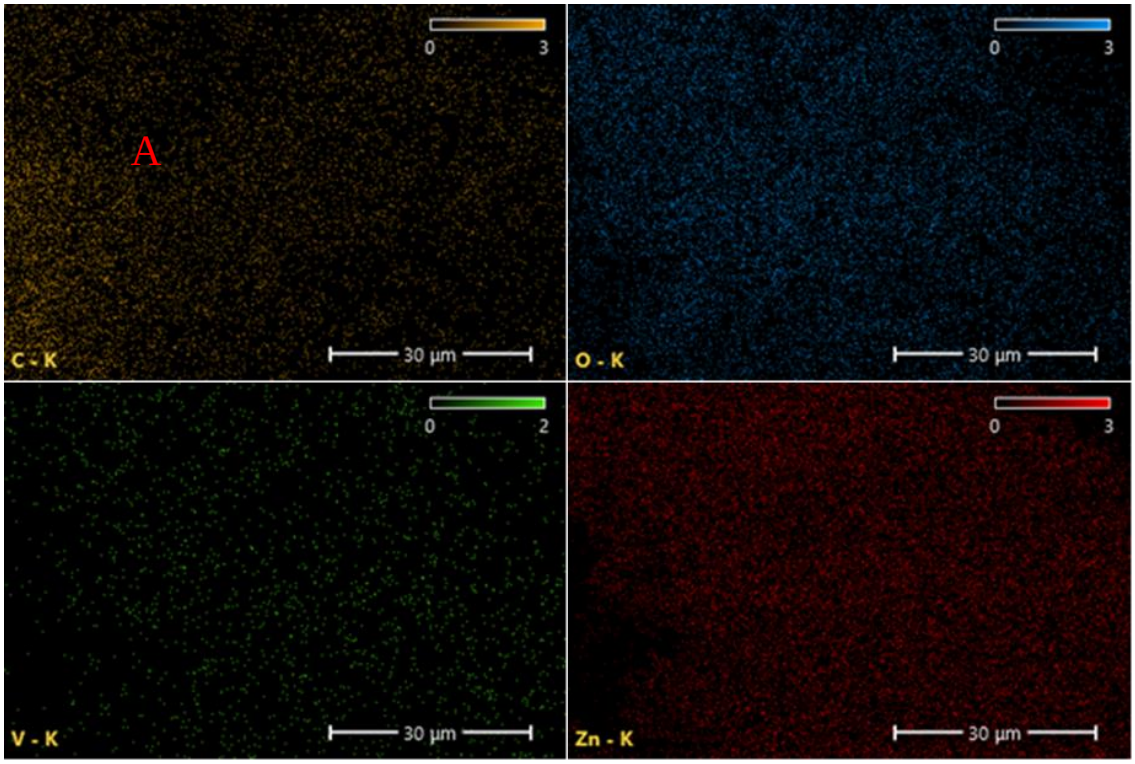

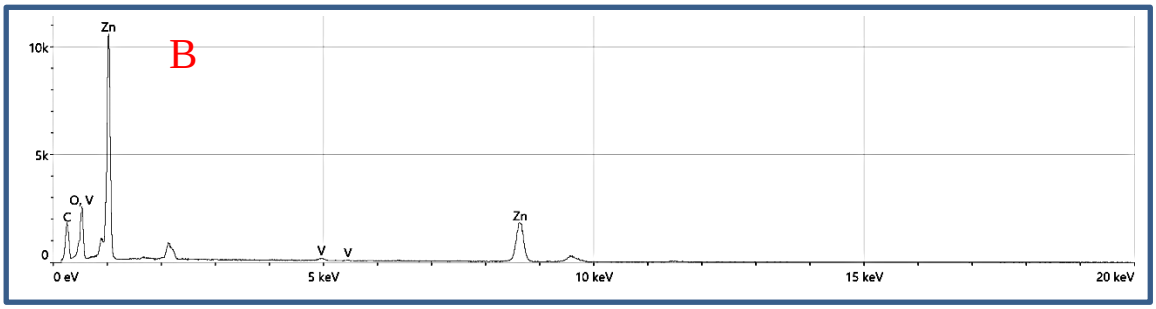

Fig. (4.4): (A) EDX analysis of V_2O_5/ZnO nanoparticles images (B) blots.

Table (4.5): EDX analysis results of V_2O_5/ZnO nanoparticles.

Element	Atomic %	Atomic % Error	Weight %	Weight % Error
C	51.8	0.7	24.8	0.3
O	25.5	1.9	16.2	1.2
V	0.5	0.0	1.0	0.1
Zn	22.2	0.3	58.0	0.7

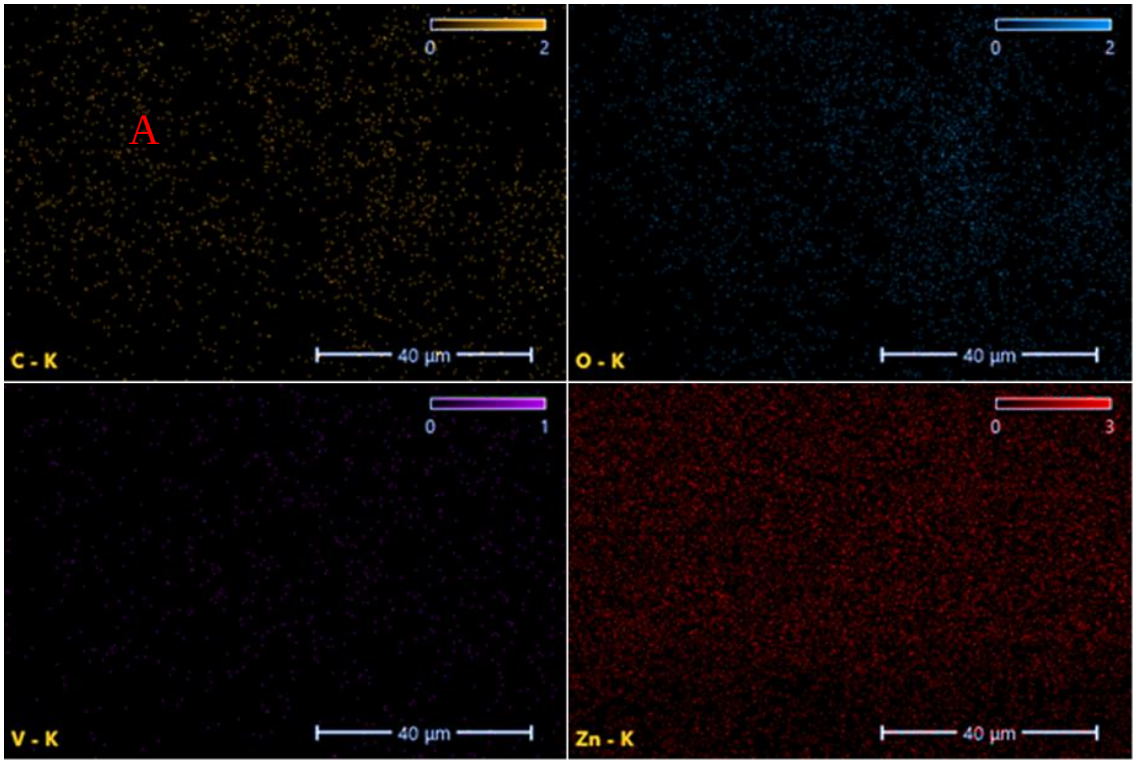

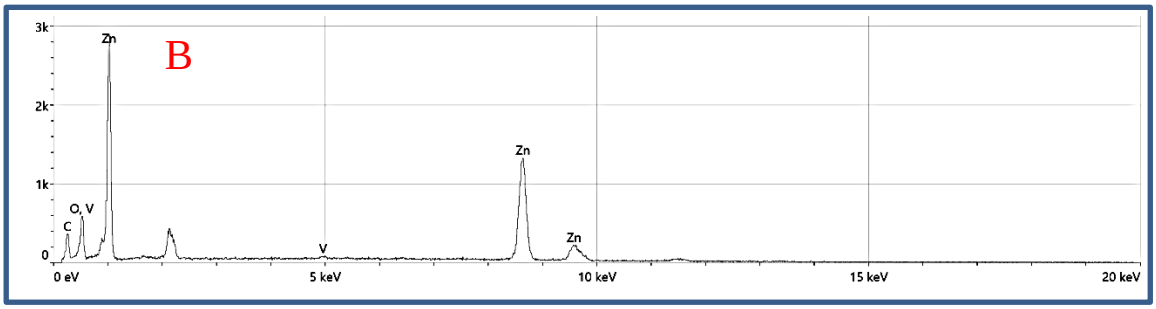

Fig. (4.5):(A) EDX analysis of $Ag/V_2O_5/ZnO$ nanoparticles images(B) blots .

Table (4.6): EDX analysis results of $Ag/V_2O_5/ZnO$ nanoparticles.

Element	Atomic %	Atomic % Error	Weight %	Weight % Error
C	35.5	1.0	11.2	0.3
O	16.7	1.0	7.0	0.4
V	0.4	0.1	0.5	0.1
Zn	47.4	0.7	81.3	1.1

4.6 Transmission Electron Microscopy (TEM)

To characterise the specific surface area of nanostructured particles, a method based on analysing transmission electron microscopy (TEM) images is used, and takes into account structural parameters of nanostructured particles including the number distribution of primary particles.

The approach proposed in this work was applied to one nanostructured powder laboratory prepared ($Ag/V_2O_5/ZnO$). This first involved prior analysis by the BET method, The procedure to calculate the specific surface area using image analysis was then applied to the sampled.

The experimental results obtained on the nanostructured powder cover a range of diameters varying from 60 to 200 nm [135]. It is identified from the image that the zinc oxide NPs are randomly distributed. It has been estimated that the diameter and the length of the nanoparticles are about 60, 100 and 200 nm, respectively.

Transmission Electron Microscopy images reveal that the V_2O_5 compound are overlap with the ZnO compound.

Furthermore, the V_2O_5 nanoparticles and ZnO nanoparticles overlap with each other and with Ag form a three-dimensional network structure on $Ag/V_2O_5/ZnO$ nanocomposite, which provides a fast conducting electrons path.

It leads to a better charge transportation in the photocatalytic process [136]. The random distribution of ZnO nanoparticles on V_2O_5 is shown in Fig. (4.6).

There are two factors that influence the size and shape of ZnO materials synthesized: (i) the nature of the agent added during ZnO formation and (ii) the prepare method, spherical nanoparticles formed by coalescence of photodeposition were observed, very small spherical nanoparticles were obtained, spherical nanoparticles with narrow size distribution were observed.

Finally, agglomerates were obtained by coalescence of spherical nanoparticles [137]. The grainy contrast in Fig. (4.6) confirms the nanocrystalline structure of the material, specifically, it reveals the area in the nanocrystalline agglomerate consisting of the grains with similar orientations.

These grains give a noticeable bright contrast. These nanoparticles are an ideal sample to investigate the internal structure of by TEM and relate it to the structure of initial V_2O_5 crystals.

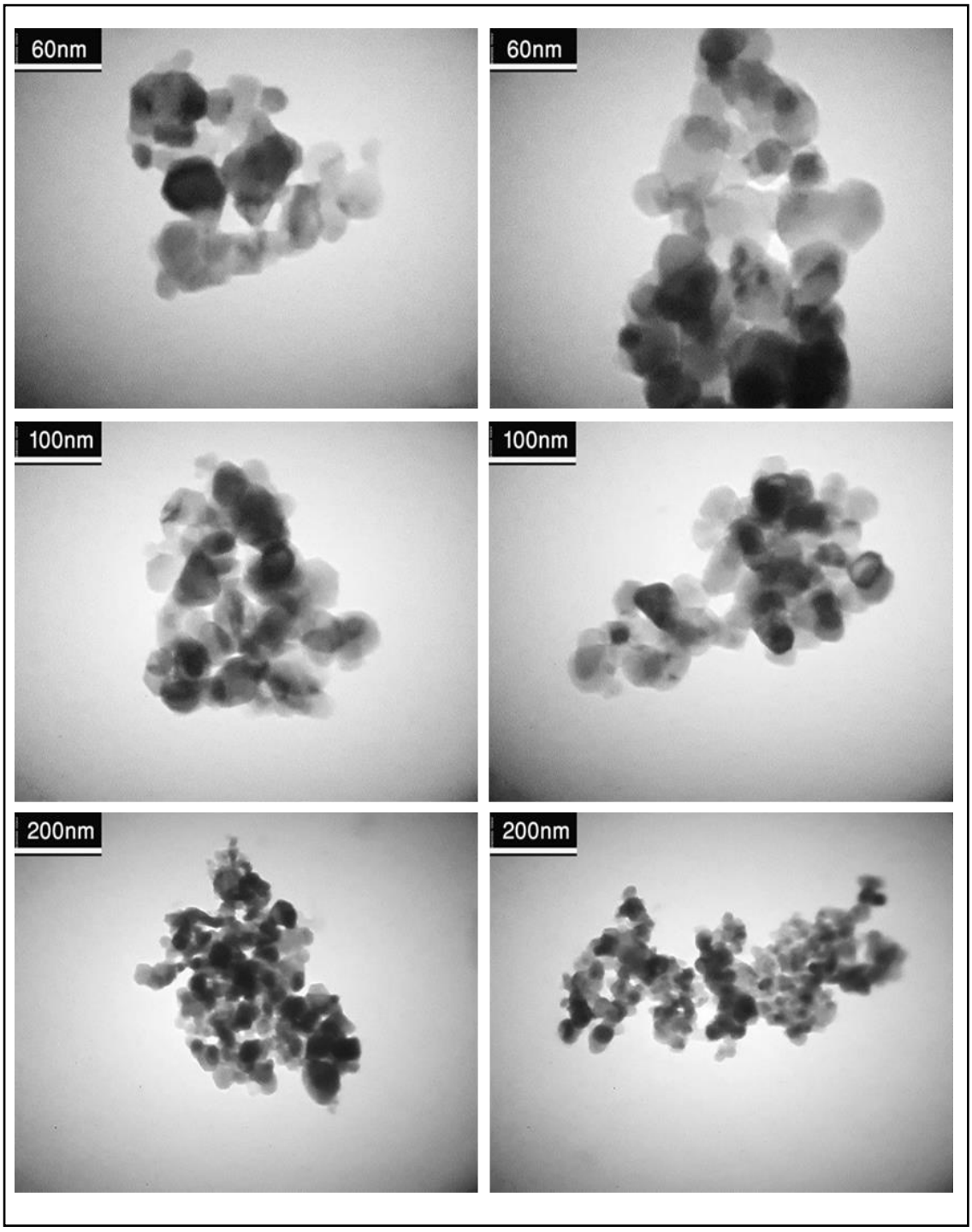

Fig. (4.6): TEM analysis of Ag/V_2O_5/ZnO NPs.

4.7 Surface Area Analysis BET

At the present time, only the measurement of specific surface area by the BET method constitutes a reference in the domain of materials and more recently in toxicology [138,139].

However, the low mass concentrations of nanoparticles usually (in the order of 0.1 mg/m^3 or less) are incompatible with the BET analysis [140]. The corresponding isotherms and multi-point fit plots of ZnO, V_2O_5/ZnO and Ag/V_2O_5/ZnO are shown in Table (4.7).

The multi-point plot reveals that the ZnO, V_2O_5/ZnO and Ag/V_2O_5/ZnO samples have a surface area of 10.476, 15.569 and 24.933 $m^2\ g^{-1}$, respectively.

As observed from the BET measurement, the ZnO has very low surface area. However, the surface area increases after the incorporation of V_2O_5 in ZnO and Ag in V_2O_5/ZnO.

The cumulative pore volumes of ZnO, V_2O_5/ZnO and Ag/V_2O_5/ZnO are 0.1379, 0.2310 and 0.2457 $cm^3\ g^{-1}$, respectively. The calculated BET parameters of the samples are given in Table (4.7) .

The pore size distribution of ZnO is shown in Table (4.7). It is dominated mostly by pores in the range of 52.647 nm, but some biggest pores are also present of V_2O_5/ZnO is 59.345 nm.

Also, the pores decreases when the nanomaterials are inoculated with silver nitrate by the photo deposition process and show in the range of 39.424 nm .

The measured BET surface area of the sample ZnO was smaller than V_2O_5/ZnO and surface area of the sample V_2O_5/ZnO was smaller than Ag/ V_2O_5/ZnO which can be correlated to the fact that the method of preparation helped to form a nanocomposite distinguished by its physical and chemical properties.

A consequence of the particle surface area variation, which is caused by the particle size difference. Fig. (4.7), (4.8) and (4.9) shows the positive correlation between surface area nanoparticles, such positive correlations strongly indicate that the increased photocatalytic activity should be ascribed to the smaller size of ZnO and V_2O_5 particles, which gives a higher surface area of the catalyst Ag/V_2O_5/ZnO.

Table (4.7): BET analysis results of ZnO, V_2O_5/ZnO and Ag/V_2O_5/ZnO NPs.

Nanoparticles	V_m $cm^3(STP)g^{-1}$	$a_{s,BET}$ $m^2\ g^{-1}$	C	Total pore volume(p/p_0= 0.981) [$cm^3\ g^{-1}$]	Average pore diameter[nm]
ZnO	2.407	10.476	509.28	0.1379	52.647
V_2O_5/ZnO	3.577	15.569	103.18	0.231	59.345
Ag/V_2O_5/ZnO	5.7284	24.933	———	0.2456	39.424

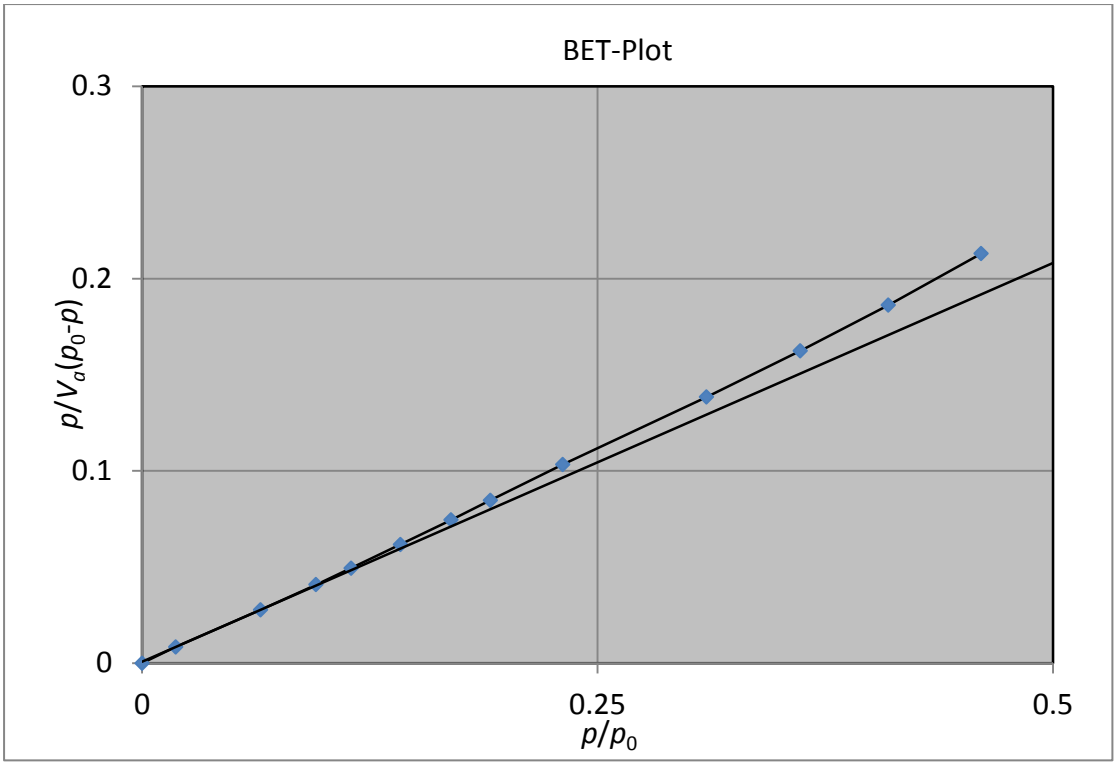

Fig. (4.7): BET analysis of ZnO.

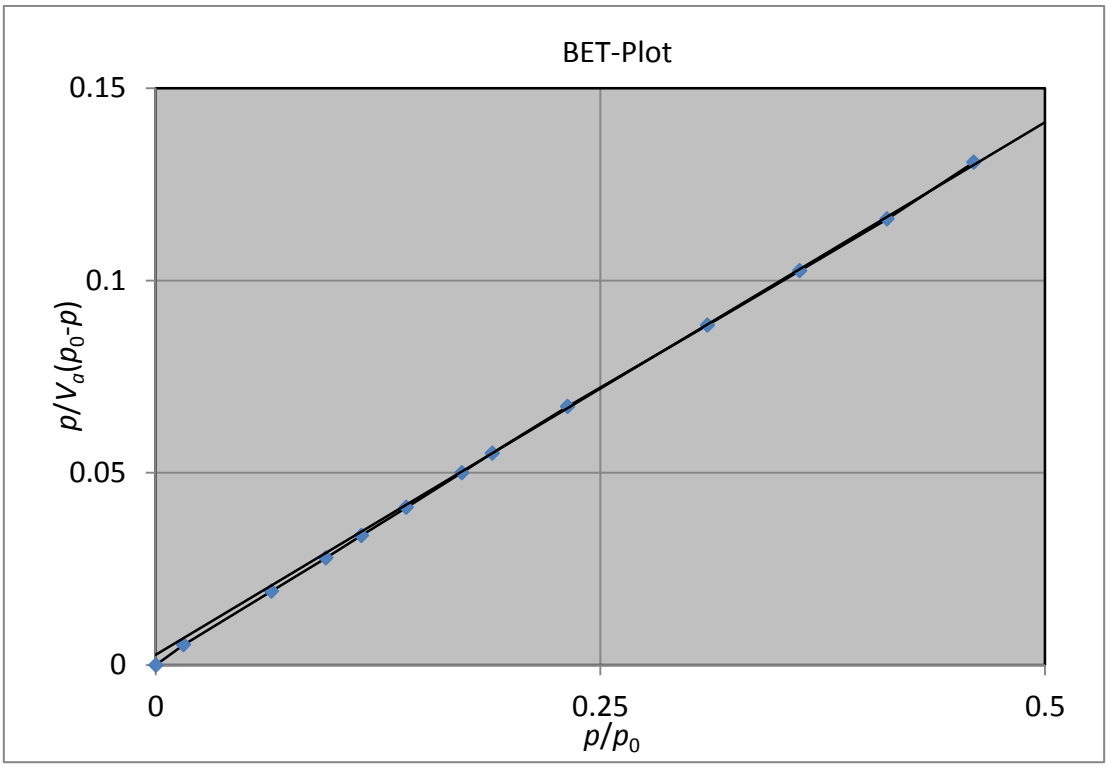

Fig. (4.8): BET analysis of V_2O_5/ZnO NPs.

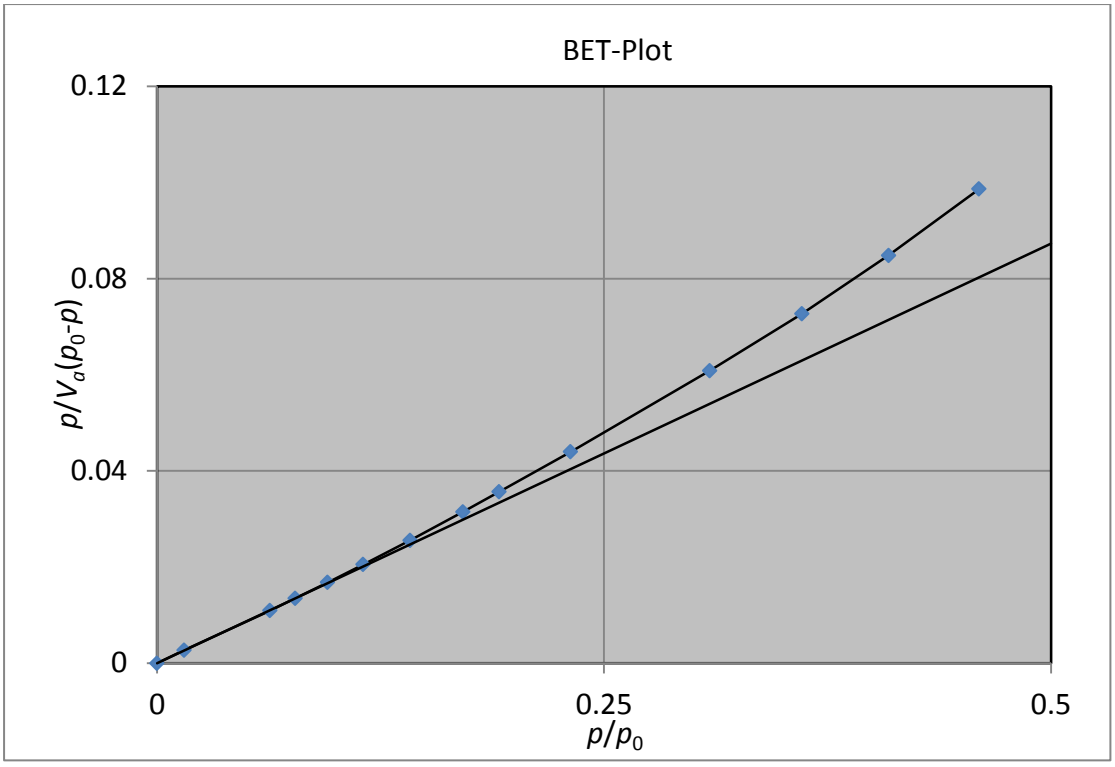

Fig. (4.9): BET analysis of $Ag/V_2O_5/ZnO$ NPs.

4.8 Fourier Transform Infrared (FTIR)

Fourier Transform Infrared technique was used to analyze the surface functional groups responsible for the absorption of GRL dye for nanoscale surfaces ($Ag/V_2O_5/ZnO$), V_2O_5/ZnO, ZnO, as in Fig. (4.10).

The samples were made in the form of nanoparticles, then the infrared spectra were measured on a spectrophotometer. Infrared light was recorded in the wavenumber range (4000-500) cm^{-1} with an intensity is 100 (a.u). Fig. (4.10) shows the infrared spectrum of the three composites and experience a broad peak at (3000-2500) cm^{-1} in the spectrum of the nanocomposite. The peaks indicate the set of functional properties present in the nanoparticles of zinc oxide.

It is concluded that the samples have absorption peaks in the range of 3000 cm^{-1}, 2900 cm^{-1}, 2350 cm^{-1}, 775 cm^{-1}, 700 cm^{-1}, 575 cm^{-1}, and the bending of the spectrum is observed at 1600 cm^{-1}.

The absorption peak at 575 cm^{-1} corresponds to the oxygen vibration mode metallic (ZnO stretching vibrations).

The V_2O_5/ZnO spectrum consists of the same peaks of the ZnO compound and it is observed that they are broader and more stretched (asymmetric stretching mode of V-O -V), 775 cm^{-1}, 700 cm^{-1} and 575cm^{-1} (stretching mode homologue of V- O), 3000 $cm^{-1}$and 2900 cm^{-1}.

The peak at 3000 cm^{-1} (vibration of VO) gives information about the structural quality of the product. Similarly, the presence of the absorption peak of V-O-V reveals the formation of a V_2O_5 phase. In the case of (Ag /V_2O_5/ZnO) peak intensity decreases due to the formation of Ag nanoparticles on the surface of V_2O_5/ZnO.

A decrease occurs in the peak of the curve at the peak 575 cm^{-1}. The vibration at 537 cm^{-1} can be attributed to the local vibrational mode associated with oxygen vacancies and interfacial zinc elements.

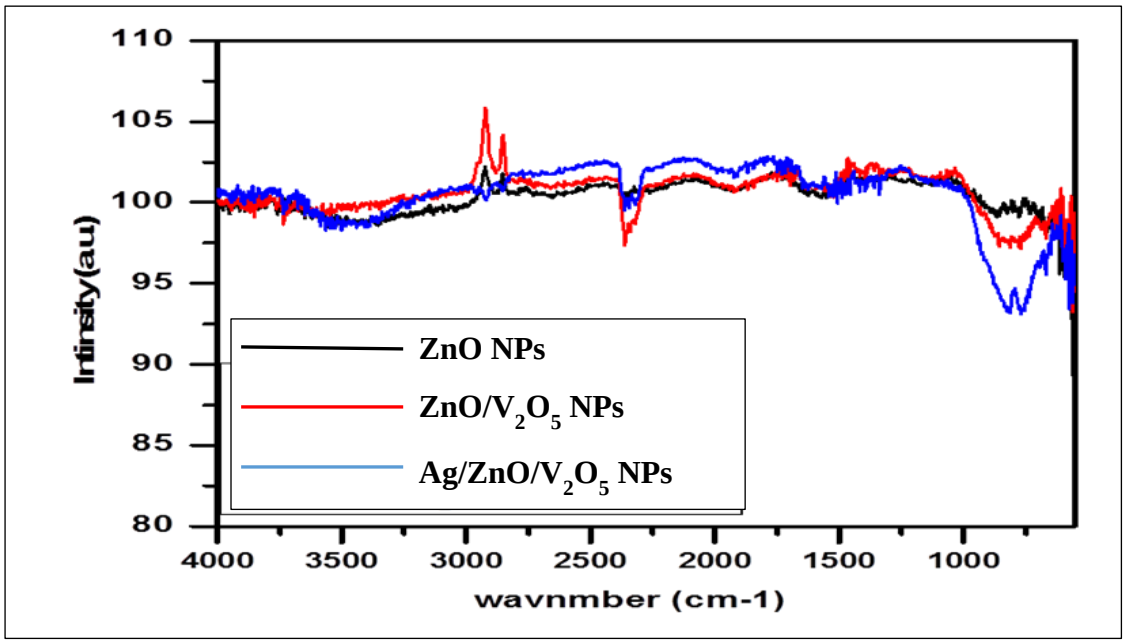

Fig. (4.10): FTIR diffract gram of ZnO, V_2O_5/ZnO and Ag/V_2O_5/ZnO NPs.

4.9 Photocatalytic Activity of V_2O_5/ZnO NPs

Different dye concentrations and different amount of V_2O_5/ZnO nanoparticles were used, and the light intensity was changed. The primary tested concentrations of dye were 5, 10, 15, 20 and 25 ppm (in 200 mL solution GRL dye).

The effect of concentrations solution on the dye absorption via V_2O_5/ZnO composite was studied at amount of 0.4 g and intensity of light is 2 mW/cm^2.

The effect of amount on the dye absorption via V_2O_5/ZnO composite was studied at a concentration of 5 ppm and intensity of light is 2 mW/cm^2.

The effect of intensity on the dye absorption via V_2O_5/ZnO composite was studied at amount of 0.4 g and concentration of 5 ppm.

Experimental tests were performed before photocatalysis and an 1 hr after photocatalysis, all samples were placed in a centrifuge at 3500 r/min for 10 min, the non-sediment material was withdrawn and back into the centrifuge once again and calculate the amount of absorbance.

The absorbance of the solution was measured by using UV-Visible spectrophotometer.

All experiments carried out under temperature 25°C, using Eq. (3.1), the photodegradation efficiency was determined. The results are summarized in the following subsections.

4.9.1 Effect of Mass Dosage

The effect of amounts (0.1, 0.2, 0.4 and 0.6) g of ZnO/ V_2O_5 NPs on the cracking and degradation of (GRL) dye, photocatalytic degradation in the solution GRL dye concentration 5 ppm, reaction at 25°C, time is 1hr.

First, order experimental data to be analyzed as shown in Fig. (4.11). The influence of adsorbent dose on the removal of 5 ppm GRL dye as in Fig. (4.11).

Increasing the amount of V_2O_5/ZnO NPs from 0.1 g to 0.6 g, the photocatalytic efficiency is improved from 48.6% to 60.96% after 1hr. The maximum value of absorption efficiency is 84.08% at 0.2 g.

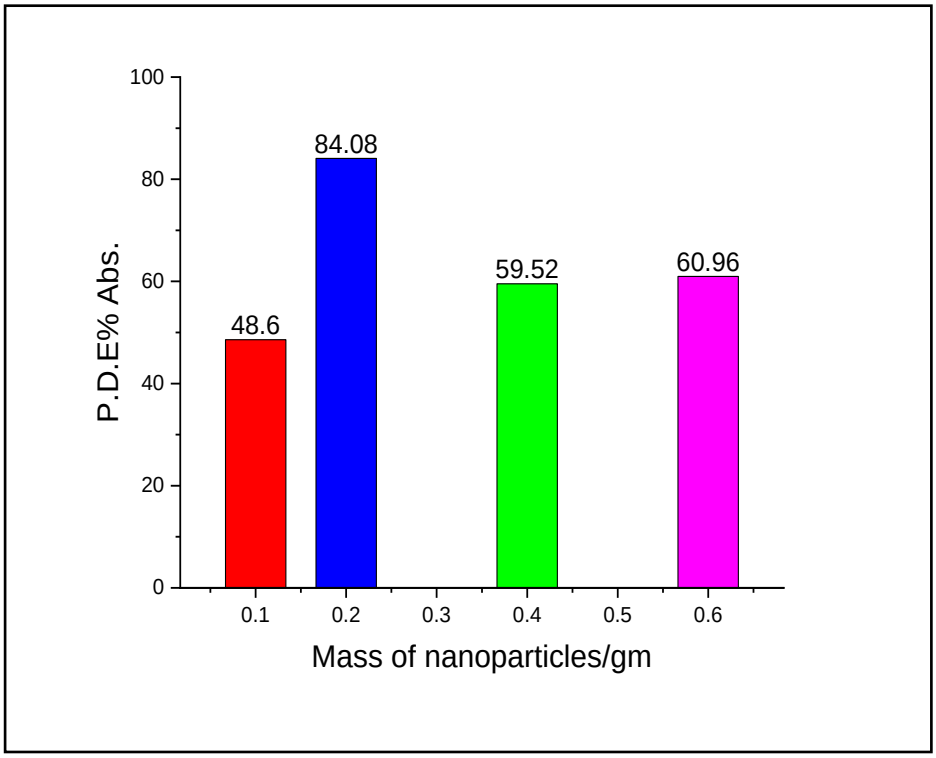

Fig. (4.11): Photocatalytic efficiency at several dosages for V_2O_5/ZnO NPs.

4.9.2 Effect of Concentration of GRL Dye

Several dye concentrations 5, 10, 15, 20 and 25 ppm, were carefully chosen to study the influence of initial GRL dye concentration on to V_2O_5/ZnO NPs. Amount of V_2O_5/ZnO NPs was 0.4 g and intensity of light was 2 mW/cm^2. GRL dye solution plays a pivotal role in estimate rate of degradation, also the time dependence of photocatalytic degradation of GRL under several concentrations.

Fig. (4.12) show the effects of absorbent GRL dye on the mass dosage 0.4 g and the removal percentage improved after 1houre time of absorption.

Increasing of GRL dye concentration from 5 to 25 ppm led to a change in the absorption efficiency from 59.52% to 26.23 %.

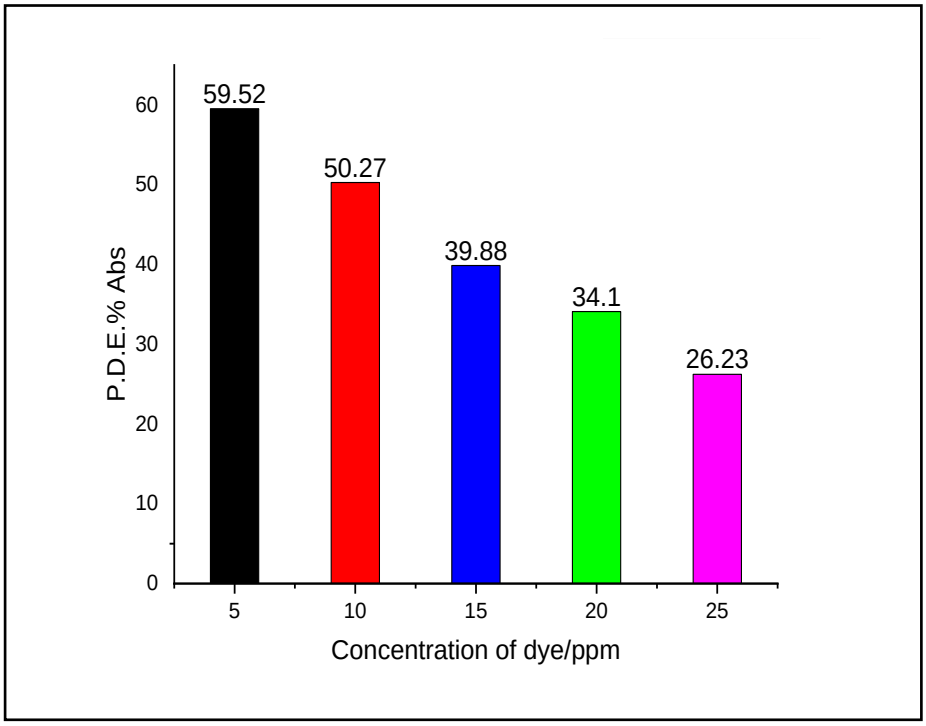

Fig. (4.12): Photocatalytic efficiency at several Concentration of dye for V_2O_5/ZnO NPs.

4.9.3 Effect of Light Intensity

Effect of light intensity (L.I) 0.8, 2 and 2.6 Mw/cm^2, was observed via change the distance among light source and exposed surface of the material. Photo degradation of GRL dye via the influence of L.I was studied at 0.4 g for V_2O_5/ZnO NPs, concentration of GRL dye 5 ppm.

All reactions were discovered to continue following the first-order kinetics depicted in Fig. (4.13). As more radiation is accessible to excite the catalyst and, as a result, more charge carriers are created, the rate of Photocatalytic efficiency and absorbance efficiency (PDE%) increased with increasing U.V intensity light.

The increasing of light intensity, the photocatalytic efficiency is improved from 49.19% to 93.35% after 1hr.

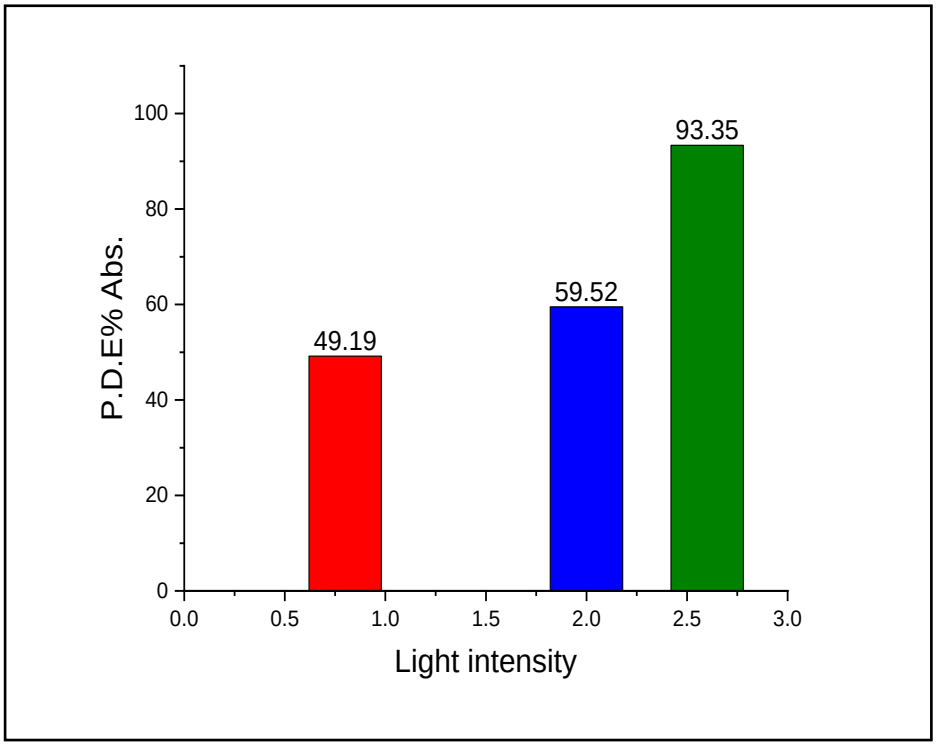

Fig. (4.13): Photocatalytic efficiency at several light intensity for V_2O_5/ZnO NPs.

4.10 Photocatalytic Activity of $Ag/V_2O_5/ZnO$ NPs

Maxilon blue dye stock solutions (1g, 1000 mL^{-1}) are generated, and DW dilutions are used to create the series of needed concentrations. $Ag/V_2O_5/ZnO$ nanoparticles of various amounts and dye concentrations were utilized, and the light intensity is altered. The main dye concentrations that have been evaluated are 5, 10, 15, 20 and 25 ppm (in a solution of 200 mL of GRL dye). At amount of 0.4 g and a light intensity of 2 mW/cm^2, the influence of the solution concentrations on the dye absorption via $Ag/V_2O_5/ZnO$ composite is tested. The effect of intensity on the dye absorption via $Ag/V_2O_5/ZnO$ composite is studied at amount of 0.4 g and concentration of 5 ppm, while the effect of amount on the dye absorption via $Ag/V_2O_5/ZnO$ composite is studied at a concentration of 5 ppm and intensity of light 2 mW/cm^2.

All tests were performed in a photo-reaction vessel, and the beaker was exposed to a UV-visible lamp for an hour at 365 nm using a UV Visible spectrophotometer (1650 spectrophotometer, Japan) before the Photocatalytic process.

The amount of absorbance before and after photocatalysis for one hour was calculated by experimental experiments. Using a UV-Vis spectrophotometer to measure solution absorbance while running a centrifuge at 3500 rpm for 10 minutes. Maximum wavelength 365 nm was determined using a (UV-Visible) spectrophotometer [141].

The temperature used for all trials was 25°C , using Eq. (3.1), the photodegradation efficiency was determined. The results are summarized as follows:

4.10.1 Effect of Mass Dosage

Effect of amounts 0.1, 0.2, 0.4and 0.6 g for $Ag/V_2O_5/ZnO$ NPs on the Photocatalytic degradation of GRL dye, at a reaction temperature of 25°C for a period of one hour. The analysis of first order experimental data is depicted in Fig. (4.14) .

The effect of adsorbent dosage on the removal of 5 ppm GRL dye. After 1hr, the absorption efficiency increased from 60.089% to 66.32% due to the $Ag/V_2O_5/ZnO$ NPs increased amount from 0.1 g to 0.6 g. The maximum value of absorption efficiency was 71.068% at 0.4 g.

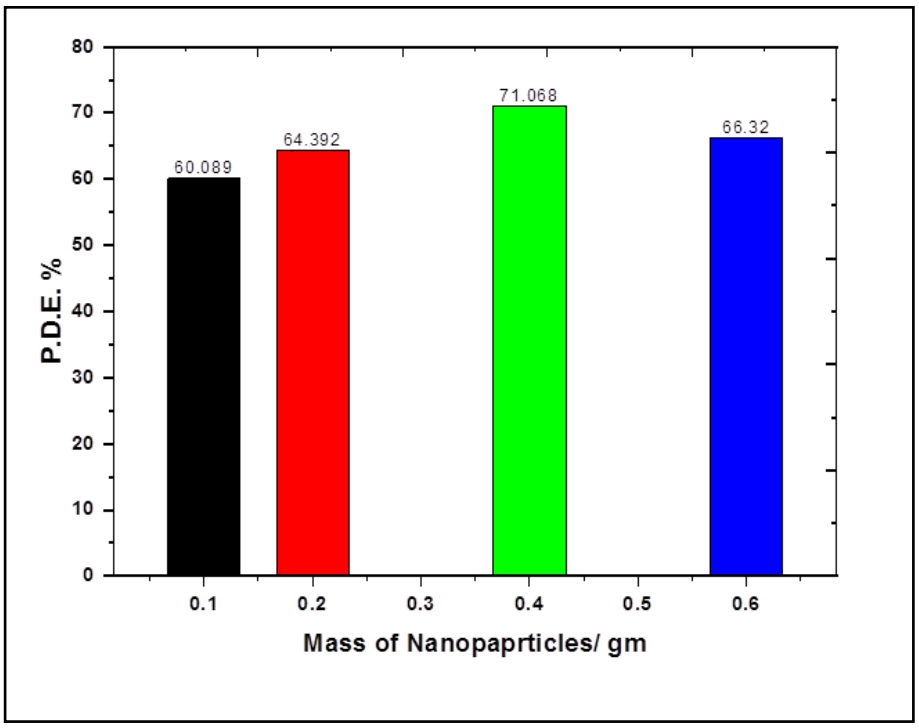

Fig. (4.14): Photocatalytic efficiency at several dosages for $Ag/V_2O_5/ZnO$ NPs.

4.10.2 Effect of Concentration of GRL Dye

For the purpose of examining the impact of GRL dye concentration on $Ag/V_2O_5/ZnO$ NPs, many dye concentrations 2,5,10,15,20 and 25 ppm were carefully selected. The amounts of GRL adsorbed at solution are depicted in Fig. (4.15) at 0.4 g of $Ag/V_2O_5/ZnO$ NPs.

GRL dye solution is essential for estimating the rate of photocatalytic degradation as well as the time dependency of this process at various concentrations. Assuming first order kinetics based on the experimental results, Fig. (4.15) shows first order kinetics. Effects of the GRL dye adsorbent on the mass dosage 0.4 g, as shown in Fig. (4.15).

After 1hr of absorption, the elimination percentage decreased from 91.03% to 16.37% as the GRL dye concentration increased by roughly 2 to 25 ppm.

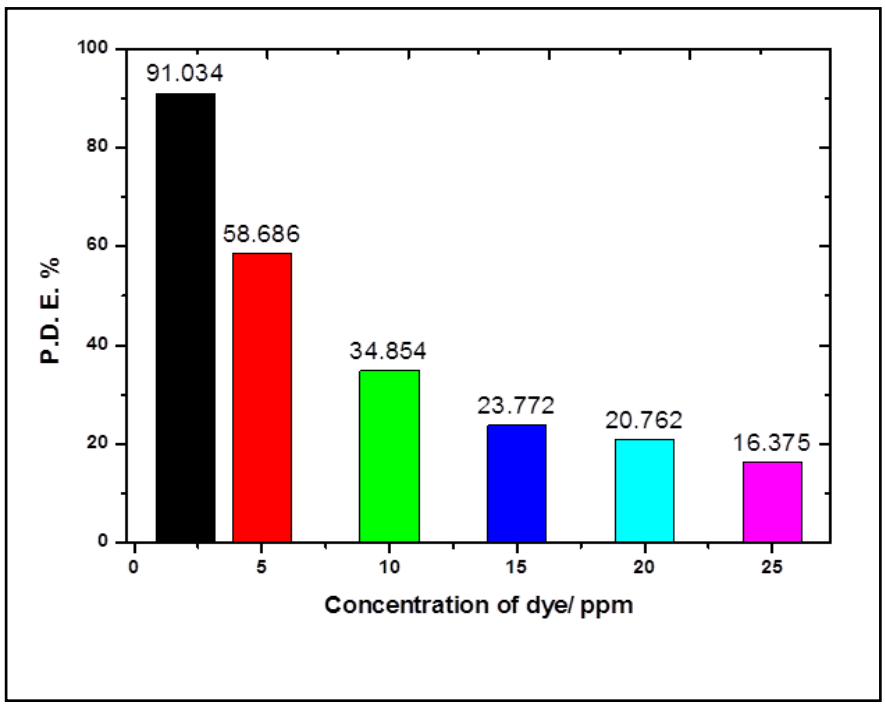

Fig. (4.15): Photocatalytic efficiency at several concentration of dye for $Ag/V_2O_5/ZnO$ NPs.

4.10.3 Effect of Light Intensity

By varying the distance between the light source and the material's exposed surface, the influence of light intensity 0.8, 2, and 2.6 mW/cm^2 was seen. GRL dye photo degradation under the effect of L.I was examined in 0.4 g of Ag/V_2O_5/ZnO NPs with a GRL dye concentration of 10 ppm.

All reactions were found to proceed in accordance with the first-order kinetics shown in Fig. (4.16).

The rate of photocatalytic degradation and PDE% increased with increasing U.V intensity light since more radiation is available to excite the catalyst and, as a result, more charge carriers are produced.

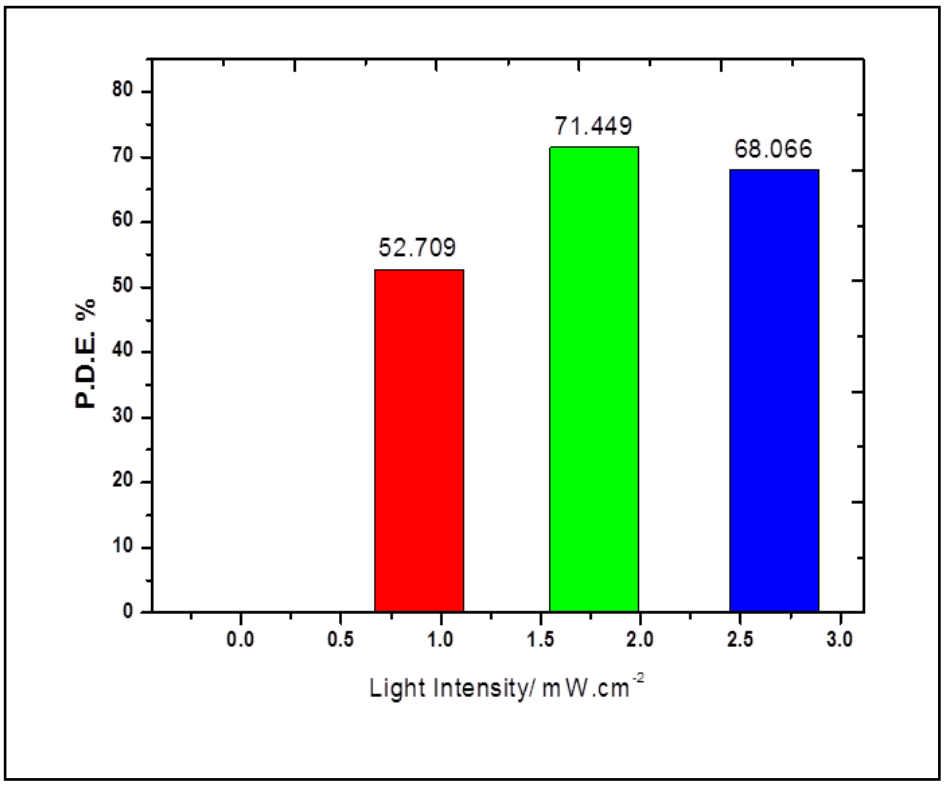

Fig. (4.16): Photocatalytic efficiency at several light intensity for Ag/V_2O_5/ZnO NPs.

4.11 Photocatalytic of $Ag/V_2O_5/ZnO$ in Aqueous Mix Dye.

A laboratory sample of a dye of unknown concentration was used in its aqueous solution 200 ml. An amount of nanocatalyst was chosen and placed in the dye solution, then an adsorption experiment was performed for ten minutes, and then a photocatalytic experiment was performed on it using a visible ultraviolet lamp for 2 hrs.

A sample was withdrawn of the solution before the photocatalytic experiment and a sample was withdrawn after every 15 minutes of this experiment.

The samples were separated by a centrifuge for ten minutes, the clear matter was withdrawn, and the sample separation process was repeated again.

The absorption spectrum was measured with an ultraviolet-visible spectrophotometer, and the results appeared as in Fig. (4.17).

The reason for the emergence of many peaks is due to the selection of a mixture of dyes (more than 7 mixed dyes).

The peaks that located the range (200- 400) nm show the yellow and orange dye, such as rhodamine and eosin, while the peaks located in the range of (500- 600) nm are blue and violet, such as methylene blue and maxilon blue.

The gradient of the top in Fig. (4.17) starts from the dye before the photocatalytic to the adsorption state, then it begins to gradually crack every 15 min, starting from yellow and orange to blue and violet, then the dye disappears after two hours, and this is evidence that proves the effectiveness and activity of the surface of the photocatalyst.

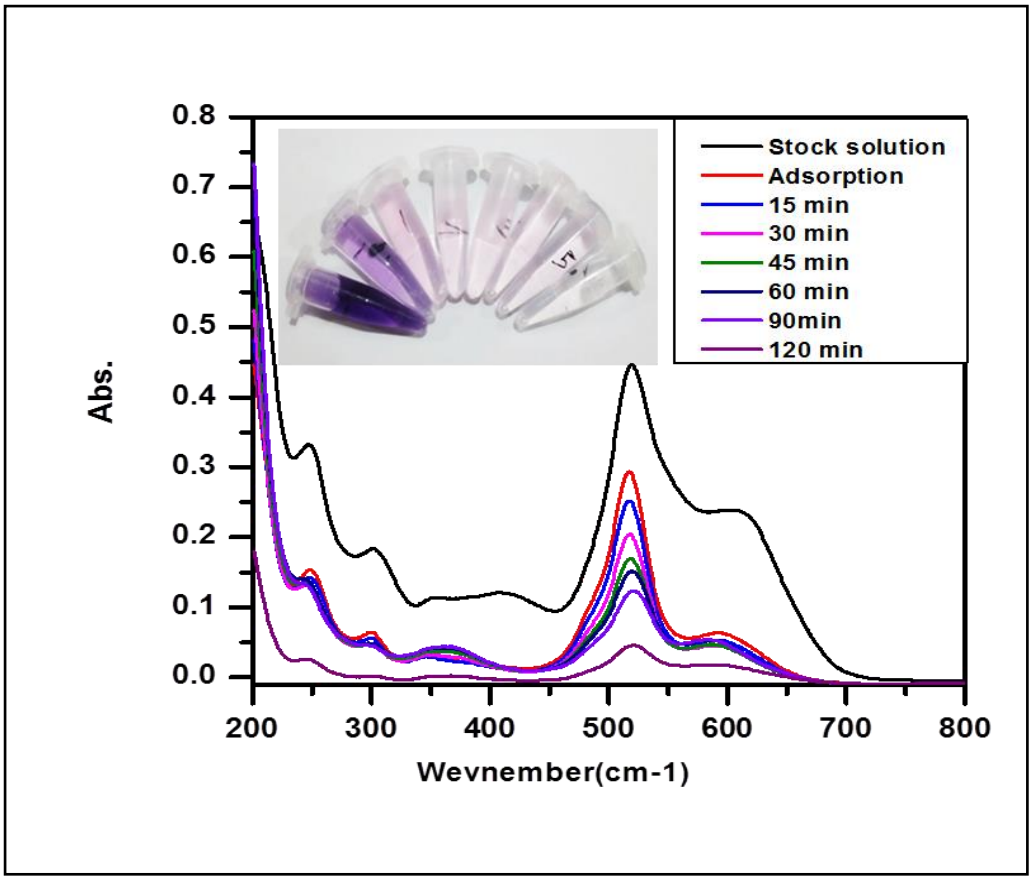

Fig. (4.17): Photocatalytic efficiency of samples aqueous mix of dye for $Ag/V_2O_5/ZnO$ NPs.

4.12 Photocatalytic Comparison of ZnO, ZnO/V_2O_5 and $Ag/V_2O_5/ZnO$ NPs.

The photocatalytic experiment was conducted for the three nanocomposites ZnO, V_2O_5/ZnO and $Ag/V_2O_5/ZnO$ each separately, and the catalytic efficiency was calculated for each nanocomposite. The results of the comparison showed as in the Table (4.8).

It is clear from the table that the catalytic efficiency of ZnO was rather low, but V_2O_5/ZnO shows a better efficiency, which indicates the success of the preparation process for this nanocomposite.

$Ag/V_2O_5/ZnO$ nanocomposite shows higher efficiency absorption, which indicates the success of the photodeposition process for this nanocomposite as shows in Fig. (4.18).

Table (4.8): Comparison of photocatalytic efficiency for ZnO, V_2O_5/ZnO and Ag/V_2O_5/ZnO NPs.

Sequence	nanocomposites	before Photocatalytic	after Photocatalytic	Photocatalytic efficiency
1	ZnO	0.610	0.261	57.21%
2	V_2O_5/ZnO	0.798	0.323	59.52%
3	Ag/V_2O_5/ZnO	0.930	0.470	49.46%

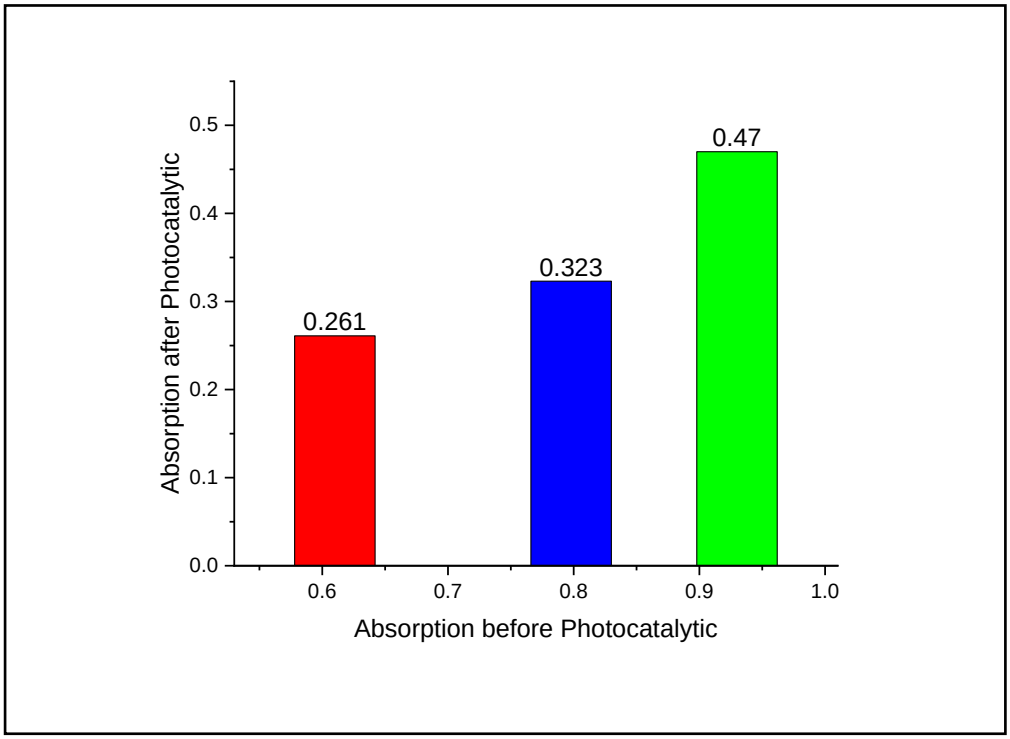

Fig. (4.18): Comparison of photocatalytic efficiency for ZnO, V_2O_5/ZnO and Ag/V_2O_5/ZnO NPs.

4.13 Optical Properties

When studying the spectra of absorbance, transmittance and reflectivity, we can verify the practical benefit that enables us to use the prepared nanomaterial for the applications for which it is intended.

The absorbance of the nanomaterial depends on the energy of the photons falling on the material, on the type of material and the nature of its crystalline structure.

Optical spectrometer (UV-Visible spectrophotometer, single beam (Shimadzu/ Japan) was used, which records absorbance as a function of wavelength within the range (400-800) nm.

We made all measurements of the absorbance, transmittance and reflectivity spectra within the wavelength 590 nm for all the prepared materials [142].

Observing the results shown in Tables (4.9) and (4.10), one can conclude that the absorbance of the two types of prepared V_2O_5/ZnO and Ag/V_2O_5/ZnO materials begin with a gradual decrease with the increase in the concentration of the dye with the constant amount of nanomaterial used and the intensity of the light used.

This decrease is caused by the difficulty of breaking down the dye as its concentration increases.

Using of the nanocomposite in the concentration of 5 ppm achieved the highest absorbance compared with other concentrations, as shown in Fig. (4.19). This corresponds to the lowest recorded transmittance for the same concentration as shown in Fig. (4.20).

That the ratio of reflectivity of the V_2O_5/ZnO compound increases in general with increasing percentages of concentration, except for the ratio 25 ppm, as the percentage of reflectivity decreased. The highest ratio of reflectivity was recorded at a concentration of 20 ppm.

As for Ag/V_2O_5/ZnO composite, the reflectivity begins to increase at concentration 10 ppm and then begins to gradually decrease for other concentrations. This is what seems clear from the spectrum in Fig. (4.21), which represents the change of reflectivity as a function of the change in the concentration of the dye.

The highest value of the absorption coefficient for both Tables was 1.37 cm^{-1} and 1.35 cm^{-1} at the dye concentration 5 ppm, respectively and the highest value of the extinction coefficient for both Tables was $6.43 \times 10^{-6}$and 6.34×10^{-6} at the concentration 5 ppm, respectively.

Table (4.9): Absorbance spectra, transmittance, reflectivity, absorption coefficient, extinction coefficient, and refractive index with the dye concentration change of V_2O_5/ZnO NPs.

Concentration of dye (ppm)	P.D.E% absorbance	P.D.E% transmittance	P.D.E% reflectivity	Absorption coefficient (cm^{-1})	Extinction coefficient ($\times 10^{-6}$)	Refractive index
5	59.52	25.39	15.08	1.37	6.43	2.27
10	50.27	31.42	18.31	1.16	5.45	2.50
15	39.88	39.92	20.20	0.92	4.32	2.63
20	34.10	45.60	20.30	0.78	3.66	2.64
25	26.23	54.66	19.11	0.60	2.82	2.55

Table (4.10): Absorbance spectra, transmittance, reflectivity, absorption coefficient, extinction coefficient, and refractive index with the dye concentration change of $Ag/V_2O_5/ZnO$ NPs.

Concentration of dye (ppm)	P.D.E% absorbance	P.D.E% transmittance	P.D.E% reflectivity	Absorption coefficient (cm^{-1})	Extinction coefficient ($\times 10^{-6}$)	Refractive index
5	58.70	25.88	15.42	1.35	6.34	2.29
10	34.90	44.77	20.33	0.80	3.75	2.64
15	23.80	57.80	18.40	0.55	2.58	2.50
20	20.80	61.94	17.26	0.48	2.25	2.42
25	16.40	68.54	15.06	0.38	1.78	2.27

We can explain the effect of addition the dye to V_2O_5/ZnO and $Ag/V_2O_5/ZnO$ on all optical properties based on the Tables (4.9) and (4.10). Table (4.9) shows that the refractive index, absorption coefficient, reflectivity and absorbance all decrease except transmittance will be increases, as the concentration of dye increases.

This is because the dye molecules absorb light and then re-emit it in a different direction. This reduces the amount of light that is reflected back from the surface, and it also reduces the amount of light that is absorbed by the nanoparticle, therefore will be more transparence.

The specific effects of dye on the optical properties of V_2O_5/ZnO and $Ag/V_2O_5/ZnO$ nanoparticles depend on the type of dye, the concentration of the dye, and the deposition method.

However, in general, the addition of dye can be used to tune the optical properties of V_2O_5/ZnO and Ag/V_2O_5/ZnO nanoparticles, which can be useful for applications in optical devices.

The refractive index and reflectivity of the nanoparticle also show a non-monotonic behavior as the concentration of dye increases. The reflectivity and refractive index increases as the concentration of dye increases from 5 ppm to 10 ppm, and then decreases as the concentration of dye increases from 10 ppm to 25 ppm.

There are a few possible explanations for this behavior. One possibility is that the dye molecules are initially arranged in a way that enhances the scattering of light. As the concentration of dye increases, the dye molecules become more tightly packed, which reduces the scattering of light. This results in a decrease in the refractive index and reflectivity of the nanoparticle [143].

Another possibility is that the dye molecules are absorbing different wavelengths of light at different concentrations. At low concentrations, the dye molecules may be absorbing light that is not important for the refractive index or reflectivity of the nanoparticle.

As the concentration of dye increases, the dye molecules may start to absorb light that is important for the refractive index or reflectivity of the nanoparticle.

When the concentration of dye is low, the dye molecules are spaced far apart. This allows light to pass through the nanoparticle without being scattered much [144].

As the concentration of dye increases, the dye molecules become more tightly packed. This reduces the amount of space between the dye molecules, which increases the amount of scattering.

This results in a decrease in the refractive index and reflectivity of the nanoparticle. Overall, the refractive index and reflectivity data in the Table (4.9) is not as clear-cut as the other optical properties.

There are a few possible explanations for the behavior of the refractive index and reflectivity data, and more research is needed to understand the underlying mechanism.

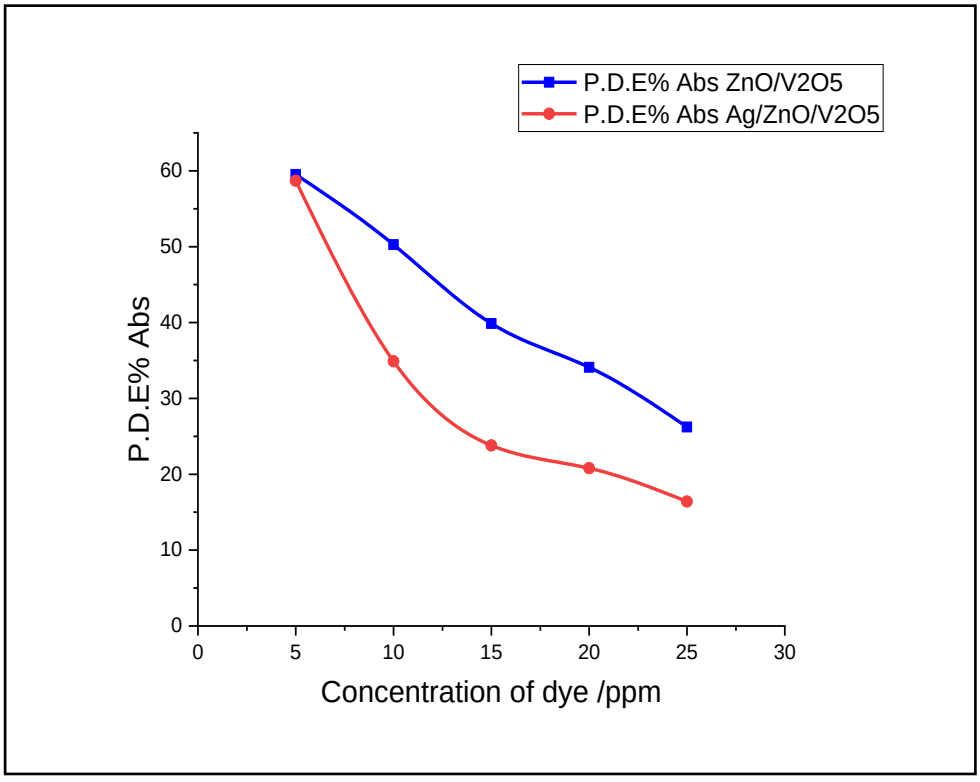

Fig. (4.19): Absorbance with the dye concentration change for V_2O_5/ZnO and Ag/V_2O_5/ZnO NPs.

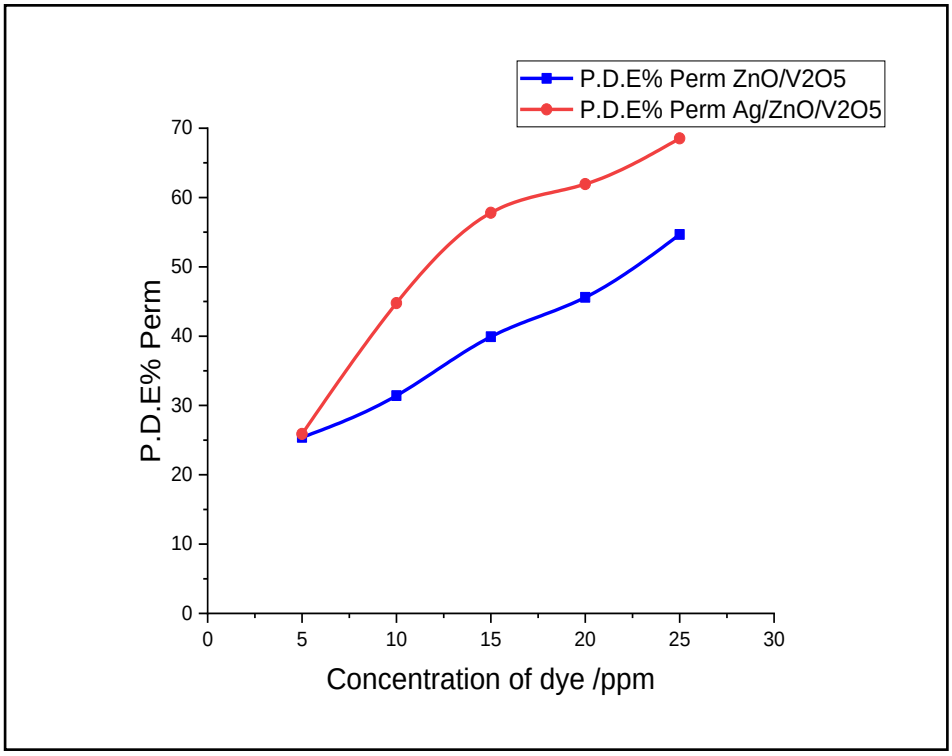

Fig. (4.20): Transmittance with the dye concentration change for V_2O_5/ZnO and Ag/V_2O_5/ZnO NPs.

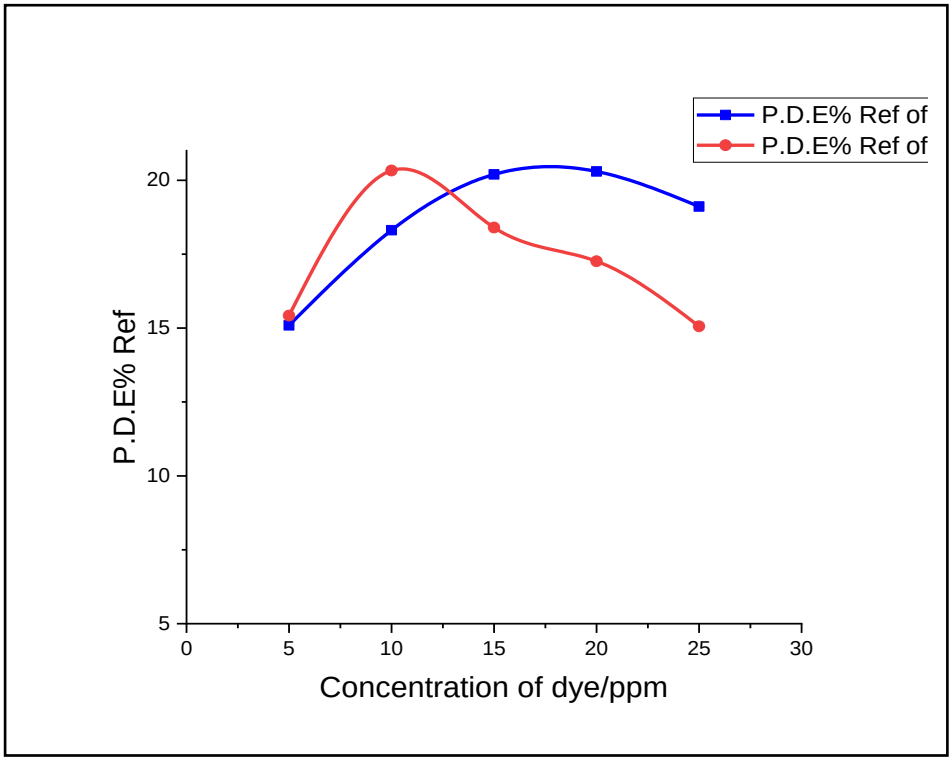

Fig. (4.21): Reflectivity with the dye concentration change for V_2O_5/ZnO and Ag/V_2O_5/ZnO NPs.

The results in Table (4.11) lead us to the conclusion that the absorbance efficiency somewhat increases randomly while transmittance and reflectivity both drop irregularly. Absorbance increasing when 0.2 g of nanomaterial is utilized.

The maximum absorbance was attained using 0.2 g of the V_2O_5/ZnO nanocomposite in comparison to other quantities.

This relates to the lowest recorded permeability for the same amount of 0.2 g, the highest transmittance when at 0.1 g, and the lowest recorded reflectivity for the same amount of 0.2 g, the highest reflectivity when at 0.1 g.

While the Table (4.12) shows the absorbance efficiency increases systematically when increasing the amount of nanocomposite, consistent decrease in both transmittance and reflectivity efficiency as the amount of nanocomposite increases, which corresponds to an ongoing improvement in the nanocomposite crystal structure and surface area following the photodeposition process.

The Fig. (4.22), (4.23) and (4.24) display the findings from the two Tables (4.11) and (4.12).

The greatest value of the extinction coefficient for V_2O_5/ZnO was 9.11×10^{-6} at the amount of 0.2 g, while the highest value of the absorption coefficient was 1.94 cm^{-1}. As the amount of Ag/V_2O_5/ZnO nanocomposite increases, the absorption coefficient and the extinction coefficient increases.

At amount of 0.6 g, the absorption coefficient reached its greatest value of 1.40 cm^{-1}, and the greatest value of the extinction coefficient was 6.57×10^{-6}.

Table (4.11): Absorbance spectra, transmittance, reflectivity, absorption coefficient, extinction coefficient, and refractive index with the mass change of V_2O_5/ZnO NPs.

Mass of nanoparticles(g)	**P.D.E% absorbance**	**P.D.E% transmittance**	**P.D.E% reflectivity**	**Absorption coefficient (cm^{-1})**	**Extinction coefficient ($\times 10^{-6}$)**	**Refractive index**
0.1	48.60	32.65	18.75	1.12	5.26	2.53
0.2	84.08	14.42	01.50	1.94	9.11	1.27
0.4	59.52	25.39	15.09	1.37	6.43	2.27
0.6	60.96	24.56	14.48	1.40	6.57	2.23

Table (4.12): Absorbance spectra, transmittance, reflectivity, absorption coefficient, extinction coefficient, and refractive index with the mass change of Ag/V_2O_5/ZnO NPs.

Mass of nanoparticles(g)	P.D.E% absorbance	P.D.E% transmittance	P.D.E% reflectivity	Absorption coefficient (cm^{-1})	Extinction coefficient ($\times 10^{-6}$)	Refractive index
0.1	54.17	28.72	17.11	1.25	5.87	2.41
0.2	56.42	27.27	16.31	1.30	6.10	2.35
0.4	58.70	25.88	15.42	1.35	6.34	2.29
0.6	66.32	21.71	11.97	1.53	7.18	2.06

In other words, we can say that there are two effects in this different behavior for each of the refractive index and reflectivity as follows:

1- Scattering: The refractive index of a material is a measure of how much light is bent when it passes through the material. The reflectivity of a material is a measure of how much light is reflected back from the surface of the material. Both the refractive index and reflectivity can be affected by scattering, which is the process of light being redirected by particles in a material. When the amount of nanoparticles is low, the dye molecules are spaced far apart. This allows light to pass through the nanoparticles without being scattered much.

As the amount of nanoparticles increases, the dye molecules become more tightly packed. This reduces the amount of space between the dye molecules, which increases the amount of scattering. This results in a decrease in the refractive index and reflectivity of the nanoparticles.

2- Absorbance: The refractive index and reflectivity of a material can also be affected by absorption, which is the process of light being absorbed by the material.

When the amount of nanoparticles is low, the dye molecules absorb a small amount of light. This does not have a significant impact on the refractive index or reflectivity of the nanoparticles. As the amount of nanoparticles increases, the dye molecules absorb more light.

This reduces the amount of light that is available to be reflected or refracted, which results in a decrease in the refractive index and reflectivity of the nanoparticles.

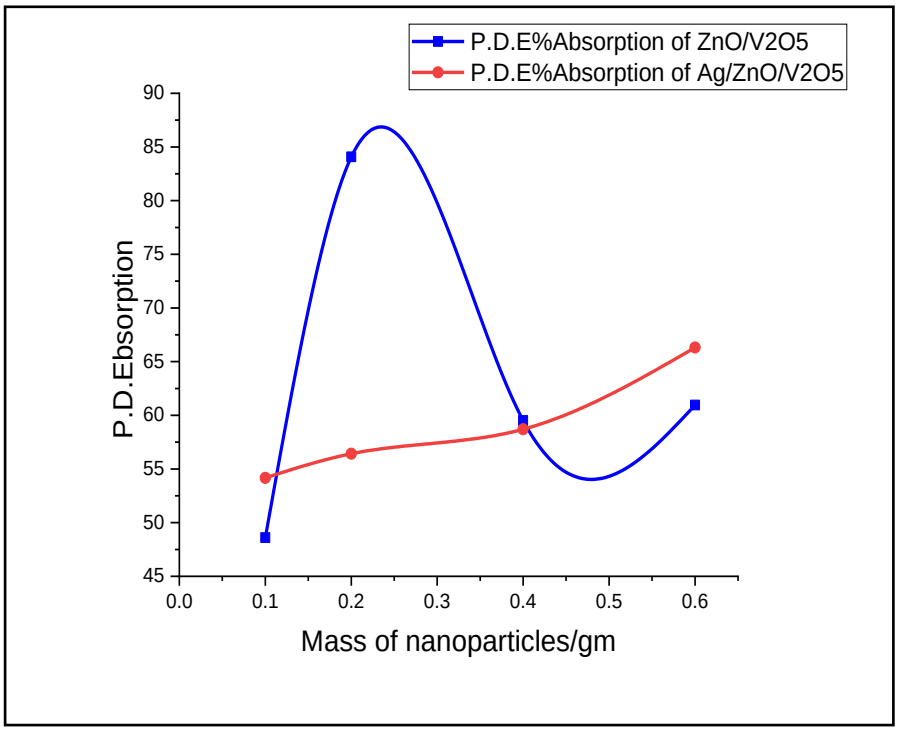

Fig. (4.22): Absorbance with the mass change for V_2O_5/ZnO and Ag/V_2O_5/ZnO NPs.

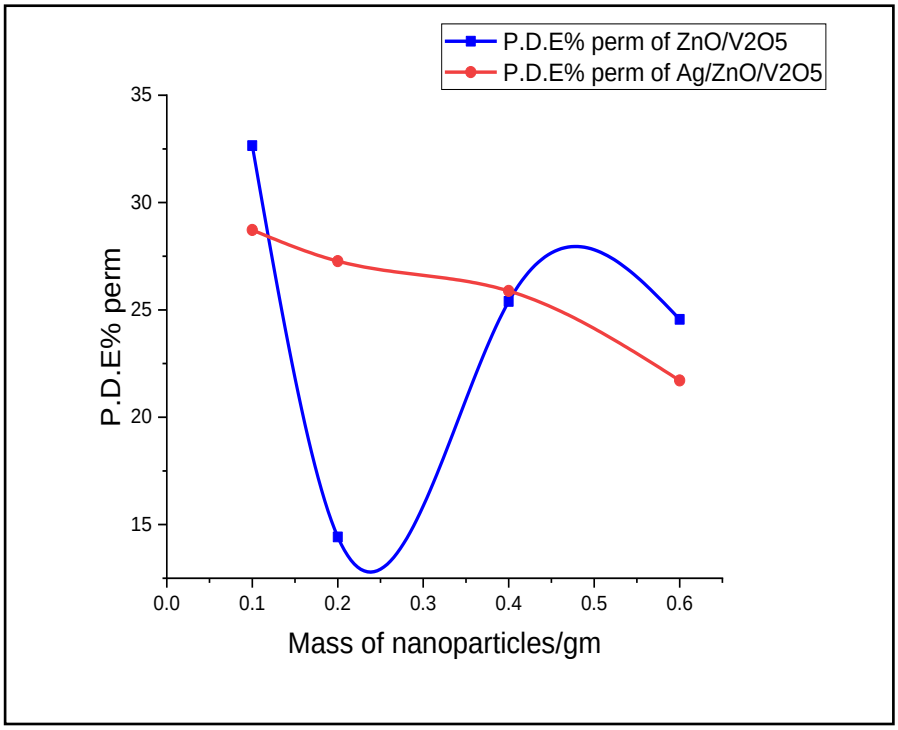

Fig. (4.23): Transmittance with the mass change for V_2O_5/ZnO and Ag/V_2O_5/ZnO NPs.

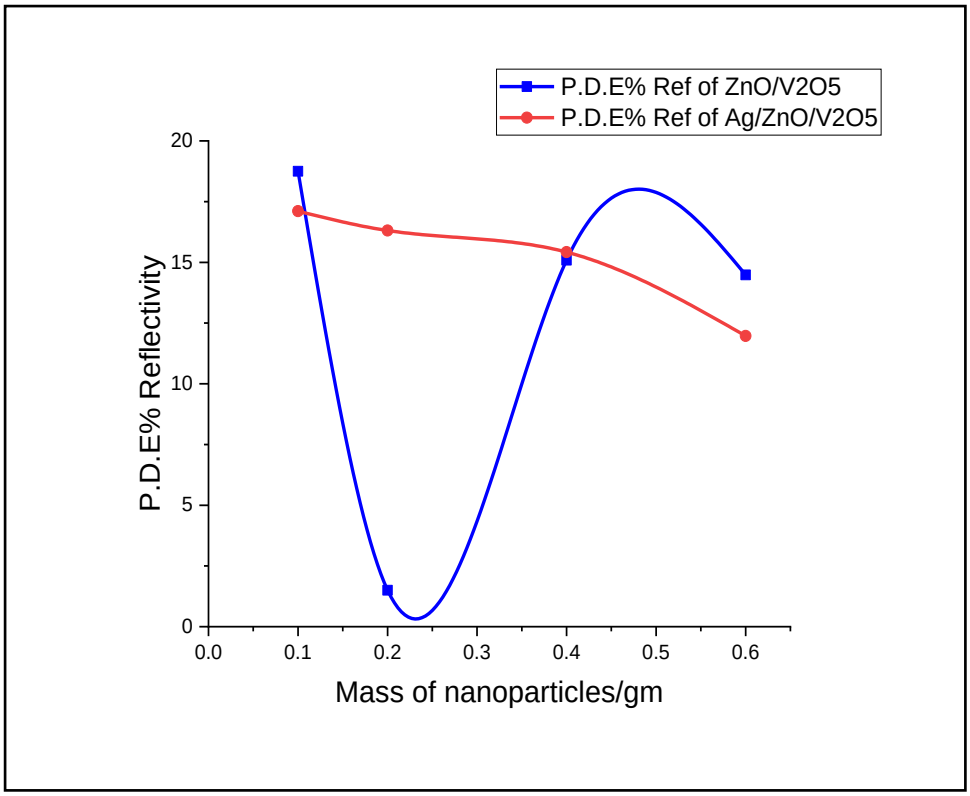

Fig. (4.24): Reflectivity with the mass change for V_2O_5/ZnO and Ag/V_2O_5/ZnO NPs.

The results in Tables (4.13) and (4.14) lead to the conclusion that the absorbance efficiency increases, while transmittance and reflectivity both decreasing regularly.

The maximum absorbance is attained using 2.6 mW/cm^2 of the V_2O_5/ZnO and Ag/V_2O_5/ZnO nanocomposite in comparison to other Light intensity. This is related to the lowest recorded transmittance for the same amount at same Light intensity.

The highest transmittance and highest reflectivity recorded at Light intensity is 0.8 mW/cm^2, while the lowest transmittance and reflectivity recorded at Light intensity is 2.6 mW/cm^2.

Table (4.13) shows the absorbance efficiency increases systematically when increasing the light intensity of nanocomposite, consistent decrease in both transmittance and reflectivity efficiency as the light intensity of nanocomposite increases, which corresponds to an ongoing improvement in the nanocomposites crystal structure and surface area following the photodeposition process.

In Fig. (4.25), (4.26) and (4.27), the greatest value of the extinction coefficient for ZnO/V_2O_5 is 10.1×10^{-6}at the light intensity for 2.0 mW/cm^2, while the highest value of the absorption coefficient is 2.15 cm^{-1} at the same light intensity.

As the light intensity of $Ag/V_2O_5/ZnO$ nanocomposite increases, both the absorption coefficient and the extinction coefficient increases. At 2.6 mW/cm^2, the absorption coefficient reached its greatest value of 1.56 cm^{-1} and the greatest value of the extinction coefficient is 7.32×10^{-6}.

Table (4.13): Absorbance spectra, transmittance, reflectivity, absorption coefficient, extinction coefficient, and refractive index with the light intensity change of V_2O_5/ZnO NPs.

Light intensity (mW/cm^2)	P.D.E% absorbance	P.D.E% transmittance	P.D.E% reflectivity	Absorption coefficient (cm^{-1})	Extinction coefficient ($\times 10^{-6}$)	Refractive index
0.8	49.19	32.21	18.60	1.13	5.30	1.91
2.0	59.52	25.39	15.09	1.37	6.43	2.27
2.6	93.35	11.65	05.00	2.15	10.1	1.33

Table (4.14): Absorbance spectra, transmittance, reflectivity, absorption coefficient, extinction coefficient, and refractive index with the light intensity change of $Ag/V_2O_5/ZnO$ NPs.

Light intensity (mW/cm^2)	P.D.E% absorbance	P.D.E% transmittance	P.D.E% reflectivity	Absorption coefficient (cm^{-1})	Extinction coefficient ($\times 10^{-6}$)	Refractive index
0.8	52.07	30.15	17.78	1.20	5.63	2.46
2.0	58.70	25.88	15.42	1.35	6.34	1.81
2.6	68.06	20.86	11.08	1.56	7.32	1.99

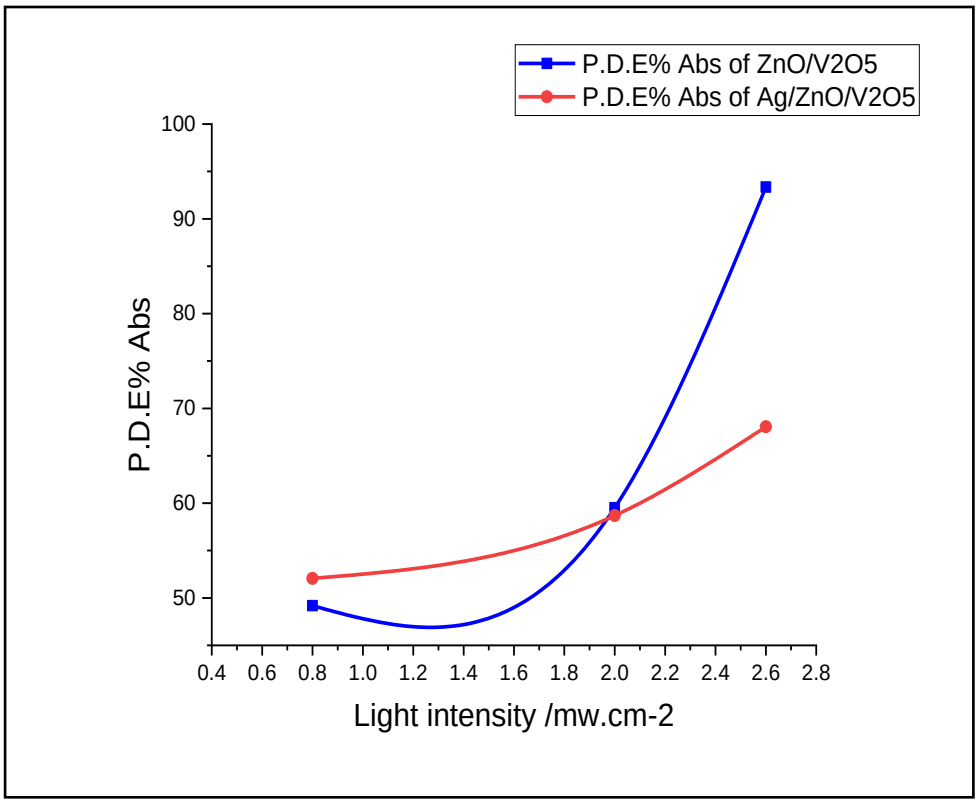

Fig. (4.25): Absorbance with the light intensity change for V_2O_5/ZnO and $Ag/V_2O_5/ZnO$ NPs.

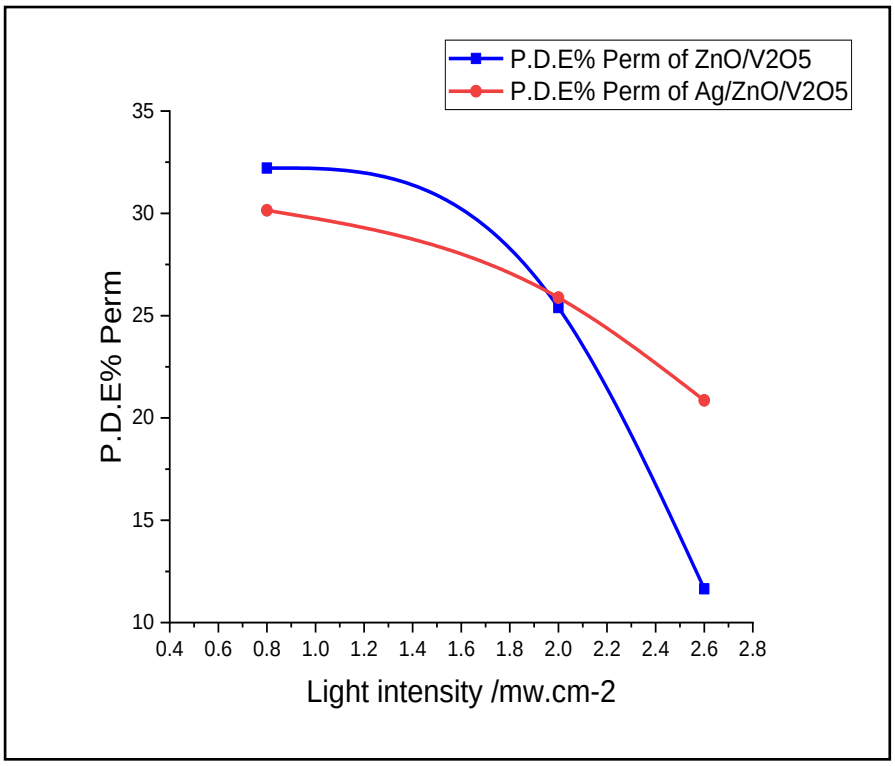

Fig. (4.26): Transmittance with the light intensity change for V_2O_5/ZnO and Ag/V_2O_5/ZnO NPs.

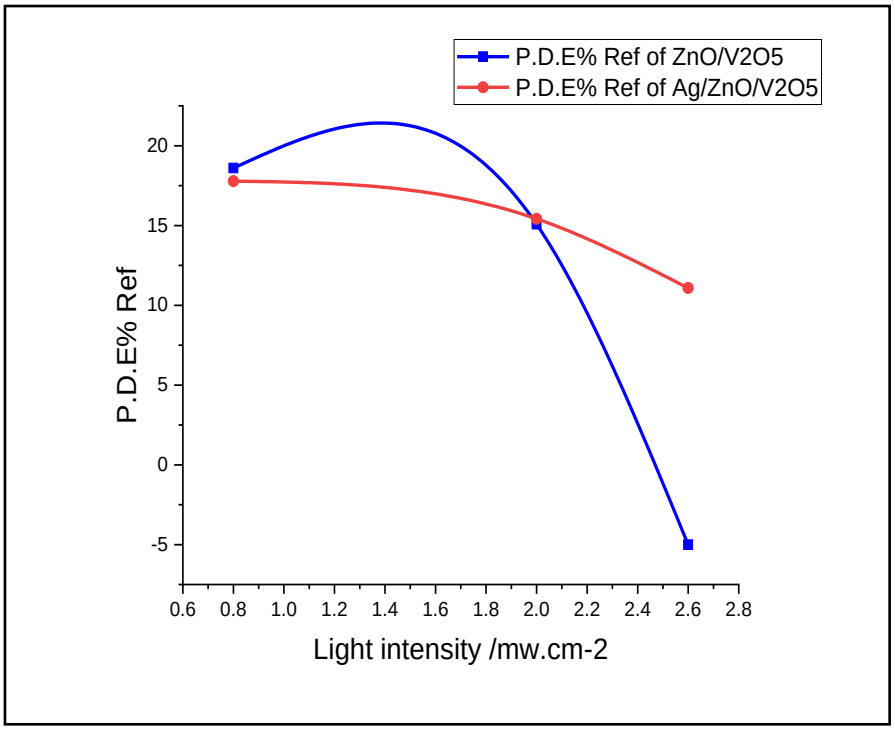

Fig. (4.27): Reflectivity with the light intensity change for V_2O_5/ZnO and Ag/V_2O_5/ZnO NPs.

4.14 Optical Energy Gap

Studies of the optical characteristics of these particles using UV-Vis Spectroscopy in the range of wavelengths (200-800) nm have determined the value of the energy band gap of created nanocomposites. Based on the sample's absorption spectrum, the band gap energy was determined using the formula below [145]:

$$E_g = 1240/\lambda_{max} \quad (4.1)$$

From Eq. (2.10) and plotting $(\alpha h\nu)^2$ versus the photon energy ($h\nu$) in Fig. (4.28), the value of energy gap (E_g) can be found by extrapolating the intercept of the curve to zero absorption in the photon energy axis.

The band gap energy of pure ZnO nanomaterial of 3.25 eV was less than that of bulk ZnO 3.37 eV. This reduction in the energy band gap agrees with those reported in the Reference [48].

The band gap energies of V_2O_5/ZnO and Ag/V_2O_5/ZnO nanomaterial were smaller than that of pure ZnO nanomaterial which may be due to the effect of vanadium and Ag concentrations. The band gap energies of V_2O_5/ZnO nanomaterial was 3.15 eV and the band gap energies of Ag/V_2O_5/ZnO NPs was 3.04 eV as shown in Fig. (4.28).

Fig. (4.28) shows the decrease in energy gap of Ag/V_2O_5/ZnO nanomaterial compared with V_2O_5/ZnO and pure ZnO.

Due to the collective oscillation of the silver nanoparticles, free electrons with the light wave, these free electrons produce the surface absorption band.

Consequently, there is a net charge difference, which serves as a restoring force. As a result, all of the absorption edges exhibit a dipolar oscillation, and the band gap energy drops, showing that the silver has been doped with V_2O_5/ZnO nanoparticles [146, 147].

Low absorption in the visible range is present of Ag/V_2O_5/ZnO in Fig. (4.28). The increase in defect sites on the catalyst structure, which can prevent the recombination of charge carriers and boost the photocatalytic activity of V_2O_5/ZnO has led to an improvement in the optical absorption of V_2O_5/ZnO.

The results show that the band gap shrinks as a result of photodeposition [148, 149].

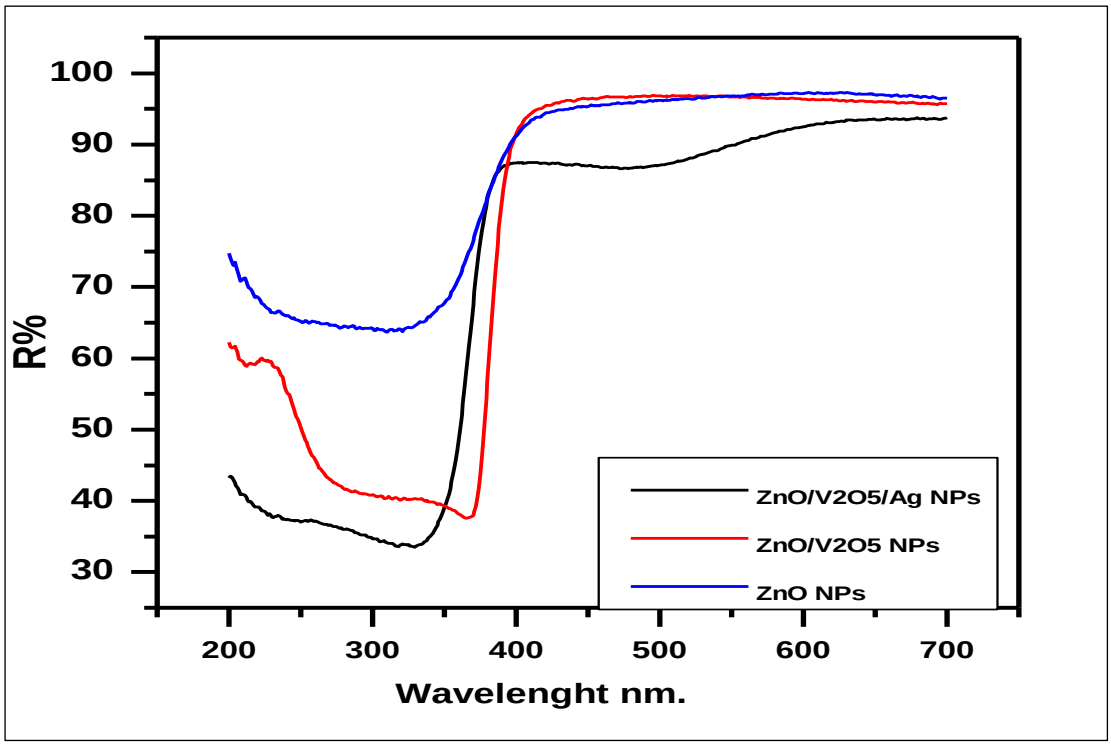

Fig. (4.28): Energy gab diagram for ZnO, V_2O_5/ZnO and Ag/V_2O_5/ZnO NPs.

The different energy gaps of the Ag/V_2O_5/ZnO NPs can be explained by a number of factors, including, (in general):

•The photodeposition method: The deposition method can affect the structure and properties of the nanoparticle, which can affect the energy gap. For example, physical vapor deposition (PVD) is a low-energy process that typically produces films with a high energy gap. Chemical vapor deposition (CVD) is a higher-energy process that can produce films with a lower energy gap.

•The presence of Ag: The presence of Ag can also affect the energy gap of the nanoparticle. Ag is a metal with a relatively low energy gap, and it can interact with the ZnO and V_2O_5 layers to create defects that can reduce the energy gap.

The silver can donate electrons to the V_2O_5/ZnO NPs, which can lead to a decrease in the energy gap of the V_2O_5/ZnO NPs. The interaction between the Ag layer and the V_2O_5/ZnO NPs can also lead to the formation of a new energy level within the V_2O_5/ZnO NPs.

This new energy level can act as a trap for electrons, which can also lead to a decrease in the energy gap. The decrease in the band gaps of the samples is useful in optoelectronic devices [150].

There are several factors for the decrease in the optical energy band gap such as grain size, carrier concentration, structural parameters and lattice strain and existence of defects or impurities [151,152].

4.15 Conclusions:

1. Hydrothermal synthesis done usefully for synthesis ZnO, V_2O_5/ZnO nanoparticles.

2. Doping Ag on the surface of V_2O_5/ZnO play important role of reduced the recombination process.

3. Highest Photocatalytic removal have been got in the presence of

Ag/V_2O_5/ZnO.

4. V_2O_5/ZnO shows good Photocatalytic activity.

5.The best conditions for Photocatalytic degradation of dyes was light

intensity 2.6 mW/cm^2 mass of catalyst 0.4 g concentration with

Ag/V_2O_5/ZnO.

6. The average crystallite size of the V_2O_5/ZnO NPs decreased when they were doped with silver nitrate during the photodeposition process and the energy gap decreased, the smallest particle size was 12.71 nm, and the smallest value of the energy gap was 3.04 eV.

7. The absorbance efficiency increases systematically when increasing the amount of Ag/V_2O_5/ZnO NPs, consistent decrease in both transmittance and reflectivity efficiency as the amount of nanocomposite increases, both the absorption coefficient and the extinction coefficient increases.

8. The absorbance efficiency increases systematically when increasing the Light intensity of Ag/V_2O_5/ZnO NPs, consistent decrease in both transmittance and reflectivity efficiency.

9. The refractive index and reflectivity of the nanoparticle also show a non-monotonic behavior as the concentration of dye increases.

10. The catalytic efficiency of ZnO was rather low, but V_2O_5/ZnO shows better efficiency, Ag/V_2O_5/ZnO NPs shows maximum absorbance efficiency.

4.16 Recommendations and Suggestions

1- Preparation of nanoparticles by solvothermal method and comparison of results prepared by hydrothermal method.

2- Using different activators on the surfaces of nanocomposites and studying their effect instead of silver.

3- Adding a tungsten trioxide compound to the nanocomposite and studying the structural and optical properties of the new composite.

4- Studying recycling for prepared nanocomposites to further confirm the photocatalytic efficiency, and the find of the subsequent characterization revealed.

5- Studying the importance of photocatalysis in the medical aspect by conducting the process of photolysis of some medical drugs, such as Emoxylin, using prepared catalyst nanomaterials.

References

References

1. Tian, J., Zhao, Z., Kumar, A., Boughton, R. I., & Liu, H. (2014). Recent progress in design, synthesis, and applications of one-dimensional TiO_2 nanostructured surface heterostructures. *Chemical Society Reviews, 43*(20), 6920-6937.
2. Basahel, S. N., Ali, T. T., Mokhtar, M., & Narasimharao, K. (2015). Influence of crystal structure of nanosized ZrO_2 on photocatalytic degradation of methyl orange. *Nanoscale research letters, 10*, 1-13.
3. Zhang, L., Sun, L., Liu, S., Huang, Y., Xu, K., & Ma, F. (2016). Effective charge separation and enhanced photocatalytic activity by the heterointerface in MoS_2/reduced graphene oxide composites. *Chemical Society Reviews, 6*(65), 60318-60326.
4. Robinson, T., McMullan, G., Marchant, R., & Nigam, P. (2001). Remediation of dyes in textile effluent: a critical review on current treatment technologies with a proposed alternative. *Bioresource technology, 77*(3), 247-255.
5. Hao, O. J., Kim, H., & Chiang, P.-C. (2000). Decolorization of wastewater. *Critical reviews in environmental science and technology, 30*(4), 449-505.
6. Li, B., & Cao, H. (2011). ZnO graphene composite with enhanced performance for the removal of dye from water. *Journal of Materials Chemistry, 21*(10), 3346-3349.
7. Wu, Q., Zhou, M., Gong, Y., Li, Q., Yang, M., Yang, Q., & Zhang, Z. (2018). Three-dimensional bandgap-tuned Ag_2S quantum dots/reduced graphene oxide composites with enhanced adsorption and photocatalysis under visible light. *Catalysis Science & Technology, 8*(20), 5225-5235.
8. Huang, J., Xu, X., Gu, C., Fu, G., Wang, W., & Liu, J. (2012). Flower-like and hollow sphere-like WO_3 porous nanostructures: Selective synthesis and their photocatalysis property. *Materials Research Bulletin, 47*(11), 3224-3232.
9. Lin, Z., Li, J., Zheng, Z., Yan, J., Liu, P., Wang, C., & Yang, G. (2015). Electronic reconstruction of α-Ag_2WO_4 nanorods for visible-light photocatalysis. *American Chemical Society nano, 9*(7), 7256-7265.
10. Mahanthappa, M., Kottam, N., & Yellappa, S. (2019). Enhanced photocatalytic degradation of methylene blue dye using CuSCdS nanocomposite under visible light irradiation. *Applied Surface Science, 475*, 828-838.

11. Sobhani-Nasab, A., Pourmasoud, S., Ahmadi, F., Wysokowski, M., Jesionowski, T., Ehrlich, H., & Rahimi-Nasrabadi, M. (2019). Synthesis and characterization of $MnWO_4$/$TmVO_4$ ternary nano-hybrids by an ultrasonic method for enhanced photocatalytic activity in the degradation of organic dyes. *Materials Letters, 238*, 159-162.
12. Lops, C., Ancona, A., Di Cesare, K., Dumontel, B., Garino, N., Canavese, G., & Cauda, V. (2019). Sonophotocatalytic degradation mechanisms of Rhodamine B dye via radicals generation by micro- and nano-particles of ZnO. *Applied Catalysis B: Environmental, 243*, 629-640.
13. Kiwaan, H., Atwee, T., Azab, E., & El-Bindary, A. (2020). Photocatalytic degradation of organic dyes in the presence of nanostructured titanium dioxide. *Journal of Molecular Structure, 1200*, 115-127.
14. Linsebigler, A. L., Lu, G., & Yates Jr, J. T. (1995). Photocatalysis on TiO_2 surfaces: principles, mechanisms, and selected results. *Chemical reviews, 95*(3), 735-758.
15. Guo, Q., Zhang, Q., Wang, H., & Zhao, Z. (2018). ZnO_2-promoted ZnO as an efficient photocatalyst for the photoreduction of carbon dioxide in the presence of water. *Catalysis Communications, 103*, 24-28.
16. Zhao, X., Li, M., & Lou, X. (2014). Sol–gel assisted hydrothermal synthesis of ZnO microstructures: morphology control and photocatalytic activity. *Advanced Powder Technology, 25*(1), 372-378.
17. Wang, J., Wang, Z., Huang, B., Ma, Y., Liu, Y., Qin, X., & Dai, Y. (2012). Oxygen vacancy induced band-gap narrowing and enhanced visible light photocatalytic activity of ZnO. *American Chemical Society applied materials & interfaces, 4*(8), 4024-4030.
18. Zheng, L., Zheng, Y., Chen, C., Zhan, Y., Lin, X., Zheng, Q., & Zhu, J. (2009). Network structured SnO_2/ZnO heterojunction nanocatalyst with high photocatalytic activity. *Inorganic Chemistry, 48*(5), 1819-1825.
19. Marschall, R. (2014). Semiconductor composites: strategies for enhancing charge carrier separation to improve photocatalytic activity. *Advanced Functional Materials, 24*(17), 24 .2440-21
20. Solarska, R., Santato, C., Jorand-Sartoretti, C., Ulmann, M., & Augustynski, J. (2005). Photoelectrolytic oxidation of organic species at mesoporous tungsten trioxide film electrodes under visible light illumination. *Journal of applied electrochemistry, 35*, 715-721.

21. Adhikari, S., Sarkar, D., & Madras, G. (2015). Highly efficient WO_3–ZnO mixed oxides for photocatalysis. *Chemical Society Reviews, 5*(16), 11895-11904.
22. Khan, A. U., Hussain, T., Abdullah, Khan, M. A., Almostafa, M. M., Younis, N. S., & Yahya, G. (2023). Antibacterial and Antibiofilm Activity of Ficus carica-Mediated Calcium Oxide (CaONPs) Phyto-Nanoparticles. *Molecules, 28*(14), 53-55.
23. Govan, J., & Gun'ko, Y. K. (2014). Recent advances in the application of magnetic nanoparticles as a support for homogeneous catalysts. *Nanomaterials, 4*(2), 222-241.
24. Sheldon, R., & Downing, R. (1999). Heterogeneous catalytic transformations for environmentally friendly production. *Applied Catalysis A: General, 189*(2), 163-183.
25. Cole-Hamilton, D. J. (2003). Homogeneous catalysis--new approaches to catalyst separation, recovery, and recycling. *Science, 299*(5613), 1702-1706.
26. Cornils, B., & Herrmann, W. A. (2003). Concepts in homogeneous catalysis: the industrial view. *Journal of Catalysis, 216*(1-2), 23-31.
27. Laurent, S., Forge, D., Port, M., Roch, A., Robic, C., Vander Elst, L., & Muller, R. N. (2008). Magnetic iron oxide nanoparticles: synthesis, stabilization, vectorization, physicochemical characterizations, and biological applications. *Chemical reviews, 108*(6), 2064-2110.
28. Tiwari, J. N., Tiwari, R. N., & Kim, K. S. (2012). Zero-dimensional, one-dimensional, two-dimensional and three-dimensional nanostructured materials for advanced electrochemical energy devices. *Progress in Materials Science, 57*(4), 724-803.
29. Mody, V. V., Siwale, R., Singh, A., & Mody, H. R. (2010). Introduction to metallic nanoparticles. *Journal of Pharmacy and bioallied sciences, 2*(4), 282.
30. Chng, L. L., Erathodiyil, N., & Ying, J. Y. (2013). Nanostructured catalysts for organic transformations. *Accounts of chemical research, 46*(8), 1825-1837.
31. Dey, S., Das, S., & Kar, A. K. (2021). Role of precursor dependent nanostructures of ZnO on its optical and photocatalytic activity and influence of FRET between ZnO and methylene blue dye on photocatalysis. *Materials Chemistry and Physics, 270*, 124872.

32. Ballesteros-Balbuena, M., Roa-Morales, G., Vilchis-Nestor, A., Castrejón-Sánchez, V., Vigueras-Santiago, E., Balderas-Hernández, P., & Camacho-López, M. (2020). Photocatalytic urchin-like and needle-like ZnO nanostructures synthetized by thermal oxidation. *Materials Chemistry and Physics*, *244*, 122-703.
33. Arca, E., Fleischer, K., & Shvets, I. (2009). Influence of the precursors and chemical composition of the solution on the properties of ZnO thin films grown by spray pyrolysis. *The Journal of Physical Chemistry C*, *113*(50), 21074-21081.
34. Romero, R., Leinen, D., Dalchiele, E., Ramos-Barrado, J., & Martín, F. (2006). The effects of zinc acetate and zinc chloride precursors on the preferred crystalline orientation of ZnO and Al-doped ZnO thin films obtained by spray pyrolysis. *Thin Solid Films*, *515*(4), 1942-1949.
35. Kwoka, M., Lyson-Sypien, B., Kulis, A., Maslyk, M., Borysiewicz, M. A., Kaminska, E., & Szuber, J. (2018). Surface properties of nanostructured, porous ZnO thin films prepared by direct current reactive magnetron sputtering. *Materials*, *11*(1), 131.
36. Zhang, Q., Dandeneau, C. S., Zhou, X., & Cao, G. (2009). ZnO nanostructures for dye-sensitized solar cells. *Advanced materials*, *21*(41), 4087-4108.
37. Kołodziejczak-Radzimska, A., & Jesionowski, T. (2014). Zinc oxide from synthesis to application: a review. *Materials*, *7*(4), 2833-2881.
38. Islam, F., Shohag, S., Uddin, M. J., Islam, M. R., Nafady, M. H., Akter, A., & Cavalu, S. (2022). Exploring the journey of zinc oxide nanoparticles (ZnO-NPs) toward biomedical applications. *Materials*, *15*(6), 2160.
39. Espitia, P. J. P., Soares, N. d. F. F., Coimbra, J. S. d. R., de Andrade, N. J., Cruz, R. S., & Medeiros, E. A. A. (2012). Zinc oxide nanoparticles: synthesis, antimicrobial activity and food packaging applications. *Food and bioprocess technology*, *5*, 1447-1464.
40. Nagaraju, P., Vijayakumar, Y., Reddy, M. R., & Deshpande, U. (2019). Effect of vanadium pentoxide concentration in ZnO/V_2O_5 nanostructured composite thin films for toluene detection. *Chemical Society Reviews advances*, *9*(29), 16515-16524.
41. Sharma, R. K., Kumar, P., & Reddy, G. (2015). Synthesis of vanadium pentoxide (V_2O_5) nanobelts with high coverage using plasma assisted PVD approach. *Journal of Alloys and Compounds*, *638*, 289-297.

42. Zou, C., Fan, L., Chen, R., Yan, X., Yan, W., Pan, G., & Gao, W. (2012). Thermally driven V_2O_5 nanocrystal formation and the temperature-dependent electronic structure study. *CrystEngComm*, *14*(2), 626-631.
43. Yao, J., Li, Y., Massé, R. C., Uchaker, E., & Cao, G. (2018). Revitalized interest in vanadium pentoxide as cathode material for lithium-ion batteries and beyond. *Energy Storage Materials, 11*, 205-259.
44. Chakrabarti, S., & Dutta, B. K. (2004). Photocatalytic degradation of model textile dyes in wastewater using ZnO as semiconductor catalyst. *Journal of hazardous materials, 112*(3), 269-278.
45. Akhtar, M. S., Khan, M. A., Jeon, M. S., & Yang, O.-B. (2008). Controlled synthesis of various ZnO nanostructured materials by capping agents-assisted hydrothermal method for dye-sensitized solar cells. *Electrochimica Acta, 53*(27), 7869-7874.
46. Hong, R., Li, J., Chen, L., Liu, D., Li, H. Z., Zheng, Y., & Ding, J. (2009). Synthesis, surface modification and photocatalytic property of ZnO nanoparticles. *Powder Technology, 189*(3), 426-432.
47. Shidpour, R., Simchi, A., Ghanbari, F., & Vossoughi, M. (2014). Photo-degradation of organic dye by zinc oxide nanosystems with special defect structure: Effect of the morphology and annealing temperature. *Applied Catalysis A: General, 472*, 198-204.
48. Moulahi, A., & Sediri, F. (2014). ZnO nanoswords and nanopills: Hydrothermal synthesis, characterization and optical properties. *Ceramics International, 40*(1), 943-950.
49. Yin, H., Yu, K., Song, C., Huang, R., & Zhu, Z. (2014). Synthesis of Au-decorated V_2O_5/ZnO heteronanostructures and enhanced plasmonic photocatalytic activity. *American Chemical Society applied materials & interfaces, 6*(17), 14851-14860.
50. Aslam, M., Ismail, I. M., Almeelbi, T., Salah, N., Chandrasekaran, S., & Hameed, A. (2014). Enhanced photocatalytic activity of V_2O_5/ZnO composites for the mineralization of nitrophenols. *Chemosphere, 117*, 115-123.
51. Bechambi, O., Chalbi, M., Najjar, W., & Sayadi, S. (2015). Photocatalytic activity of ZnO doped with Ag on the degradation of endocrine disrupting under UV irradiation and the investigation of its antibacterial activity. *Applied Surface Science, 347*, 414-420.
52. Saravanan, R., Khan, M. M., Gupta, V. K., Mosquera, E., Gracia, F., Narayanan, V., & Stephen, A. (2015). ZnO/Ag/CdO nanocomposite for visible light-induced photocatalytic degradation of industrial textile effluents. *Journal of colloid and interface science, 452*, 126-133.

53. Alshammari, A. S., Chi, L., Chen, X., Bagabas, A., Kramer, D., Alromaeh, A., & Jiang, Z. (2015). Visible-light photocatalysis on C-doped ZnO derived from polymer-assisted pyrolysis. *Chemical Society Reviews, 5*(35), 27690-27698.
54. Kong, X., Li, L., Guo, Z., Zeng, C., Huang, J., Li, C., & Li, J. (2016). Soft chemical in situ synthesis and photocatalytic performance of 1D $Ag/AgCl/V_2O_5$ hetero-nanostructures. *Materials Letters, 183*, 215-218.
55. Gad, E. S., Chaudhary, K., Ahmed, A. H., Rafiq, S., Yousif, A. M., & Suleman, M. (2023). Hydrothermal synthesis of bifunctional Ag/MnO_2 nanowires decorated with V_2O_5 nanorice: Photocatalytic and electrochemical impedance study for treatment of impurities present in waste water. *Optical Materials, 135*, 113-274.
56. Zhu, X.-D., Zheng, Y.-L., Feng, Y.-J., & Sun, K.-N. (2018). Delicate $Ag/V_2O_5/TiO_2$ ternary nanostructures as a high-performance photocatalyst. *Journal of solid state chemistry, 258*, 691-694.
57. Sawant, S. Y., Kim, J. Y., Han, T. H., Ansari, S. A., & Cho, M. H. (2018). Electrochemically active biofilm-assisted biogenic synthesis of an Ag-decorated ZnO/C core–shell ternary plasmonic photocatalyst with enhanced visible-photocatalytic activity. *New Journal of Chemistry, 42*(3), 1995-2005.
58. Aliaga, J., Cifuentes, N., González, G., Sotomayor-Torres, C., & Benavente, E. (2018). Enhancement photocatalytic activity of the heterojunction of two-dimensional hybrid semiconductors ZnO/V_2O_5. *Catalysts, 8*(9), 374.
59. El-Sheshtawy, H. S., El-Hosainy, H. M., Shoueir, K. R., El-Mehasseb, I. M., & El-Kemary, M. (2019). Facile immobilization of Ag nanoparticles on $g\text{-}C_3N_4/V_2O_5$ surface for enhancement of post-illumination, catalytic, and photocatalytic activity removal of organic and inorganic pollutants. *Applied Surface Science, 467*, 268-276.
60. Le, T. K., Kang, M., & Kim, S. W. (2019). Relation of photoluminescence and sunlight photocatalytic activities of pure V_2O_5 nanohollows and V_2O_5/RGO nanocomposites. *Materials Science in Semiconductor Processing, 100*, 159-166.
61. Abed, A. S., Qasim, S. J., & Abbas, A. F. (2020). Structural and Optical Properties of ZnO Nanorods Thin Films Prepared Using Hydrothermal Technique and Effect of growth time. *Journal of Kufa-Physics, 12*(2).

62. Jawad, A. S., & Al-gubury, H. Y. (2021). Studying the Effect of Different Parameters on Photocatalytic Degradation of Commercial Safranin-T Dye by Using ZnO/V_2O_5 Nanocomposite. *NeuroQuantology, 19*(8), 59.
63. Mukhtar, F., Munawar, T., Nadeem, M. S., ur Rehman, M. N., Riaz, M., & Iqbal, F. (2021). Dual S-scheme heterojunction ZnO–V_2O_5–WO_3 nanocomposite with enhanced photocatalytic and antimicrobial activity. *Materials Chemistry and Physics, 263*, 124-372.
64. Dey, B., Narzary, R., Chouhan, L., Bhattacharjee, S., Parida, B., Mondal, A., & Srivastava, S. (2022). Crystal structure, optical and dielectric properties of Ag: ZnO composite-like compounds. *Journal of Materials Science: Materials in Electronics*, 1-14.
65. Yang, A., Luo, J., Xie, Z., & Chen, Q. (2022). Photocatalytic activity of V_2O_5/ZnV_2O_6 catalysts and its origin: Insights into enhanced photocatalytic mechanisms via DFT study. *Applied Surface Science, 599*, 153-894.
66. Srinivasan alias Arunsankar, N., Anbuchezhiyan, M., & Harish, S. (2022). Investigation of C–ZnO/V_2O_5 nanocomposite for organic compound decomposition under visible light. *Journal of Materials Science: Materials in Electronics, 33*(12), 9743-9754.
67. Shalaby, N. H., Al-Mhyawi, S. R., Ragab, A. H., Elmawgoud, H., Al-Swat, E. A., & Al-Thubaiti, N. M. (2023). Waste-Extracted Zn and Ag Co-Doped Spent Catalyst-Extracted V_2O_5 for Photocatalytic Degradation of Congo Red Dye: Effect of Metal-Nonmetal Co-Doping. *Catalysts, 13*(3), 584.
68. Liu, R., Fu, X., Guo, Y., Zhang, J., & Tian, W. (2023). A study on Ag or Ce doped and co-doped ZnO for the photocatalytic degradation of RhB dye. *Vacuum, 215*, 112-337.
69. Raza, W., Ahmad, K., Khan, R. A., & Kim, H. (2023). Ag decorated ZnO for enhanced photocatalytic H_2 generation and pollutant degradation. *International Journal of Hydrogen Energy, 48*(75), 29011-29424.
70. Alzahrani, E. A., Nabi, A., Kamli, M. R., Albukhari, S. M., Althabaiti, S. A., Al-Harbi, S. A., & Malik, M. A. (2023). Facile Green Synthesis of ZnO NPs and Plasmonic Ag-Supported ZnO Nanocomposite for Photocatalytic Degradation of Methylene Blue. *Water, 15*(3), 384.
71. Ganesan, S., Gurunathan, R., Pasupuleti, R. R., Dahms, H.-U., Arul Pragasan, L., SenthilKannan, K., & Ponnusamy, V. K. (2023). Green synthesis of V_2O_5/ZnO nanocomposite materials for efficient photocatalytic and anti-bacterial applications. *Applied Nanoscience, 13*(1), 859-869.

72. Byrappa, K., & Adschiri, T. (2007). Hydrothermal technology for nanotechnology. *Progress in crystal growth and characterization of materials, 53*(2), 117-166.
73. Yoshimura, M., & Byrappa, K. (2008). Hydrothermal processing of materials: past, present and future. *Journal of Materials Science, 43*, 2085-2103.
74. Liu, Y.-L., Yang, Y.-H., Yang, H.-F., Liu, Z.-M., Shen, G.-L., & Yu, R.-Q. (2005). Nanosized flower-like ZnO synthesized by a simple hydrothermal method and applied as matrix for horseradish peroxidase immobilization for electro-biosensing. *Journal of Inorganic Biochemistry, 99*(10), 2046-2053.
75. Khorshidi, B., Biswas, I., Ghosh, T., Thundat, T., & Sadrzadeh, M. (2018). Robust fabrication of thin film polyamide-TiO_2 nanocomposite membranes with enhanced thermal stability and anti-biofouling propensity. *Scientific Reports, 8*(1), 784.
76. Ndlwana, L., Raleie, N., Dimpe, K. M., Ogutu, H. F., Oseghe, E. O., Motsa, M. M., & Mamba, B. B. (2021). Sustainable hydrothermal and solvothermal synthesis of advanced carbon materials in multidimensional applications. *Materials, 14*(17), 50-94.
77. Khan, Y., Sadia, H., Ali Shah, S. Z., Khan, M. N., Shah, A. A., Ullah, N., . . . Khedher, N. B. (2022). Classification, synthetic, and characterization approaches to nanoparticles, and their applications in various fields of nanotechnology. *Catalysts, 12*(11), 13-86.
78. Byrappa, K., & Adschiri, T. (2007). Hydrothermal technology for nanotechnology. *Progress in crystal growth and characterization of materials, 53*(2), 117-166.
79. Yang, J., Mei, S., & Ferreira, J. (2001). Hydrothermal synthesis of TiO_2 nanopowders from tetraalkylammonium hydroxide peptized sols. *Materials Science and Engineering: C, 15*(1-2), 183-185.
80. SONG, X.-l., Peng, Q., YANG, H.-m., & QIU, G.-z. (2006). Synthesis of ZnO doped ceria nanoparticles via azeotropic distillation processing. *Transactions of Nonferrous Metals Society of China, 16*, 350-355.
81. Chen, X., & Mao, S. S. (2007). Titanium dioxide nanomaterials: synthesis, properties, modifications, and applications. *Chemical reviews, 107*(7), 2891-2959.
82. Benamraoui, F. (2018). *Elimination des colorants cationiques par des charbons actifs synthétisés à partir des résidus de l'agriculture.*

83. Yakar, A., Ünlü, A., Yeşilçayır, T., & Bıyık, İ. (2020). Kinetics and thermodynamics of textile dye removal by adsorption onto iron oxide nanoparticles. *Nanotechnology for Environmental Engineering, 5*, 1-12.
84. Hunger, K. (2007). *Industrial dyes: chemistry, properties, applications*: John Wiley & Sons.
85. Sabry, F. (2022). *Multi Function Structure: Future Air Force systems will become integrated into multi-function material airframes with embedded sensor, and network components* (Vol. 17): One Billion Knowledgeable.
86. Pawlowski, L. (2008). *The science and engineering of thermal spray coatings*: John Wiley & Sons.
87. Subash, A. A., Chandramouli, K. V., Ramachandran, T., Rajendran, R., & Muthusamy, M. (2012). Preparation, characterization, and functional analysis of zinc oxide nanoparticle-coated cotton fabric for antibacterial efficacy. *Journal of the Textile Institute, 103*(3), 298-303.
88. Khudair, G. H., & Mohmood, K. H. (2021). Study of the effect of annealing during and after deposition on (crystal growth and some physical properties) of zinc sulfide (ZnS) nanoparticles prepared by vacuum thermal evaporation method (PVD). *Turkish Journal of Computer and Mathematics Education (turcomat), 12*(14), 2013-2029.
89. Salih, M. A.-A., Shinen, M. H., & Kareem, Q. (2021). Study of the effect of annealing temperature on the response of nano-films of ZnO to ammonia gas sensor. *In Journal of Physics Conference Series*, *1854*(1), 008-012.
90. Havrdova, M., Polakova, K., Skopalik, J., Vujtek, M., Mokdad, A., Homolkova, M., & Zboril, R. (2014). Field emission scanning electron microscopy (FE-SEM) as an approach for nanoparticle detection inside cells. *Micron, 67*, 149-154.
91. Inkson, B. J. (2016). Scanning electron microscopy (SEM) and transmission electron microscopy (TEM) for materials characterization. *In Materials characterization using nondestructive evaluation (NDE) methods*, 17-43.
92. Takahashi, C., Shirai, T., & Fuji, M. (2012). Observation of interactions between hydrophilic ionic liquid and water on wet agar gels by FE-SEM and its mechanism. *Materials Chemistry and Physics, 133*(1), 565-572.
93. Mishra, R. K., Zachariah, A. K., & Thomas, S. (2017). Energy-dispersive X-ray spectroscopy techniques for nanomaterial. In *Microscopy methods in nanomaterials characterization* (pp. 383-405): Elsevier.

94. Zheng, H., Meng, Y. S., & Zhu, Y. (2015). Frontiers of in situ electron microscopy. *Mrs Bulletin, 40*(1), 12-18.
95. Yu, L., Li, M., Wen, J., Amine, K., & Lu, J. (2021). (S) TEM-EELS as an advanced characterization technique for lithium-ion batteries. *Materials Chemistry Frontiers, 5*(14), 5186-5193.
96. Stadtländer, C. (2007). Scanning electron microscopy and transmission electron microscopy of mollicutes: challenges and opportunities. *Modern research and educational topics in microscopy, 1*, 122-131.
97. Petrosino, P., Pirrie, D., Santoro, L., & de Gennaro, R. (2022). Scanning Electron Microscopy (SEM) in Forensic Geoscience. *In Mineralogical Analysis Applied to Forensics: A Guidance on Mineralogical Techniques and Their Application to the Forensic Field, 316*, 61-91.
98. Torres, F. G., Troncoso, O. P., Lopez, D., Grande, C., & Gomez, C. M. (2009). Reversible stress softening and stress recovery of cellulose networks. *Soft Matter, 5*(21), 4185-4190.
99. Brunauer, S., Emmett, P. H., & Teller, E. (1938). Adsorption of gases in multimolecular layers. *American chemical society, 60*(2), 309-319.
100. Hanaor, D. A., Ghadiri, M., Chrzanowski, W., & Gan, Y. (2014). Scalable surface area characterization by electrokinetic analysis of complex anion adsorption. *Langmuir, 30*(50), 15143-15152.
101. Yusuf, M. O. (2023). Bond Characterization in Cementitious Material Binders Using Fourier-Transform Infrared Spectroscopy. *Applied Sciences, 13*(5), 3353.
102. McDonald, K. J., & Choi, K.-S. (2011). Synthesis and photoelectrochemical properties of $Fe_2O_3/ZnFe_2O_4$ composite photoanodes for use in solar water oxidation. *Chemistry of Materials, 23*(21), 4863-4869.
103. Pathakoti, K., Huang, M.-J., Watts, J. D., He, X., & Hwang, H.-M. (2014). Using experimental data of Escherichia coli to develop a QSAR model for predicting the photo-induced cytotoxicity of metal oxide nanoparticles. *Journal of Photochemistry and Photobiology B: Biology, 130*, 234-240.
104. Dean, K. (1984). Waves and fields in optoelectronics: Prentice-Hall series in solid state physical electronics. *Physics Bulletin*, *35*(8), 0031-9112.
105. Ünlü, H. (1992). A thermodynamic model for determining pressure and temperature effects on the bandgap energies and other properties of some semiconductors. *Solid-state electronics, 35*(9), 1343-1352.

106. Wang, Y.-Y., Jin, Q., Zhuang, K., Choi, J. K., & Nxumalo, J. (2021). Band gap measurement by nano-beam STEM with small off-axis angle transmission electron energy loss spectroscopy (TEELS). *Ultramicroscopy, 220*, 113164.
107. Flory, F., Escoubas, L., & Berginc, G. (2011). Optical properties of nanostructured materials: a review. *Journal of Nanophotonics, 5*(1), 052-502.
108. Pattar, J., Sawant, S. N., Nagaraja, M., Shashank, N., Balakrishna, K., Sanjeev, G., & Mahesh, H. (2009). Structural optical and electrical properties of vacuum evaporated indium doped zinc telluride thin films. *International Journal of Electrochemical Science, 4*(3), 369-376.
109. Hadi, R., & Salih, A. (2017). A Studing Of the Optical Properties Of ZnO thin film doped (ZnO) 1-x (SeO_2) x By (Sol-Gel spin coating). *Kirkuk Journal of Science, 12*(1), 69-80.
110. Panta, G., & Subedi, D. (2012). Electrical characterization of aluminum (Al) thin films measured by using four-point probe method. *Kathmandu University journal of science, Engineering and technology, 8*(2), 31-36.
111. Kruschwitz, J. D. T., & Pawlewicz, W. T. (1997). Optical and durability properties of infrared transmitting thin films. *Applied optics, 36*(10), 2157-2159.
112. Rajkumar, R., & Kumar, P. P. (2018). Optical, mechanical, dielectric and thermal properties of piperazinium benzoate single crystal for nonlinear optical applications. *Journal of Optics, 47*, 75-82.
113. Kose, S., Atay, F., Bilgin, V., & Akyuz, I. (2008). Some physical properties of copper oxide films: The effect of substrate temperature. *Materials Chemistry and Physics, 111*(2-3), 351-358.
114. Khudayer, I. H., Hussein, B. H., & Hamid, M. (2018). Depending the Structure and Optical Properties of Cadmi-um Telluride Films on the Doping Process. *Al-Mustansiriyah Journal of Science, 29(1)*, 2521-3520.
115. Zubko, P., Catalan, G., & Tagantsev, A. K. (2013). Flexoelectric effect in solids. *Annual Review of Materials Research, 43*, 387-421.
116. Chand, P., Gaur, A., Kumar, A., & Gaur, U. K. (2015). Effect of NaOH molar concentration on morphology, optical and ferroelectric properties of hydrothermally grown CuO nanoplates. *Materials Science in Semiconductor Processing, 38*, 72-80.

117. Benhebal, H., Chaib, M., Salmon, T., Geens, J., Leonard, A., Lambert, S. D., & Heinrichs, B. (2013). Photocatalytic degradation of phenol and benzoic acid using zinc oxide powders prepared by the sol–gel process. *Alexandria Engineering Journal, 52*(3), 517-523.
118. Akbar, I., Yuwono, A. H., Sofyan, N., Ramahdita, G., & Sholehah, A. (2015). Effect of citric acid addition upon the precipitation process on the nanostructural characteristics of ZnO nanoparticles. *Int. J. Technol, 6*, 1205.
119. Dimitriev, Y., Ivanova, Y., Staneva, A., Alexandrov, L., Mancheva, M., Yordanova, R., & Iliev, C. (2009). synthesis of submicron powders. *Journal of the University of Chemical Technology and Metallurgy*, *44*(3), 235-242.
120. Muñoz-Fernandez, L., Gómez-Villalba, L. S., Milošević, O., & Rabanal, M. E. (2022). Influence of nanoscale defects on the improvement of photocatalytic activity of Ag/ZnO. *Materials Characterization, 185*, 111-718.
121. Koyuncu, M. (2009). Adsorption of maxilon blue GRL from an aqueous solution: equilibrium and kinetic studies. *Asian Journal of Chemistry*, *21*(1), 121-127.
122. Alrobayi, E. M., Algubili, A. M., Aljeboree, A. M., Alkaim, A. F., & Hussein, F. H. (2017). Investigation of photocatalytic removal and photonic efficiency of maxilon blue dye GRL in the presence of TiO_2 nanoparticles. *Particulate Science and Technology, 35*(1), 14-20.
123. Alshamsi, H. A., Al Bedairy, M. A., & Alwan, S. H. (2021). Visible light assisted photocatalytic degradation of Rhodamine B dye on CdSe-ZnO nanocomposite: Characterization and kinetic studies. *Paper presented at the IOP conference series: earth and environmental science*, *722*, 005-012.
124. Reza, K. M., Kurny, A., & Gulshan, F. (2017). Parameters affecting the photocatalytic degradation of dyes using TiO_2. *Applied Water Science, 7*, 1569-1578.
125. Wang, F., Jiang, M., Qian, C., Yang, S., Li, C., Zhang, H., & Tang, X. (2017). Residual attention network for image classification. *Paper presented at the Proceedings of the IEEE conference on computer vision and pattern recognition*, 3156-3164.
126. Inkson, B. J. (2016). Scanning electron microscopy (SEM) and transmission electron microscopy (TEM) for materials characterization. In Materials characterization using nondestructive evaluation (NDE) methods. *Woodhead publishing*, 17-43.

127. Galarneau, A., Mehlhorn, D., Guenneau, F., Coasne, B., Villemot, F., Minoux, D., & Dath, J.-P. (2018). Specific surface area determination for microporous/mesoporous materials: The case of mesoporous FAU-Y zeolites. *Langmuir, 34*(47), 14134-14142.
128. Shannon, R. D. (1976). Revised effective ionic radii and systematic studies of interatomic distances in halides and chalcogenides. *Acta crystallographica section A: crystal physics, diffraction, theoretical and general crystallography, 32*(5), 751-767.
129. Achehboune, M., Khenfouch, M., Boukhoubza, I., Mothudi, B., Zorkani, I., & Jorio, A. (2019). Study on the effect of Er dopant on the structural properties of ZnO nanorods synthesized via hydrothermal method. *Paper presented at the Journal of Physics: Conference Series*, *1292*, 012-020.
130. Radičić, R., Maletić, D., Blažeka, D., Car, J., & Krstulović, N. (2022). Synthesis of silver, gold, and platinum doped zinc oxide nanoparticles by pulsed laser ablation in water. *Nanomaterials, 12*(19), 34-84.
131. Li, Q., Yuan, H., Zhang, M., Yan, W., Liao, B., Zhang, X., & Ying, M. (2022). Enhancement of magnetic moment of Er-implanted ZnO films by post-annealing in Ar and vacuum. *Materials Letters, 306*, 130-901.
132. Ismail, M., Taha, K., Modwi, A., & Khezami, L. (2018). ZnO nanoparticles: Surface and X-ray profile analysis. *J. Ovonic Res, 14*(5), 381-393.
133. Zhu, X.-D., Zheng, Y.-L., Feng, Y.-J., & Sun, K.-N. (2018). Delicate $Ag/V_2O_5/TiO_2$ ternary nanostructures as a high-performance photocatalyst. *Journal of solid state chemistry, 258*, 691-694.
134. Ntobeng, M. K., Imoisili, P. E., & Jen, T.-C. (2020). Synthesis and photocatalytic performance of Ag-TiVOX nanocomposite. *Journal of King Saud University-Science, 32*(7), 3103-3110.
135. Bau, S., Rastoix, O., Dazon, C., & Bardin-Monnier, N. (2023). Accounting for constituent particle polydispersion in the determination of the volume specific surface area equivalent diameter. *Paper presented at the matec web of Conferences*, *379*, 790-1008.
136. Khurshid, F., Jeyavelan, M., Hudson, M. S. L., & Nagarajan, S. (2019). Ag-doped ZnO nanorods embedded reduced graphene oxide nanocomposite for photo-electrochemical applications. *Royal Society open science, 6*(2), 181764.

137. Brayner, R., Dahoumane, S. A., Yéprémian, C., Djediat, C., Meyer, M., Couté, A., & Fiévet, F. (2010). ZnO nanoparticles: synthesis, characterization, and ecotoxicological studies. *Langmuir, 26*(9), 6522-6528.
138. Bau, S., Witschger, O., Gensdarmes, F., Rastoix, O., & Thomas, D. (2010). A TEM-based method as an alternative to the BET method for measuring off-line the specific surface area of nanoaerosols. *Powder Technology, 200*(3), 190-201.
139. Kaye, B. H. (2008). *Characterization of powders and aerosols*: John Wiley & Sons.
140. Bourrous, S., Ribeyre, Q., Lintis, L., Yon, J., Bau, S., Thomas, D., & Ouf, F.-X. (2018). A semi-automatic analysis tool for the determination of primary particle size, overlap coefficient and specific surface area of nanoparticles aggregates. *Journal of Aerosol Science, 126*, 122-132.
141. Albo Hay Allah, M. A., & Alshamsi, H. A. (2023). Facile green synthesis of ZnO/AC nanocomposites using Pontederia crassipes leaf extract and their photocatalytic properties based on visible light activation. *Journal of Materials Science: Materials in Electronics, 34*(16), 1263.
142. Mourdikoudis, S., Pallares, R. M., & Thanh, N. T. (2018). Characterization techniques for nanoparticles: comparison and complementarity upon studying nanoparticle properties. *Nanoscale, 10*(27), 12871-12934.
143. Zhang, Q., Dandeneau, C. S., Park, K., Liu, D., Zhou, X., Jeong, Y.-H., & Cao, G. (2010). Light scattering with oxide nanocrystallite aggregates for dye-sensitized solar cell application. *Journal of Nanophotonics, 4*(1), 041-540.
144. Vasileva, E., Chen, H., Li, Y., Sychugov, I., Yan, M., Berglund, L., & Popov, S. (2018). Light scattering by structurally anisotropic media: a benchmark with transparent wood. *Advanced Optical Materials, 6*(23), 999-1800.
145. Nallendran, R., Selvan, G., & Balu, A. (2019). CdO-Fe_3O_4 nanocomposite with enhanced magnetic and photocatalytic properties. *Materials Science-Poland, 37*(1), 100-107.
146. Ibănescu, M., Muşat, V., Textor, T., Badilita, V., & Mahltig, B. (2014). Photocatalytic and antimicrobial Ag/ZnO nanocomposites for functionalization of textile fabrics. *Journal of Alloys and Compounds, 610*, 244-249.
147. Choi, Y. I., Jung, H. J., Shin, W. G., & Sohn, Y. (2015). Band gap-engineered ZnO and Ag/ZnO by ball-milling method and their photocatalytic and Fenton-like photocatalytic activities. *Applied Surface Science, 356*, 615-625.

148. Muñoz-Fernandez, L., Sierra-Fernández, A., Milošević, O., & Rabanal, M. E. (2016). Solvothermal synthesis of Ag/ZnO and Pt/ZnO nanocomposites and comparison of their photocatalytic behaviors on dyes degradation. *Advanced Powder Technology, 27*(3), 983-993.
149. Abbas, A. M., Abid, M., Abbas, K. N., Aziz, W. J., & Salim, A. (2021). Photocatalytic activity of Ag-ZnO nanocomposites integrated essential ginger oil fabricated by green synthesis method. *Paper presented at the Journal of Physics: Conference Series*, *1892(1)*, 005-012.
150. Gupta, M. K., Sinha, N., & Kumar, B. (2011). p-type K-doped ZnO nanorods for optoelectronic applications. *Journal of Applied Physics, 109*(8), 32-35.
151. Majeed Khan, M., Wasi Khan, M., Alhoshan, M., AlSalhi, M., & Aldwayyan, A. (2010). Influences of Co doping on the structural and optical properties of ZnO nanostructured. *Applied Physics A, 100*, 45-51.
152. Ren, T., Baker, H. R., & Poduska, K. M. (2007). Optical absorption edge shifts in electrodeposited ZnO thin films. *Thin Solid Films, 515*(20-21), 7976-7983.

خلاصة

تم تحضير مركب أوكسيد الزنك النانوي (ZnO) ، ومتراكب أوكسيد الزنك/خامس أوكسيد الفناديوم النانوي (V_2O_5/ZnO) بواسطة عملية التخليق الحراري المائي، وتم تحضير متراكب أوكسيد الزنك/خامس أوكسيد الفناديوم النانوي المشوب بالفضة (Ag/V_2O_5/ZnO) عن طريق عملية الترسيب الضوئي كمحفزات نانوية.

باستخدام تقنيات XRD ، FE-SEM، EDX، FTIR، TEM و BET تم فحص التركيب البلوري والتركيب السطحي والخصائص البصرية للمحفزات وتميز المتراكب النانوي المشوب بالفضة بأعلى قمة مقارنة بالمتراكبات النانوية المحضرة الأخرى. تم حساب الحجم البلوري للمتراكبات النانوية المحضرة وتميز المتراكب النانوي المشوب بالفضة بأقل حجم بلوري مما يؤكد تأثير الفضة في عملية الترسيب الضوئي ونجاح تحضير المتراكب النانوي.

ازدادت مساحة سطح Ag/V_2O_5/ZnO مقارنةً بمركب ZnO و V_2O_5/ZnO ، تمت دراسة عملية التحفيز الضوئي لصبغة Maxilon Blue (GRL) باستخدام المتراكب النانوي المحضر V_2O_5/ZnO وكذلك المتراكب النانوي Ag/V_2O_5/ZnO

تم إجراء تحلل الصبغة بواسطة محاليل مائية مشعة تحتوي على تركيزات مختلفة من الصبغة وكميات مختلفة من المتراكبات النانوية المحضرة باستخدام مصباح الأشعة فوق البنفسجية المرئية عند شدات مخلفة من الضوء.

تم اختبار تأثير العوامل المختلفة على عملية التحلل الضوئي لصبغة GRL للوصول إلى الحالة المثلى، حيث تتضمن تأثير كتلة المتراكب النانوي وتأثير تركيز صبغة GRL وتأثير شدة الضوء المستخدم .

تم إجراء دراسة مقارنة للتحفيز الضوئي للمتراكبات النانوية المحضرة، حيث تغيرت كفاءة إزالة الصبغة بشكل كبير مع مرور الوقت حتى 60 دقيقة. تم حساب أطياف الامتصاصية والنفاذية والانعكاسية ومعامل الانكسار ومعامل الخمود ومعامل الامتصاص البصري للمواد المحفزة ضمن الطول الموجي 590 نانومتر، كما تم حساب فجوة الطاقة لكل من ZnO و V_2O_5/ZnO و Ag/V_2O_5/ZnO وقيمتها كانت (3.25، 3.15 و 3.04) الكترون فولت، على التوالي.

اظهرت النتائج ان للمتراكب النانوي الثلاثي $Ag/V_2O_5/ZnO$ نشاط تحفيز ضوئي افضل وقابلية لتحلل صبغة GRL افضل مقارنة بالمتراكب النانوي الثنائي V_2O_5/ZnO.

ان الحجم البلوري الصغير ومساحة السطح الواسعة في المتراكب النانوي $Ag/V_2O_5/ZnO$ له تأثير في نشاط التحفيز الضوئي الجيد، حيث كان لجسيمات الفضة النانوية تأثير كبير على فجوة النطاق ونشاط التحفيز الضوئي وعملية فصل الشحنات وبالتالي تحسين عملية التحفيز الضوئي.

جمهورية العراق

وزارة التعليم العالي والبحث العلمي

جامعة بابل

كلية العلوم- قسم الفيزياء

دراسة الفعالية الضوئية المحفزة لمتراكبات اوكسيد الخارصين النانوية المحدثة والمحضرة

اطروحة

مقدمة الى مجلس كلية العلوم- جامعة بابل

وهي جزء من متطلبات نيل درجة الدكتوراه فلسفة في العلوم/ الفيزياء

من قبل

احمد مسحور علي رفاس

بكالوريوس علوم جامعة المثنى / ٢٠٠٧

ماجستيرعلوم جامعة بابل / ٢٠١٦

بإشراف

أ.د. ايناس محمد الربيعي
كلية العلوم للبنات/جامعة بابل

أ.د. اياد فاضل القيم
كلية العلوم للبنات/جامعة بابل

١٤٤٥هـ

٢٠٢٣م